Spectral Analysis of the Helium Nova V445 Puppis

Sally Macfarlane

January 2012

A project submitted in partial fulfilment of the requirements for the degree M.Sc. in the Department of Astronomy, as part of the National Astrophysics and Space Science Programme
UNIVERSITY OF CAPE TOWN

Supervisor: A/Prof. P. A. Woudt

Abstract

Multifibre spectrographic observations of the bipolar helium nova V445 Puppis were made over five nights (two nights in January 2006 and three nights in January 2007) using the IMACS Integral Field Unit spectrograph on the Magellan I Telescope. Of these, spectra from the two best nights, 4 January 2006 and 8 January 2007, were reduced, extracted, calibrated and analysed in this thesis. The spectra extracted from seven target frames in 2006 and six target frames in 2007 were combined for 400 individual fibres. The two-dimensional spectra were then recombined into a data cube to create a three-dimensional picture of the emission from the nova. A combined spectrum, consisting of seven central fibres from the nova shell, features strong emission lines of [O III] λ5007, He I λ5876, He I λ7075 and the doublet [O II] λ7320/7330, with no evidence of hydrogen. I discuss two main results that arise from a spatial-intensity and spatial-velocity analysis of the spectra. Firstly, there are excess regions of [O III] λ5007 and [O II] λ7320/7330 emission at the extremes of the bipolar lobes that move outwards by $\sim 0\farcs2$ from 2006 to 2007. They can therefore be associated with the fast moving knots in the nova shell. Secondly, the deprojected radial velocities of these excess regions exceed $+$ 14000 km s^{-1} if the inclination of the polar axis with respect to the plane of the sky is $3.9 \pm 0.4^{\circ}$ and the emission is along the polar axis. These extremely high velocities suggest the excess regions could be due to either an ionisation front or to a bow-shock from a highly collimated outflow.

Acknowledgements

Thank you to the National Astrophysics and Space Science Program (NASSP) and the Astronomy Department at the University of Cape Town for their financial support. Opinions expressed and conclusions arrived at, are those of the author and are not necessarily to be attributed to the NRF.

Over the past three years, NASSP has given me the amazing opportunity to follow my dream career for which I will always be extremely grateful.

Thank you to Danny Steeghs for the interesting observations that are central to this thesis and for all the assistance with the reductions and analysis. To both Danny and my supervisor, Patrick Woudt, I greatly appreciate the amazing work visit to the University of Warwick.

I am very grateful to the many people who have assisted me with different aspects of this thesis. This includes Bianca Keene who installed IRAF on my computer, Valério Ribeiro who provided me with interesting and critical papers and books to read, Wendy Williams and Kosma van Maltitz who gave me the Latex thesis template and Moses Mogotsi for the help with uncertainty calculations.

My friends, especially Deanne de Bude, Kosma van Maltitz and Moses Mogotsi, have inspired and encouraged me throughout my thesis and have provided me with wonderful memories of office antics and ice-cream breaks. It goes without saying, that my main pillar of support is from my family and I am eternally grateful for all the love and silliness that I share with them every moment of the day.

Finally, a big thank you to my supervisor Patrick Woudt for all the invaluable assistance and the incredible opportunities that have helped to craft my love for astrophysics.

Plagiarism Declaration

I, Sally Macfarlane, know the meaning of plagiarism and declare that all of the work in the document, save for that which is properly acknowledged, is my own.

Contents

Chapter 1

Introduction

V445 Puppis (Nova Puppis 2000) is the first observed helium nova and, as such, provides an important empirical benchmark against which to test current theories of helium novae. Perhaps some of its most remarkable spectral features are the total lack of hydrogen emission, and the early abundance of carbon and helium after its outburst. This unique nova exhibits an expanding bipolar shell with a central dust disc that is still obscuring the nova remnant in 2011. Currently, the best model for this helium nova is a very massive white dwarf accreting mass from a helium star. It is possible the white dwarf will gradually gain mass through repeated outbursts and eventually, as it reaches a critical mass limit, explode as a supernova type Ia (Iben & Tutukov 1994, Wang et al. 2009) or a sub-luminous supernova .Ia (Bildsten et al. 2007). V445 Puppis is, therefore, a very intriguing object and an ideal candidate for multi-wavelength spectroscopic and photometric studies.

1.1 Novae

Helium novae, such as V445 Puppis (V445 Pup), are a sub-class of Cataclysmic Variable (CV) stars; see also Warner (1995) and Hellier (2001) for a detailed overview of Cataclysmic Variable stars. A CV is a semi-detached mass-transferring binary consisting of a cool donor star (the secondary star) and a degenerate white dwarf accretor (the primary star). The secondary star can be either a main sequence star, a red giant, a helium star or a white dwarf. The components of a non-magnetic CV are illustrated in Figure 1.1. In this figure, material that overfills the donor star's Roche Lobe is pulled through the inner Lagrangian point (denoted by L_1 in Figure 1.1) by the deep potential well of the more massive white dwarf (WD, the primary).

Due to the tidally-locked rotation in a non-magnetic CV, material moving through L_1 will have angular momentum. Therefore, instead of directly accreting onto the WD, the infalling material spirals around the WD, eventually settling into a circular orbit. As more

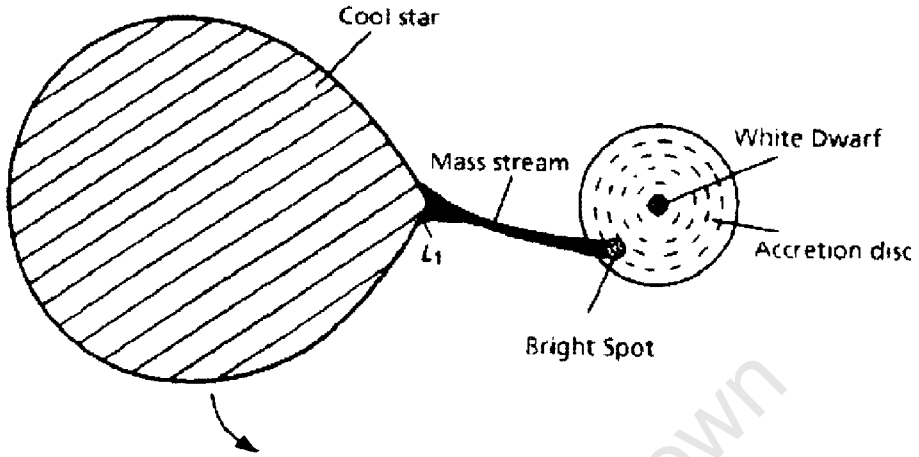

Figure 1.1: The components of a non-magnetic Cataclysmic Variable. Material overfills the Roche Lobe of the cool secondary star and accretes through the inner Lagrangian point, L_1, onto the white dwarf via an accretion disc. A very luminous spot is formed where the material stream initially interacts with the accretion disc. The entire tidally-locked system rotates as indicated (Warner 1995).

material is transferred, its potential energy is converted to heat as adjacent layers shear, causing the material to move into smaller radii. In order to conserve angular momentum, material also moves outwards and an accretion disc is formed around the WD.

In Dwarf Novae, a sub-class of CVs, instabilities in the mass transfer rate of the accretion disc occur when the mass transfer rate of the secondary star is greater than the accreting mass transfer rate causing a build up of material on the accretion disc (Osaki 1974). Once the disc reaches a critical density, the material is both expelled and deposited onto the surface of the WD. The dramatic release of potential energy in these dwarf novae outbursts cause the system to increase in brightness by around two to five magnitudes and can remain in this state for between two and twenty days (Warner 1995). These outbursts repeat on time scales of weeks to years (Warner 1995) and subsequent outbursts could lead to a greater build up of material on the WD.

More explosive outbursts (novae) occur when enough material accumulates on the surface of the white dwarf to ignite a thermonuclear runaway causing an abrupt increase in the system brightness of several magnitudes. In Classical Novae, the outburst is only known to have occurred once in recorded history, but if there is more than one recorded outburst for a specific system, they are then classified as Recurrent Novae.

1.1.1 Classical Novae

Classical Novae (CN) are a class of cataclysmic variable star systems, that each undergo an explosive outburst due to a thermonuclear runaway (see Bode & Evans (2008) for a comprehensive overview of novae). In these novae, enough mass is accreted from a donor star onto the partially degenerate surface layer of a massive white dwarf to cause the temperatures and densities of the accreted layers to rise. Nuclear burning starts which eventually causes a thermonuclear runaway explosion to take place. Although it can take anywhere from 10 to 10^6 years between successive nova outbursts to reach the required fusion temperatures, the runaway takes a matter of several seconds and ceases when the Fermi temperature is reached (Starrfield et al. 1974). This causes the expelled matter envelope to expand greatly and the system to reach a peak luminosity that can increase the system's brightness by around 11 magnitudes (Bode & Evans 2008). Afterwards, optically thick winds will occur, the envelope will reach a steady state and the novae will gradually decrease in brightness over a time that could stretch from days to months. The continuous low velocity wind in the nova after maximum outburst originates in the extended photosphere or common envelope of the nova (Williams 1992). The idealised light curve of the novae can be seen in Figure 1.2.

The spectrum of a nova will evolve through various stages during the outburst: The pre-maximum brightness spectrum is rarely observed but when it is (usually during the pre-maximum halt and rise shown in Figure 1.2), it features broad blue-shifted absorption lines over the spectrum of an optically thick, expanding and cooling shell. The spectrum may also feature P Cygni profiles. The spectrum then evolves to the 'principal phase' during maximum brightness. Here, the absorption lines become stronger and more blue-shifted and P Cygni lines form at the H I, Ca II, Na I and Fe II lines. For around 1 to 20 days after maximum brightness (depending on speed class), the spectrum moves into a 'diffuse enhanced phase' where the lines broaden and, along with a few P Cygni profiles, are further blue-shifted. Once the nova has decreased in brightness from maximum by about 1 to 2 magnitudes, the spectrum will move into a 'Orion spectrum phase' where emission lines, such as He I, C II, [N II], [O II], [N III], [N V] and occasionally H I, are formed and some line strengths dramatically change. Finally, the spectrum moves into the 'nebular phase' where emission lines of [O I], [N II], [O III] and [Ne III] form alongside intense Balmer emission lines, and the spectrum evolves to resemble a planetary nebula spectrum. The early emission spectrum of a CN is created by the evolution of the photosphere, the wind, and any surface nuclear reactions and, over time, these emission lines will evolve to become narrower due to non-uniformity in the gas expansion (Williams 1992).

Although no two novae are alike, most can be loosely classified according to certain similarities in their composition type and brightness evolution, post-outburst. For example, the light curves of novae can be grouped according to the rate at which their magnitude decreases from maximum brightness. This classification system, shown in Table 1.1, was introduced by Payne-Gaposchkin in 1957 (Gaposchkin 1964) and has not changed greatly

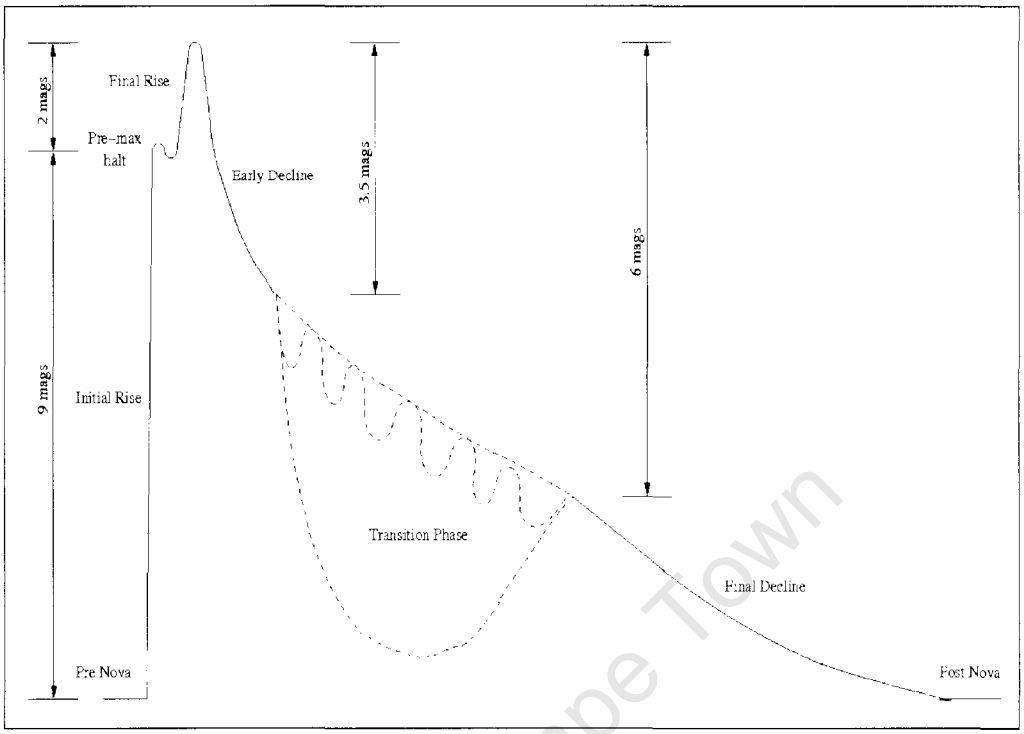

Figure 1.2: Idealised light curve of a classical nova (McLaughlin 1939,1960)

Table 1.1: Classification of nova light curves with t_2 the number of days taken to fall two magnitudes from peak brightness, and $\dot{m}_V$ the implied rate of decline (Bode & Evans 2008).

Speed Class	t_2 (days)	$\dot{m}_V$ (mag d^{-1})
Very fast	$<$ 10	$>$ 0.20
Fast	11 - 25	0.18 - 0.08
Moderately fast	26 -80	0.07 - 0.024
Slow	81 - 150	0.024 - 0.013
Very Slow	151 - 250	0.013 - 0.008

in the last 50 years (Bode & Evans 2008). There exists a direct relationship between the amplitude of eruption and the time taken to decrease by two magnitudes from peak (t_2), such that the faster the decay in the light curve, the greater the range of eruption (Warner 1995).

A more modern classification takes into account the spectroscopic features of novae. Immediately following outburst, Balmer lines are usually the most intense emission features. Therefore, Williams (1992) classified the CN according to the next most abundant lines in the 3500 Å to 7500 Å region of the spectrum; namely either the permitted transition Fe II lines or the He and N lines. Williams (1992) theorised that the spectrum originated from a two component gas; the discrete shell ejected at maximum light causing the broader He/N

emission lines, or from a continuous wind causing the narrower Fe emission lines. The profiles of the emission lines from the wind are generally P Cygni-like if they are optically thick but if the lines are optically thin, they are more likely to have broader and rounder peaked profiles. On the other hand, the emission lines that originate in the shell (which is uniformly expanding at a constant velocity) will have rectangular profiles.

In Fe II Novae, which account for $\sim 60\%$ of all novae, the spectrum takes longer to develop (on the order of weeks) and are therefore classified as slow novae with shell expansion velocities between $1000 < v_{exp}\ (\mathrm{km\,s^{-1}}) < 3500$ (Bode & Evans 2008). Compared to He/N Novae, they have a lower ionisation level with pronounced P Cygni absorption components in the Fe II and Balmer lines. In these novae, most will evolve to either a 'standard' nova or a neon nova, developing forbidden lines which are initially auroral transitions or low ionisation lines such as [N II] λ5755, the doublet [O II] λ7320/7330, [O III] λ4363 or [O I] λ6300 (Williams 1992). These forbidden lines are expected to occur in the expanding gases of the nova shell as the density decreases.

On the other hand, novae can be classified as He/N Novae. The spectrum of these fast novae develop within days and consist of flat-topped broader line profiles with little absorption. These novae have larger shell expansion velocities ($v_{exp} > 2500\ \mathrm{km\,s^{-1}}$ (Bode & Evans 2008)) and higher ionisation levels than the Fe II Novae. Unlike the Fe II novae, which radiate relatively strong auroral transitions of N and O in the initial forbidden line phase, He/N novae evolve to a nebular spectrum. They either do not produce forbidden lines at all, produce coronal forbidden lines, or result in a neon nova with lines of [Ne III] or [Ne V] (Williams 1992). These spectra exhibit strong lines of either He II λ4686, He I λ5876, N II λ5679/5001 or N III λ4640 which develop in the shell, as matter is ejected at high velocities from the WD surface at maximum outburst.

Due to the difficulties in modeling the hydrodynamics during the outburst, there is still much uncertainty in determining the amount of mass ejection in the thermonuclear reaction of a nova (Williams & Mason 2010). Williams et al. (2008) attempt to address this uncertainty by proposing to model the novae ejecta as colliding shells. In their studies of the high resolution spectrum of several nova, post outburst, they suggest the possibility of two distinct components of novae ejecta originating from different locations in the binary system. In the early spectrum of 15 novae, they found that 12 of the novae exhibited a spectrum consisting of multiple heavy element absorption lines having observable lifetimes of 2-8 weeks (Williams et al. 2008). The absorption lines in these systems, named transient heavy element absorption (THEA) systems, have different radial velocities. While the higher radial velocity lines are thought to originate from the innermost ejecta corresponding to the nuclear reactions from the WD surface, a circumbinary outer ejecta, existing prior to outburst, is the cause of the lower radial velocities. This large reservoir of slowly expanding gas is believed to be a common envelope formed from a spiral density wave which develops

when the accretion disc interacts with excess material moving through an outer Lagrangian point from the secondary star (Sytov et al. 2009). The collision of the faster moving WD ejecta with the outer gas ejecta converts the absorption spectrum to an emission spectrum and decelerates both ejecta components (Williams & Mason 2010). In this scenario, the WD ejecta gives rise to the observed 'diffuse enhanced' spectrum while the secondary ejecta is associated with the 'principal' spectrum (Williams et al. 2008). This model has implications for dust formation within the nova; since the dust is likely to be destroyed in the cloud collision, any dust model would have to consider the properties of both expanding shells.

Some novae have been observed to exhibit bipolar outflows, possibly due to jets in one theory described by Sokoloski et al. (2008). One such nova, RS Ophiuchi (RS Oph), is a recurrent nova containing a red giant secondary transferring mass to a massive white dwarf (Hachisu & Kato 2001). Although the origin of the bipolar outflow in RS Oph is uncertain, current theories suggest that jets shaping the outflow could be the result of either asymmetric explosions within the shell, the ejecta moving into inhomogeneous surroundings, or highly collimated outflows (Sokoloski et al. 2008). Alternatively, the bipolar structure could result from interactions with a pre-existing red-giant wind (Bode et al. 2007, Ribeiro et al. 2009). From radio observations of RS Oph, Sokoloski et al. (2008) found that the mechanism of highly collimated outflows was the most likely explanation for the observed bipolar outflows. In RS Oph, material is expelled from the WD in a nova outburst approximately every 20 years (Bode 1987). Strong shocks that accelerate particles to relativistic speeds are created in the nova when the expelled matter interacts with a circumbinary gas that is formed due to winds from the red giant (Eyres et al. 2009). Although Sokoloski et al. (2008) suggests that the nova explosion could have provided enough energy for the highly collimated outflow, it is uncertain what fuels the outflow later. They theorise that if the accretion disk survived the nova outburst, it could possibly collimate the flow, or it could result from some nonstandard way. This model is useful in understanding the highly collimated outflows in other novae, such as the recurrent nova U Sco (Kato & Hachisu 2003a), the fast nova V1494 Aql (Iijima & Esenoglu 2003) and the target of interest in this thesis, the helium novae V445 Pup (Woudt et al. 2009).

1.1.2 Helium Novae

The helium nova was first theoretically predicted by Kato et al. (1989). In a helium nova, helium-dominant (and hydrogen-deficient) mass is accreted from a secondary donor star to the surface of a (0.6 – 0.8 $M_{\odot}$) carbon-oxygen (CO) white dwarf. Once the helium layer reaches a critical limit, weak unstable helium shell flashes occur on the surface of the white dwarf that cause the resultant outburst (Kato et al. 1989). As the system goes into outburst, the star maintains a constant brightness, lasting a length of time that is dependent on the ignition mass (the mass of the envelope) (Ashok & Banerjee 2003). After outburst, the V-magnitude decreases slowly at first and then very rapidly later.

The donor star in the binary system of a helium nova is believed to be either a non-degenerate helium star (Iben & Tutukov 1991, Yoon & Langer 2004) or a semi-/fully degenerate star. In the latter case, Bildsten et al. (2007) suggested that helium novae were the result of ultra-compact binary star systems called AM Canum Venaticorum (AM CVn) binaries where a CO WD accretes helium from a WD donor in a doubly-degenerate binary system. These progenitors have very short orbital periods and therefore weak helium flashes.

Currently, the only observed helium nova to date is V445 Pup (Woudt et al. 2009). Detailed analysis of this prototype will hopefully help distinguish between the various theoretical models of helium novae by highlighting essential differences. Depending on the stellar components of the binary system in V445 Pup, the overall brightness of the system will change and therefore affect the kind of model used. For example, V445 Pup could not be a symbiotic nova (containing a red giant donor) as the deduced pre-outburst colour ($(V\text{-}K)^0$ = 1.58 mag) is too blue (Woudt et al. 2009), high-excitation emission lines have not been observed in the early decline phase and the light curve has declined faster than the expected decline rate of a symbiotic nova (Ashok & Banerjee 2003). Also, the luminosities observed are better described by a binary system containing a luminous accretion flow, a bright donor and a massive white dwarf rather than a less luminous AM CVn system (Woudt et al. 2009).

1.2 The Outburst and Evolution of the Helium Nova V445 Puppis

A wide range of observations exist for V445 Pup (V445 Pup) from which system parameters have been derived. These range from pre-outburst archival photometry (which sets the luminosity of the progenitor), photometry and spectroscopy during outburst and decline (observed hydrogen deficiency, light curve modeling) and post-outburst multi-wavelength photometry, spectroscopy and high resolution imaging (for distance calculations). In this section, I give an overview of V445 Pup at the various stages of its outburst with some of the system's parameters deduced from previous observations.

1.2.1 Discovery and Pre-outburst

V445 Pup was discovered in outburst on 30 December 2000 by K. Kanatsu and was reported as a star with $V \approx 8.6$ mag (Kato et al. 2000). The exact date of outburst is uncertain but VSNET* reports can be used to constrain the time of outburst by identifying the progenitor and its brightness.

*http://www.kusastro.kyoto-u.ac.jp/vsnet

By using the US Naval CCD Astrograph catalog (UCAC1), Platais et al. (2001) determined that the progenitor was a 13.6 magnitude star. Using photographic plates (IAUC 7552), Ashok & Banerjee (2003) identified an object brighter than 14 magnitudes between March 1994 and December 1999 in the position of V445 Pup. They found in later VSNET photographic records that the object was fainter than 12 mag on 26 September 2000, and then brighter at 8.8 mag on 23 November 2000. Therefore, the outburst most likely fell between these dates.

In order to reach the expected pre-outburst colours of the likely donor stars, (Woudt et al. 2009) deduced a pre-outburst brightness of 10.1 mag $\leq V^o \leq$ 10.4 mag (V^o is the extinction-corrected pre-outburst brightness including Galactic and circumstellar reddening corrections). For a distance of 8.2 kpc, this corresponds to a pre-outburst luminosity of $\log(L/L\odot) = 4.34 \pm 0.36$ based on the expansion parallax of the nova shell and the amount of dust obscuration ($E(B\text{-}V) = 0.62$) (Woudt et al. 2009). This high luminosity likely reflects a combination of a luminous companion (helium star) and a high mass transfer rate onto a massive white dwarf.

1.2.2 Outburst

V445 Pup is considered to be a slow nova, decreasing by $\sim$ 1 magnitude in the first six months (Ashok & Banerjee 2003). In June 2001, there was a sudden drop in brightness due to the optically thick wind ceasing and the photosphere shrinking rapidly. The brightness then declined more rapidly and a thick dust shell, rich in carbon, formed (Kato & Hachisu 2003b). Figure 1.3 is an up-to-date optical and near-infrared light curve illustrating the brightness of the nova before, during and after outburst. The most recent data point corresponds to 11 October 2011.

No hydrogen lines were identified in early infrared and optical observations in January 2001 by Ashok & Banerjee (2003) and Wagner et al. (2001), respectively. Both observed many permitted Fe II, Ca I and Ca II, O I and Na I emission lines. Ashok & Banerjee (2003) also found the spectrum to be unusually full of C I lines. Later, in mid-January, Kato & Hachisu (2003b) observed unconfirmed high excitation lines of O IV and He II, implying that the shell was still dense and illuminated by a rich UV source.

In an in-depth study of the early post-outburst spectra, Iijima & Nakanishi (2008) identified P Cygni absorption components in emission lines of Fe II, Ti II, Cr II, Na II and Mg II. Considering a system velocity of $+224 \pm 8$ km s^{-1}, they deduced that the components were blue-shifted by $\sim$500 km s^{-1} which relates to the outflow velocity of the equatorial dust during outburst (Iijima & Nakanishi 2008).

Nova eruptions have bolometric luminosities that are at or slightly above the Eddington luminosity (Bode & Evans 2008). As the luminosity of the nova approaches or exceeds the

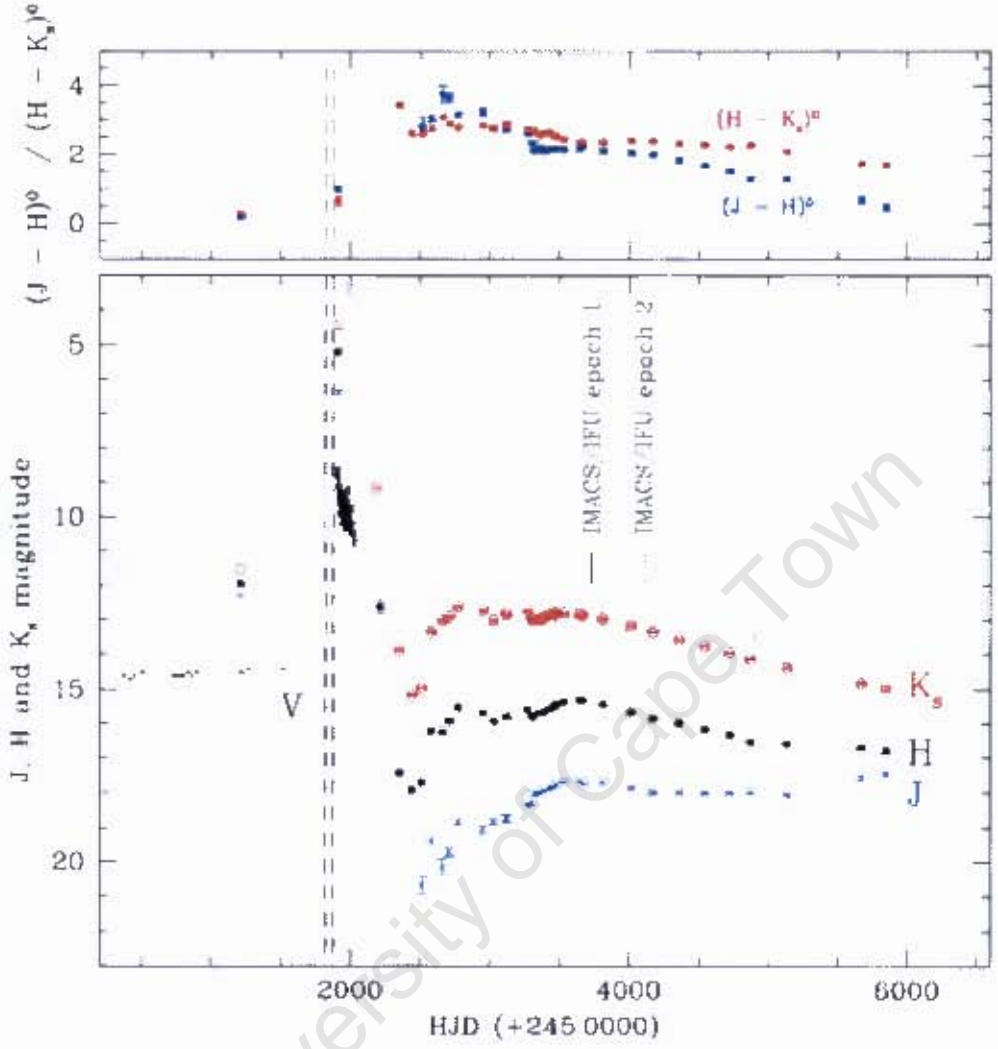

Figure 1.3: Lower panel: Near-infrared light curves of V445 Pup before, during and after outburst. Top Panel: Infrared colour evolution of V445 Pup (corrected for Galactic foreground extinction). The exact time of outburst is constrained to the region between the vertical dashed lines in both panels. Data from the two epochs indicated are analysed in this thesis (figure adapted from Woudt et al. 2009).

Eddington Limit, a high velocity expanding shell is ejected. The Eddington luminosity of a star with mass M can be expressed as:

$$\log(L_{edd}) - \frac{4\pi GMm_p c}{\sigma_T} \simeq 3.2 \times 10^4 (\frac{M}{\mathrm{M}_\odot})\mathrm{L}_\odot \tag{1.1}$$

where G is the gravitational constant, m_p is the mass of a proton, c is the speed of light, T is the temperature of the star, σ_T is the Thompson cross-section, $\mathrm{M}_\odot$ is the mass of the sun and $\mathrm{L}_\odot$ is the solar luminosity (Rybicki & Lightman 1979).

For a very massive white dwarf (WD mass $M_{wd} \simeq 1.33$ $M_{\odot}$), the Eddington luminosity is therefore $\log L_{edd}/L_{\odot} = 4.64$. Using the distance to V445 Pup of 8.2 kpc (Woudt et al. 2009), the peak luminosity of the nova during outburst is $\log L/L_{\odot} = 4.93$ (corrected for a Galactic reddening of $E(B\text{-}V) = 0.51$) which is therefore greater than the Eddington Luminosity. This is also seen in CN such as V1974 Cygni which often have peak luminosities that exceed the Eddington luminosity (Kato & Hachisu 2005).

1.2.3 Post-outburst Appearance and Evolution

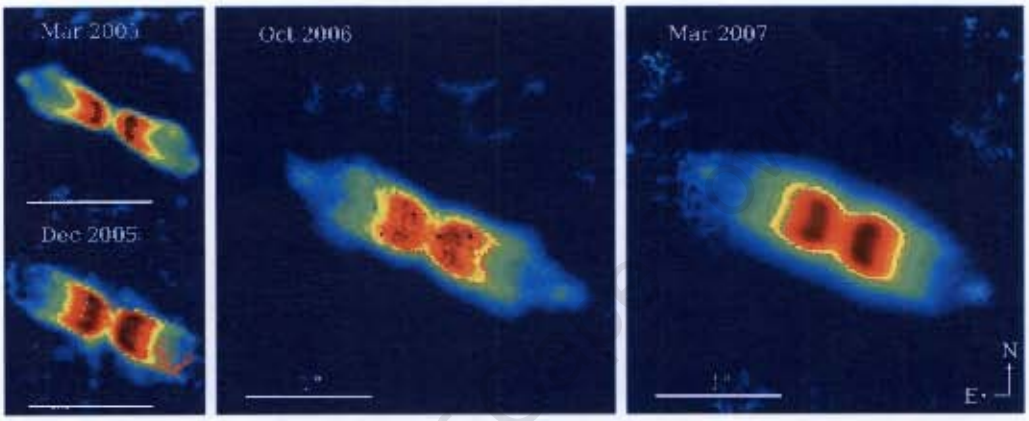

Figure 1.4: The evolving nova shell of V445 Pup obtained in the NIR K_s band. The data were obtained over two years using NAOS/CONICA on the VLT. All images are plotted on the same scale with a sampling of 27.15 mas pixel^{-1} (Woudt et al. 2009)

As shown in the detailed false colour near-infrared K_s images of V445 Pup in Figure 1.4 taken four to six years after outburst, the nova is expanding outwards in bipolar lobes; one orientated north-east (NE) and the other south-west (SW), with a inclination of $\sim$3.9° to the plane of the sky (Woudt et al. 2009). The nova system expands from one epoch to the next, which is clearly illustrated by the initially narrow waist of the nova widening over time. At all epochs, an equatorial dust disc shrouds the nova remnant and high speed knots are observed to move outwards at the extremes of the shell along the polar axis. The ejecta spans about 2″ - 3″ across the sky and the nova has a position angle of $\sim$ 66° (Woudt et al. 2009).

The expanding shell of V445 Pup is unlike any classical nova observed. Instead, it closely resembles the expanding shells seen in some planetary nebulae (PNe) and protoplanetary nebulae (pPNe). The major difference between V445 Pup and other PNe or pPNe is the large expansion velocity (polar shell expansion velocity $v_p = 6720 \quad 650$ km s^{-1}), that is more typical (although on the high end) of a nova outburst. From one-dimensional (1D) hydrodynamical models of PNe evolution (Schönberner et al. 2005, Raga et al. 2008), the observed edges of a PN shell are either due to an ionisation wave or to a shock front moving

at velocities that cannot be measured spectroscopically. Observations of the nova spectrum in 2006 and 2007 reveal a lack of [N II] λ6583 and [S II] λ6717/6731 lines which may be a positive indication of shock ionisation in the spectrum of V445 Pup (Woudt et al. 2009). This may not be the case with V445 Pup as research by Allen et al. (2008) suggest that in some symbiotic stars, the density may be too high for [S II] to exist. As they only created shock models for velocities less than 1000 kms $^{-1}$ these models will have to be adapted to the higher velocities observed in V445 Pup in order to determine whether [S II] is to be expected in the spectrum.

Three years after maximum brightness, Lynch et al. (2004) observed a thermal continuum emission using 0.9 - 2.5 μm observations. They also identified two narrow helium lines, probably originating from the hot interior region of the nova when viewed through the dust shell. At this epoch, no He II or coronal lines were identified in the near-infrared spectra (Lynch et al. 2004). They reasoned that this was because the ionising source was not hot enough and there was no hard radiation from the shell until later after outburst. According to their near-infrared observations on 16 November 2005, no more thermal dust emission was observed.

Later post-outburst spectra, observed five to six years after peak brightness, show a nebular ionised spectrum with emission lines of He I, [O I], [O II], [O III] and a very weak continuum (Woudt et al. 2009). This spectrum is analysed and discussed in detail in later chapters of this thesis.

1.2.4 Dust in V445 Puppis

Gehrz (1989) predicted that dust would form in fast novae, causing a sharp drop in optical brightness when the dust obscured the central system. This dust is typically not formed for many months following outburst. In the case of V445 Pup, dust is believed to have formed approximately a month after the 2000 outburst (Ashok & Banerjee 2003). Although this is unusual for novae, there have been special cases before, such as V838 Her, which developed dust just eight days after outburst (Chandrasekhar et al. 1992). The central binary star system is still obscured eleven years later as shown in Figure 1.3. This is unusual for the typical classical nova (Woudt et al. 2009).

A month after the 2000 outburst, two infrared observations were carried out, resulting in contrary discussions about how the dust was formed. These were JHK band observations on the 2 January (Ashok & Banerjee 2003) and 3-14 μm mid-infrared observations on the 31 January 2001 (Lynch et al. 2001). Lynch et al. (2001) observed a smooth featureless spectrum with no trace of the black-body distribution that would be consistent with thermal emission. They theorised that the strong infrared continuum that featured so early after the

outburst could suggest previous outbursts as it was not possible for dust to form so early. However, Ashok & Banerjee (2003) argued that, since Lynch et al. (2001) estimated that the 2000 outburst had occurred in December 2000 (a month later than their own estimates), their deductions were incorrect. Rather, Ashok & Banerjee (2003) believed there was enough time after outburst for the dust to form in January 2001. Their JHK observations revealed a massive optically-thin dust shell formation which they believed was released just after the 2000 outburst.

Using an interstellar extinction of $E(B\text{-}V) = 0.51$ mag (Iijima & Nakanishi 2008), Woudt et al. (2009) calculated a pre-outburst colour of $(V\text{-}K)^{\,0} \approx 1.58$ mag for V445 Pup. They suggested this colour could be due to the presence of substantial circumstellar reddening before the 2000 outburst.

1.3 A Spatio-kinematic Model of the Nova Shell

1.3.1 Radial Velocities of V445 Puppis

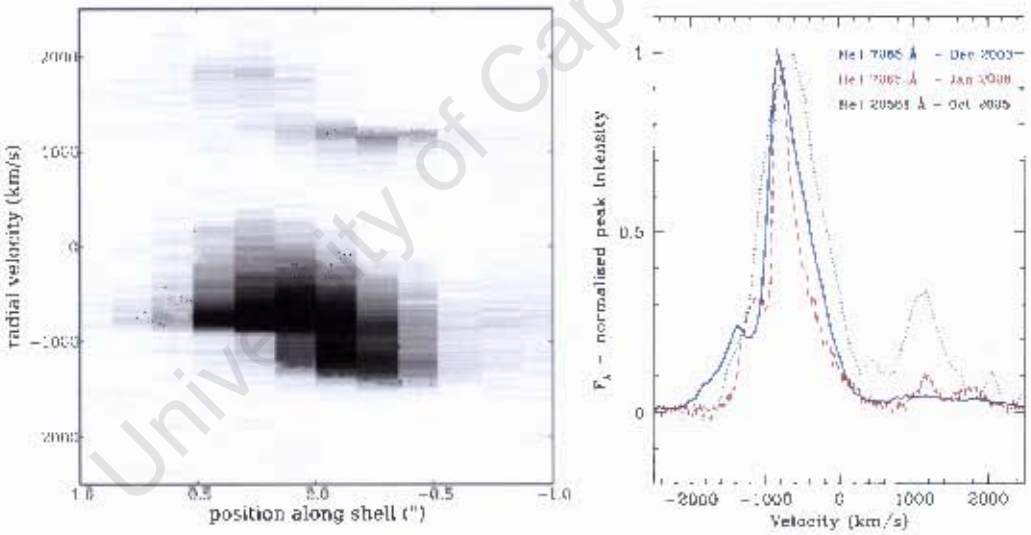

Figure 1.5: Left: Spatially resolved velocity map of the He I λ 7065 emission line. The velocity of summed spectra are sampled along the major axis running from West to East. Right: He I λ7065 emission lines from two epoch are compared with the emission line He I λ20581 (K_s band) from a different epoch (reproduced from Woudt et al. 2009).

From observations made in 2006, Woudt et al. (2009) were able to measure radial velocities of the He I λ7065 emission line along the major axis of V445 Pup. The He I λ7065 line has two components, a dominant blue-shifted component and a weaker red-shifted component, as illustrated in Figure 1.5. These respectively correspond to the material in the nova that is approaching the observer, and the receding material observed through the lobes. A

slight shift in the average velocities, moving from West to East in the shell, is also observed. This corresponds to a slight inclination to the line-of-sight, with the polar axis of the SW lobe inclined away from the observer and the polar axis of the NE lobe pointed towards the observer. From the data, Woudt et al. (2009) deduced radial velocities of the red-shifted and blue-shifted components for the NE lobe of $\sim +1140$ km s^{-1} and ~ -1270 km s^{-1}, respectively; and for the SW lobe $\sim +1720$ km s^{-1} and ~ -760 km s^{-1}, respectively. The average of the mean radial velocities for each lobe is therefore $v_r = +210$ km s^{-1} which agrees with the systematic velocity of 224 ± 8 km s^{-1} found by Iijima & Nakanishi (2008).

Woudt et al. (2009) modeled the velocity profile of V445 Pup using a bipolar velocity field model (Solf & Ulrich 1985) on the He I λ7065 emission line. Solf & Ulrich (1985) describe the model using the equation:

$$v_{exp}(\psi) = v_e + (v_p - v_e)\sin^{\alpha}(|\psi|) \tag{1.2}$$

where ψ is the latitude angle (with the poles at $\psi = 90°$ and the equator at $\psi = 0°$). v_e is the equatorial velocity, v_p is the velocity at the poles and α is the bipolarity degree where a larger α implies a stronger bipolarity.

The equatorial velocity was kept constant at ~ 500 km s^{-1}, as this is the velocity of the optically thick outflow deduced by Iijima & Nakanishi (2008) from the blue-shifted P Cygni absorption components. Woudt et al. (2009) found that the nova had a very large polar outflow velocity of 6720 ± 650 km s^{-1} and that, for a range of models, V445 Pup comprises a bipolar shell aligned along the plane of the sky and an orthogonal dust disc aligned along line-of-sight. They found that the inclination of the bipolar shell was $i_{shell} = 3.9 \pm 0.4$ ° (Woudt et al. 2009).

1.3.2 The Distance to V445 Puppis

From early outburst observations, Wagner et al. (2001) estimated that the distance to V445 Pup had an upper limit of 3 kpc. Their result was derived using the the equivalent width of the interstellar absorption band at 5780 Å. They also deduced an interstellar reddening of $E(B\text{-}V) \leq 0.8$ mag. By comparing the absolute magnitude of their theoretical light curves with their observed apparent magnitude, Kato & Hachisu (2003b) calculated a distance of around 640 pc or 700 pc, depending on the model. This agreed with the upper limit estimation from Wagner et al. (2001).

Based on the upper limit of 3 kpc, Ashok & Banerjee (2003) used extinction maps from Neckel & Klare (1980) and the relation $A_V = 3.1\ E(B\text{-}V)$ (Koornneef 1983) to deduce a reddening of $E(B\text{-}V) = 0.25$ mag. They confirmed this result by comparing photometric UBV data, taken by Wooden (1970), of 110 stars in a 5 x 5 degree field surrounding V445 Pup.

As these stars have known spectral classes, and therefore known intrinsic $(B\text{-}V)_o$ colours, they could calculate the excess colour $E(B\text{-}V)$ from the star's observed $(B\text{-}V)$ colours.

Using a theoretical light curve model and the assumption of black body radiation from the nova's photosphere, Kato & Hachisu (2003b) deduced a distance of $d \leq 1$ kpc. They later revised their model and distance estimate as new considerations came to light. Iijima & Nakanishi (2008) observed Na I doublet absorption lines at velocities of 16 $\mathrm{km\,s^{-1}}$ and 73.5 $\mathrm{km\,s^{-1}}$. This implied that V445 Pup was located in or beyond the Orion Arm of the Milky Way with a distance that could be as large as 3.5 kpc $\leq d \leq$ 6.5 kpc, contrary to earlier estimates. Iijima & Nakanishi (2008) further deduced that $E(B\text{-}V) = 0.51$ mag, which was consistent with Wagner et al. (2001) but greater than the $E(B\text{-}V) = 0.25$ mag suggested by Ashok & Banerjee (2003). By considering these larger distance estimates and the observed colour indexes during outburst, Kato et al. (2008) revised their model to consider a free-free emission dominated light curve based on an optically thick wind theory (Kato & Hachisu 2003b).

The latest distance estimate, based on the expansion parallax of V445 Pup, is $d = 8.2 \pm 0.5$ kpc calculated by Woudt et al. (2009). They reached this result using combined adaptive optics spatio-kinematic observations and the velocity model described in Equation 1.2. (Solf & Ulrich 1985). Using this model, they also calculated a bulk velocity of $v_p = 6720 \pm 650$ $\mathrm{km\,s^{-1}}$. This is relatively fast when compared to hydrogen-rich novae, although not an unreasonable result. The recurrent nova U Sco has very high velocities with a full width at zero intensity (FWZI) of ~ 10000 $\mathrm{km\,s^{-1}}$ (Kato & Hachisu 2003a) and RS Oph has a similarly high bulk velocity of $v_p = 5600 \pm 1100$ $\mathrm{km\,s^{-1}}$ (Bode et al. 2007).

Woudt et al. (2009) used their distance estimate of $d = 8.2 \pm 0.5$ kpc to place the nova at a height of 313 ± 19 pc below the Galactic plane. Therefore, they could use the IRAS/DIRBE Galactic reddening maps (Schlegel et al. 1998) to deduce the Galactic reddening towards V445 Pup. By comparing the location of V445 Pup to open clusters within 10 degrees of it, they were able to deduce a Galactic reddening of 0.51 mag $\leq E(B\text{-}V) \leq 0.68$ mag. By using the equivalent widths of the Na doublets observed by Iijima & Nakanishi (2008), they could infer that $E(B\text{-}V) = 0.68$ mag was the maximum limit (Woudt et al. 2009).

The distance to V445 Pup is not well known and current estimates remain fairly uncertain. As distance is used in determining possible parent populations, it is important that improved spatio-kinematic models are produced with better spectral sampling and higher angular resolution. It is possible that the observed material seen at high resolution is not associated with the true expansion velocity of the shell, but rather with a post-shock ionisation front instead. This is the critical pitfall of any expansion parallax and remains a problem, even with perfectly resolved images.

Woudt et al. (2009) believe it is unlikely that their distance measurement of 8.2 kpc was severely underestimated, as a greater distance would imply velocities approaching those of a supernova rather than those of a classical nova. They suggest that more detailed (magneto)hydrodynamic simulations (e.g. Dennis et al. 2009) are needed in order to estimate by what amount the expansion parallax could underestimate the true distance to V445 Pup.

1.3.3 The Mass of the White Dwarf

The mass of the white dwarf in V445 Pup has so far been poorly determined as it has only been inferred from models and not directly measured. Using their initial blackbody emission model, Kato & Hachisu (2003b) inferred a very massive white dwarf of the order $M_{wd} \geq 1.33\,M_{\odot}$. They found that this mass provided the best fit for pre-outburst light curves using VSNET data. Using their revised free-free emission light curve model, they later found that the mass was closer to $M_{wd} \geq 1.35\,M_{\odot}$ (Kato et al. 2008).

1.4 V445 Puppis as a SN Ia Progenitor

1.4.1 The SNe Ia

Type Ia supernovae (SNe Ia) are important astronomical phenomena, as they produce heavier elements such as iron, and can be used as standard candles in determination of cosmological distances. This is due to the luminous homogeneity of their stellar explosions (Mazzali et al. 2011). Much research is dedicated to the identification of the progenitor binary system of SNe Ia. The favoured progenitor scenario is a CO white dwarf that accretes hydrogen from a companion donor star (Branch & Nomoto 2007). As the accreting CO white dwarf in SNe Ia are all at the Chandrasekhar limiting mass, this leads to the homogeneity of the explosions (Livio 2000). In a second scenario, the supernova Ia is due to the merger of two white dwarfs with a combined mass that exceeds the Chandrasekhar limit (Mazzali et al. 2011).

1.4.2 V445 Puppis: a SN Ia Progenitor?

It has been suggested that V445 Pup is a candidate progenitor of the type Ia Supernova (Kato et al. 2008) or the sub-luminous type .Ia supernova (Bildsten et al. 2007). In systems with He donors, the accreted helium accumulates on the surface of the white dwarf (Kato & Hachisu 1999). Due to the high accretion rate of several times $10^{-7}\,M_{\odot}\,yr^{-1}$ estimated for V445 Pup, an ignition mass greater than $10^{-5}\,M_{\odot}$, and a massive WD mass that is greater than $1.35\,M_{\odot}$, the helium flashes are very weak. Therefore, in the models of Kato et al. (2008), less than 50% of the envelope is blown off, while the rest accumulates on the

white dwarf surface. After several helium flashes, the growing white dwarf mass reaches the Chandrasekhar limit, resulting in either a supernova explosion or an accretion-induced collapse to a neutron star (Kato et al. 2008).

Woudt et al. (2009) investigated the possibility of V445 Pup having outbursts prior to one in 2000. Using plate archives at the Harvard Smithsonian Center for Astrophysics, they were unable to identify any outbursts in the time frame 1897-1955, even though V445 Pup was frequently identified at a constant brightness and the observations were well-sampled. They were also unable to find any pre-outburst spectra or an orbital period for the system that could give further clues as to the nature of the progenitor and its eventual outcome.

In a recent paper, Li et al. (2011) suggest that a V445 Pup like object is unlikely to be the progenitor of type Ia supernova SN 2011fe. Using historical images, they could not identify the progenitor system of SN 2011fe and thus were able to place an upper limit on the luminosity of the potential progenitor. This luminosity is 10 - 100 times fainter than previous SNe Ia progenitor limits and is therefore more suited to doubly-degenerate systems than to singly-degenerate systems. Although this excludes V445 Pup, lower luminosity helium novae are still possible candidates. Li et al. (2011) go on to state that given how diverse the class of SNe Ia are observed to be, multiple progenitor channels, including singly-degenerate systems, are still possibilities for this class.

1.5 Thesis Outline

Similar to observations made by Woudt et al. (2009), this dissertation presents data observed with the IMACS IFU instrument in 2006 and 2007. However, the analysis of Woudt et al. (2009) only considered the velocity profiles along the major axis for one night of observation. The research conducted in this dissertation considers the full spatial velocity map for several dominant lines over two nights. Improved estimates of radial velocities are reached, and ultimately these results can be used in one-dimensional hydrodynamic models and to constrain better estimates of the distance.

In this thesis, the IMACS IFU, situated on the Magellan Telescope at Las Campanas in Chile, was used to make multi-epoch spectographic observations of V445 Pup. These observations and the IFU spectrographic observing techniques are discussed in Chapter 2. The reduction techniques, using various IRAF routines, and the data cube reconstruction process are reviewed in Chapter 3. In Chapter 4, spectral emission from the nova is investigated in both intensity and velocity space, and the results are modeled in Chapter 5. Also, the changes from 2006 to 2007 and an excess of oxygen are discussed in detail. Finally, in Chapter 6, future prospects concerning the use of the results from this thesis are reviewed.

Chapter 2

Observations

Multifibre spectrographic observations of V445 Pup and its surroundings (including standard stars and a planetary nebula) were made over five nights in 2006 and 2007 using the IMACS IFU on the Magellan Telescope at Las Campanas Observatory in Chile. The first two observations were made on the 4 and 5 January 2006 and the last three observations were made a year later on the 8, 9 and 10 January 2007. Of these, only spectra from two nights (4 January 2006 and 8 January 2007) were chosen for further analysis as they both reach similar depth and were observed under excellent weather conditions.

2.1 The Magellan Telescope

Figure 2.1: The 6.5 m twin Magellan Telescopes situated at Las Campanas Observatory in Chile. (Credit: *http://www.lco.cl/telescopes-information/magellan/telescopes-information/magellan/*)

The multi-epoch spectrographic observations reduced and analysed in this dissertation were made using an Integral Field Unit on the Magellan I, or Walter Baade Telescope. Built by the Carnegie Institution of Washington, the 6.5 metre telescope is situated at the Las Campanas Observatory in Chile alongside its twin telescope, the Clay Telescope. Both telescopes have an alt-azimuth design with principal foci of f 11 at the Nasmyth positions and f 15 foci at the Cassegrain positions. The f 11 focus is in a Gregorian configuration, which assists with the collimator optics performance in the wide-field spectrograph IMACS (Dressler et al. 2011). The primary mirrors consist of f 1.23 paraboloid mirrors coated with aluminium surfaces. The Magellan telescopes are shown in Figure 2.1.

2.2 Spectroscopy

2.2.1 Integral Field Unit Spectroscopy

Integral Field Unit (IFU) spectroscopy is the ideal tool for spectral imaging of extended sources, which gives it a huge advantage over traditional long-slit spectroscopy. In IFU spectroscopy, data are collected from a two-dimensional (2D) field of view and then converted into a three-dimensional (3D) data cube format. This data cube consists of two spatial axes (right ascension (RA) and declination (DEC), or x and y) and a dispersion axis which is in wavelength or velocity units. With an IFU, spectra are systematically recorded from all over the field of view. Therefore, this method of spectroscopy can be used to create spatial maps of your target for specific wavelength or velocity regions, as well as line ratio maps. The IFU is designed to be primarily used in the optical red or near-infrared regions, as it is difficult to manufacture optical fibres that transmit blue light as effectively as red light.

Integral field spectroscopy consists of two components; namely a spectrograph, which disperses the spectra, and the IFU which divides the 2D spatial plane into a continuous array. The three main types of IFUs are illustrated in Figure 2.2.

In a lenslet array, light from an image is separated by a microlens array, where it is condensed into small individual points. A spectrograph then disperses these points into spectra. As the points are small, the spectra can be aligned at an angle with no overlapping, provided that the spectra are not too wide.

In a lenslet and fibre IFU, light from the image falls over a 2D fibre bundle array. Light is transferred via the fibres to a continuous slit or slits, which then disperses it into row-stacked spectra. As the fibres are cylindrical, they do not cover the field entirely. Therefore, adjacent square lenses are used to focus light onto the fibres, while still covering the entire field.

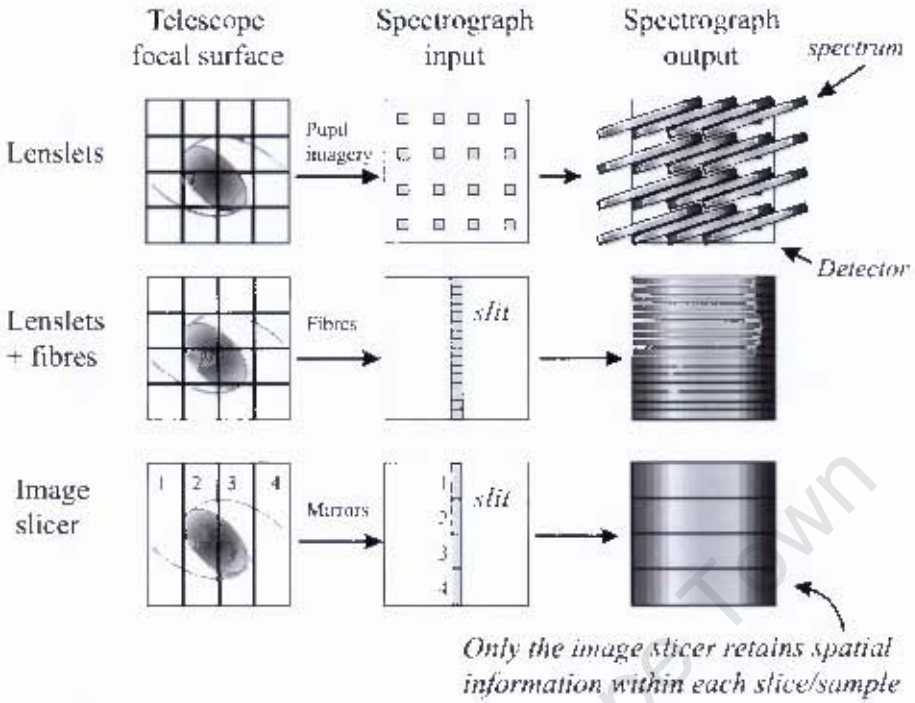

Figure 2.2: The three main methods used in integral field spectroscopy (Allington-Smith & Content 1998).

The image slicer IFU consists of strips of mirrors that focus the incoming light of the target onto a secondary set of mirrors. The second set of mirrors aligns the light continuously along a dispersing slit. As mirrors are inherently achromatic and easy to cool, these IFUs are well suited to infrared spectroscopy.

The raw data produced by an IFU contain several hundred spectra which need to be reduced and analysed. Once these spectra are extracted, they can be reassembled into a data cube. In Figure 2.3, the IFU process is illustrated using data analysed in this dissertation. The background image is a wide-field image of V445 Pup and its surroundings (30′ x 30′), based on data from the Digitised Sky Survey 2 (Credit: *ESO/Digitized Sky Survey 2*). V445 Pup is projected onto a 16 x 25 hexagonal array of fibres, sampled at 0″.2. Each of the 400 spatial pixels, or spaxels, shows the summed intensity from a portion of the spectra that lies along the third dimension in the data cube, and the spectrum for one of the spaxels covering V445 Pup is displayed in the bottom inset of Figure 2.3.

2.2.2 IMACS IFU on the Magellan Telescope

The Inamori Magellan Areal Camera and Spectrograph (IMACS) (Schmoll et al. 2004) is a multi-object spectrographic instrument designed to be used on the Magellan I Telescope,

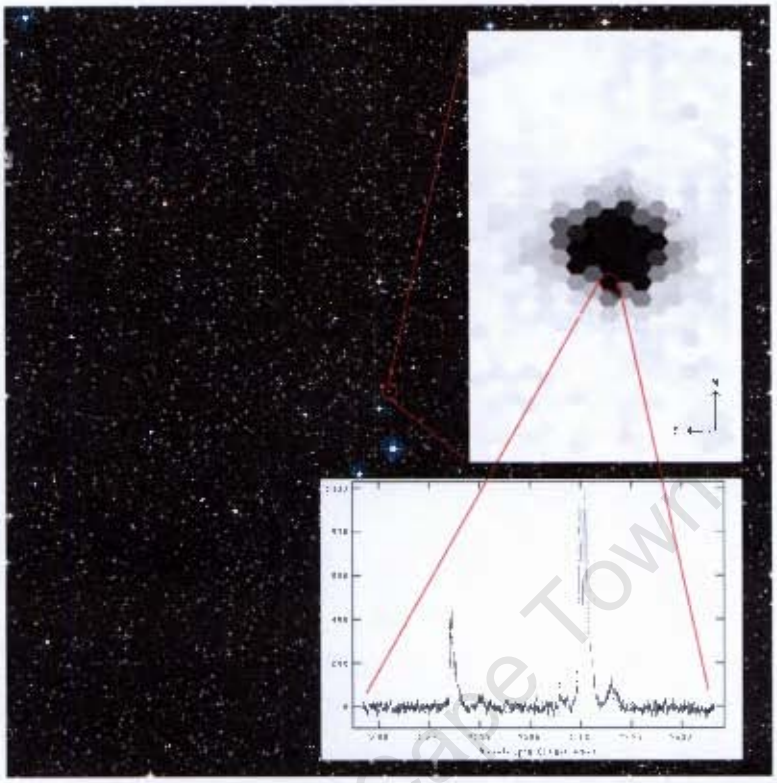

Figure 2.3: Illustration of integral field spectroscopy using a Digitised Sky Survey image of V445 Pup and observations analysed in this dissertation. The top inset is a summed on-sky projection of the He I λ7065 emission in the -900 km s^{-1} to -700 km s^{-1} range. Each aperture can be expressed as a two-dimensional spectrum as indicated in the lower inset. North East configuration is as indicated and the background field is 30′ by 30′. (Background credit: *ESO/Digitized Sky Survey 2*.)

placed at the Nasmyth focus. It has two cameras; a f/2.66 long camera for 17 arcmin fields sampled at 0.2 arcsec, and a f/1.49 camera for 27 arcmin fields sampled at 0.4 arcsec (Dressler et al. 2011). Both cameras can work in spectroscopic or imaging modes, and feed through to a 8192 x 8192 pixel CCD array. This four by two CCD array (each CCD has a dimension of 2048 x 4096 pixels) is shown in Figure 2.4. While the long camera uses grating dispersers for spectrographic imaging, the short camera uses grisms of various low dispersions. The spectral resolution is $R = \lambda/\Delta\lambda < 10000$ for the long camera and $R = \lambda/\Delta\lambda \leq 1800$ for the short camera.

Observations of V445 Pup were made using the IMACS IFU (Schmoll et al. 2004) which is a fibre lenslet IFU built specifically for the IMACS spectrograph, covering the spectral range from 400 nm to 900 nm with a spectral resolution of $R < 1800$. The IMACS IFU consists of two equally sized 5″ by 7″ rectangular fields, separated by ∼1 arcmin. The configuration of a separate object and background field allows for beam switching by nodding

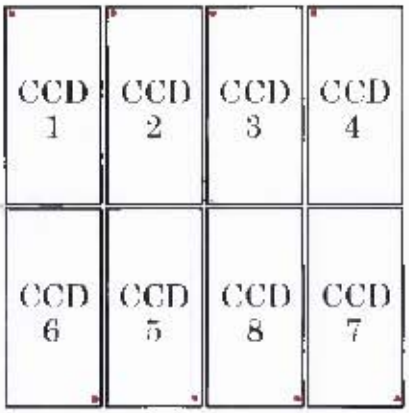

Figure 2.4: Arrangement of the eight CCDs on the IMACS spectrograph. The dot indicates the position of pixel(0,0) in each CCD. (Credit: *http://obs.carnegiescience.edu/Code/cosmos/Data.html*)

the telescope. Each field consists of an array of 1000 fibres, with each fibre sampled at 0.″2. Half of the adjacent fibres project light onto four of the eight CCDs. Similarly, the other half of the fibres project onto the other four CCDs. The mapping of these fields is illustrated in Figure 2.5, which is reproduced from Schmoll et al. (2004). In this figure, the object and background fields are alternated in blocks of 50 fibres each. This helps to avoid any large changes in the behaviour of the spectrograph when subtracting sky from the target images during reductions. A few manufacturing errors with the IMACS CCDs need to be considered when reducing; namely, the eighth and ninth Background Blocks need to be switched and the second Object Block contains two broken fibres.

2.3 Multi-epoch IFU Spectroscopy of V445 Puppis

Spectroscopic observations were taken over five nights in two years (2006 and 2007) using the IMACS IFU on the Baade Telescope by Professor Danny Steeghs using the Grism 600. This dispersing element covers the optical wavelength range from 4000 Å to 9000 Å with an expected pixel scale of 0.38 Å/pixel (Woudt et al. 2009). The field of view (5.″00 by 4.″15) is ideal for covering the nova which is approximately 2″ - 3″ across. The sampling of 0.″2 is also ideal for attempting to resolve parts of the nova shell. A central portion of the long camera, consisting of the Object and Background Blocks 7-14, was used (See Figure 2.5).Therefore, each image contained 400 fibres, and thus 400 spectra to extract.

In 2006, V445 Pup was observed on two nights, 4 January and 5 January, and the nova was positioned in the Background Blocks (with the Object Blocks containing sky exposures). In 2007, the nova was observed over three nights: 8 January, 9 January and 10 January and V445 Pup was conversely positioned in the Object Blocks (with the Background Blocks

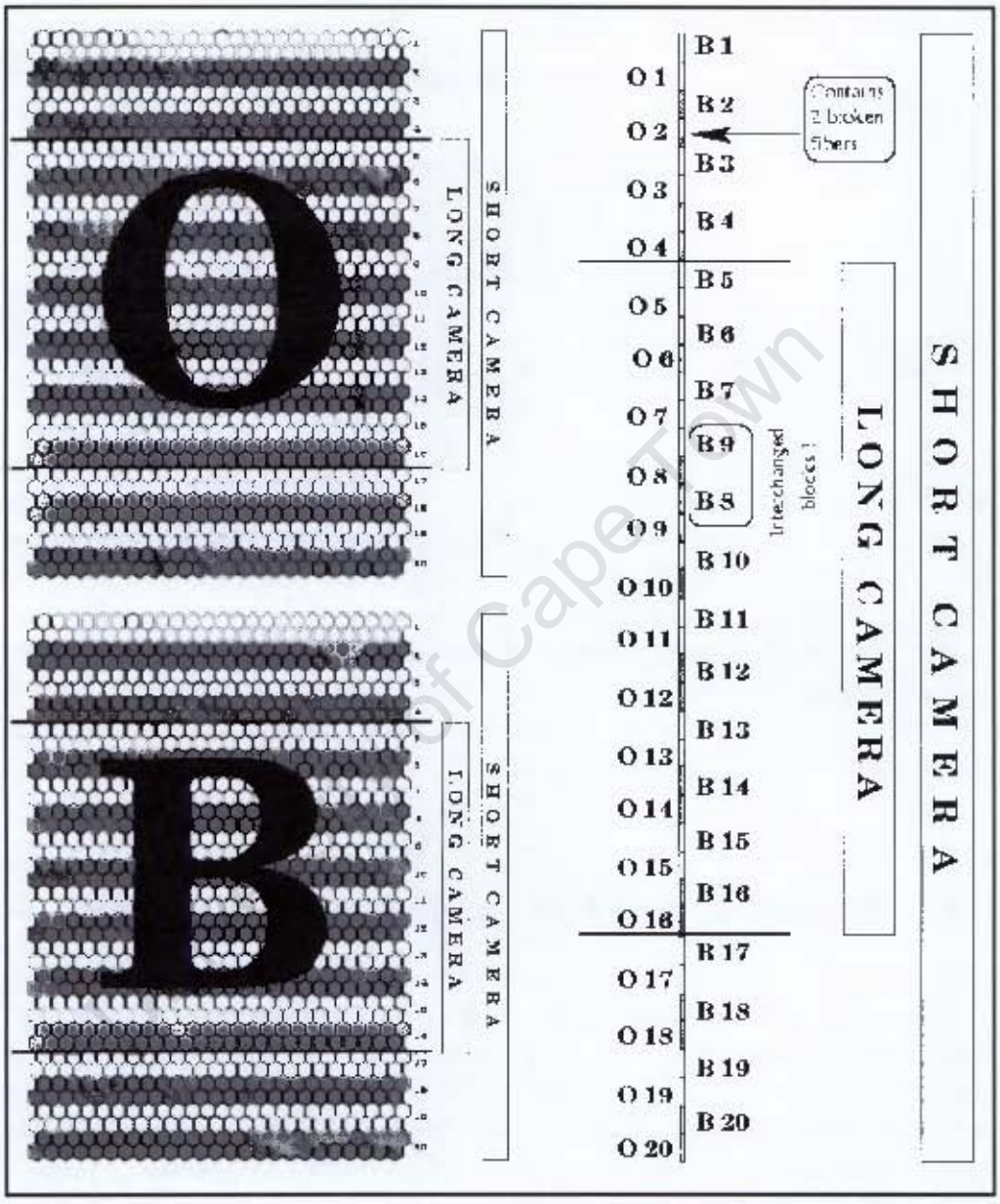

Figure 2.5: Mapping of the IMACS IFU. Object(O) and Background(B) blocks are alternated on two rectangular fields, sampled at 0″2. The long camera is 4′15 x 5′00 and the short camera is 6′92 x 5′00 (Schmoll et al. 2004).

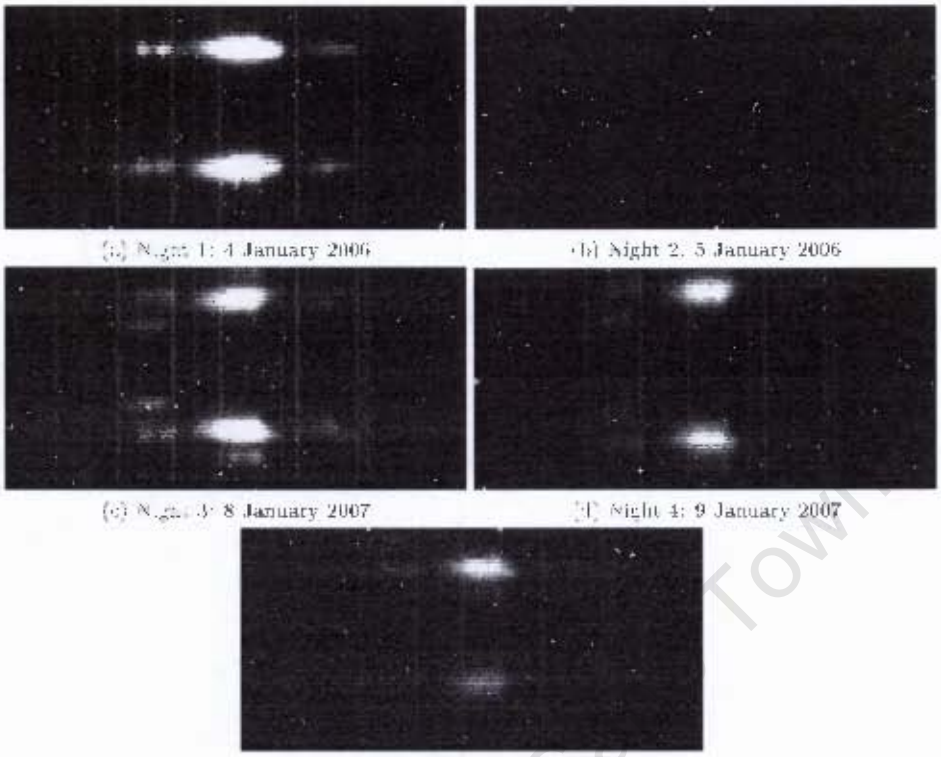

(a) Night 1: 4 January 2006 (b) Night 2: 5 January 2006

(c) Night 3: 8 January 2007 (d) Night 4: 9 January 2007

(e) Night 5: 10 January 2007

Figure 2.6: Nightly sample spectra of raw target exposures from Background (in 2006) and Object (in 2007) Block 11 in CCD 1. The spectra are centred on the [O II] λ7320/7330 doublet emission line. The dispersion axis is along the x-axis.

now containing sky exposures). Along with V445 Pup, observations were also made of the planetary nebula, IC2165, and the standard stars; GD50, LTT2415 and LTT3864. The full observing log for all five nights can be seen in Appendix A.

In Figure 2.6, a comparison is made of a small subset of spectra consisting of 50 spectra from Object Block 11 centred on the [O II] λ7320/7330 doublet emission line from each of the nights. The images have not yet been reduced and are therefore covered in cosmic rays that still need to be subtracted. Exposures of V445 Pup were either 1800s for the first four nights, or 1200s for the last night. The seeing for each night is shown in Figure 2.7. Although all of the images come from the same block, there is a chance that the camera was moved between nights and a different part of the nova is being looked at. This being said, there was no evidence of a signal in any of the spectra from CCD 2. This is probably due to the extremely variable seeing as shown in Figure 2.7 and cloudy weather on this night.

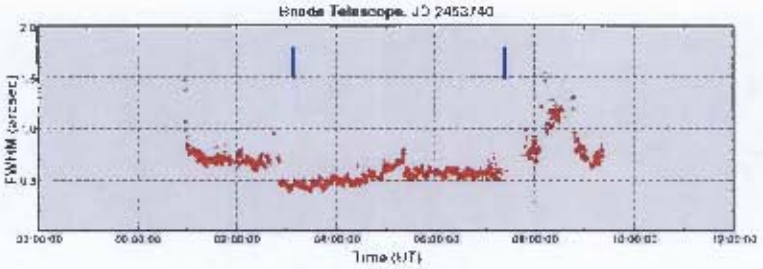

(a) Night 1: 4 January 2006

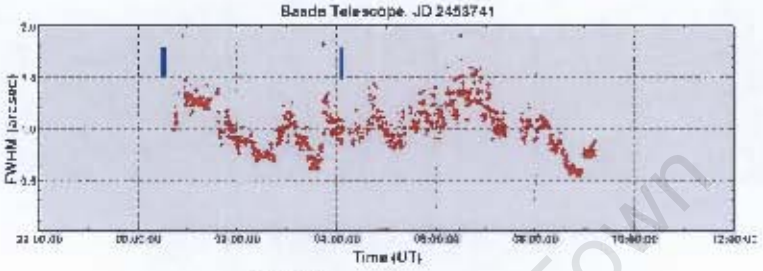

(b) Night 2: 5 January 2006

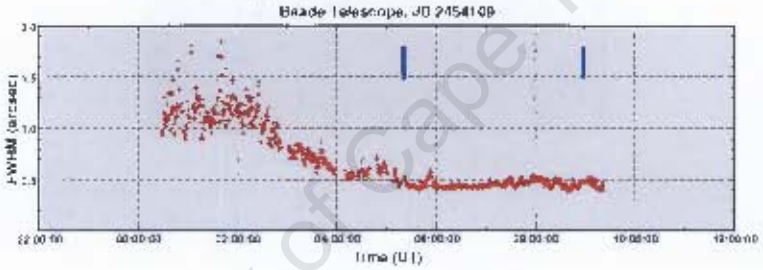

(c) Night 3: 8 January 2007

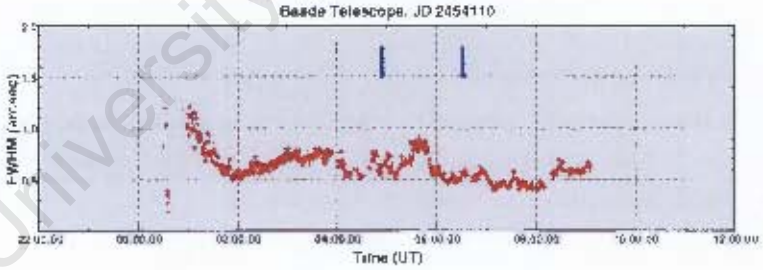

(d) Night 4: 9 January 2007

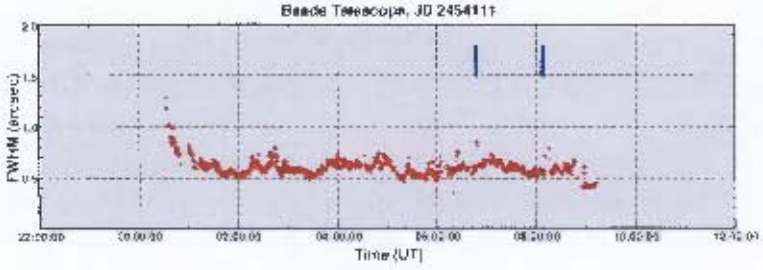

(e) Night 5: 10 January 2007

Figure 2.7: Seeing measured on the respective observing nights using the CCD guide camera on the Baade Telescope. The camera uses a *RC*610 filter and raw FWHM values are corrected for airmass assuming, $\mathrm{FWHM}_{corr} = \mathrm{FWHM}_{observed}/\mathrm{airmass}^{0.6}$. Chile's timezone is UT - 4 hours. V445 Pup was observed between the times indicated by blue vertical markers in each panel. (Credit: *www.lco.cl/observer-information/environmental-information/magellan-telescopes-guide-camera-seeing*)

Table 2.1: Observations of V445 Pup in 2006

Object	UT Start	Exposure Time (s)	RA (hh:mm:ss)	DEC (dd:mm:ss)	Airmass
V445 Pup	03:11:31	1800	07:37:56.1	-25:57:33.7	1.144
V445 Pup	03:43:10	1800	07:37:56.1	-25:57:33.0	1.079
V445 Pup	04:14:43	1800	07:37:56.0	-25:57:34.0	1.036
V445 Pup	04:50:46	1800	07:37:55.8	-25:57:46.1	1.009
V445 Pup	05:22:26	1800	07:37:56.6	-25:57:52.9	1.001
V445 Pup	06:16:41	1800	07:37:56.7	-25:57:50.8	1.024
V445 Pup	06:48:18	1800	07:37:56.6	-25:57:50.5	1.06

(a) Night 1: 4 January 2006

Object	UT Start	Exposure Time (s)	RA (hh:mm:ss)	DEC (dd:mm:ss)	Airmass
V445 Pup	02:33:37	1800	07:37:57.2	-25:57:44.1	1.244
V445 Pup	03:05:34	1800	07:37:57.3	-25:57:43.1	1.149
V445 Pup	03:37:07	1800	07:37:57.3	-25:57:42.1	1.083

(b) Night 2: 5 January 2006

2.3.1 2006 Observations

The first night (4 January) was the clearest of all five nights. This can be seen in Figure 2.6a, where the spectral feature has the greatest overall intensity. The seeing was relatively stable at around 0″5 during the duration of exposures from 3:11 am to 6:48 am (UT time). This is shown in Figure 2.7a which displays the seeing conditions during our observations. Observations from the first night included V445 Pup, dome flats, arcs, the planetary nebula IC2165, the standard star GD50 and twilight flats. On this night, seven exposures of 1800 seconds each were made of V445 Pup. After five target exposures were taken as the telescope was moving through the meridian, the observers noticed that the target had moved off the central position of the CCD. After a few spot images, they repositioned the nova to the centre of the CCD. Hence the 20″ difference seen in the declination between observations on the 4 January in Table 2.1.

Unfortunately, on the second night (5 January), the seeing was very variable the whole night and no spectral features were visible in the spectra. This can be seen in Figures 2.7b and 2.6b, respectively. Also, only three exposures were made of V445 Pup during the night.

Table 2.2: Observations of V445 Pup in 2007

Object	UT Start	Exposure Time (s)	RA (hh:mm:ss)	DEC (dd:mm:ss)	Airmass
V445 Pup	05:23:03	1800	07:37:59.8	-25:56:35.9	1.003
V445 Pup	06:06:56	1800	07:37:59.8	-25:56:33.9	1.029
V445 Pup	06:43:57	1800	07:37:59.8	-25:56:33.5	1.076
V445 Pup	07:16:20	1800	07:38:00.0	-25:56:33.8	1.141
V445 Pup	07:52:44	1800	07:38:00.1	-25:56:35.7	1.247
V445 Pup	08:25:05	1800	07:38:00.2	-25:56:37.8	1.384

(a) Night 3: 8 January 2007

Object	UT Start	Exposure Time (s)	RA (hh:mm:ss)	DEC (dd:mm:ss)	Airmass
V445 Pup	04:59:27	1800	07:37:59.3	-25:56:37.9	1.002
V445 Pup	05:31:48	1800	07:37:59.5	-25:56:36.0	1.008
V445 Pup	06:04:12	1800	07:37:59.5	-25:56:34.5	1.03

(b) Night 4: 9 January 2007

Object	UT Start	Exposure Time (s)	RA (hh:mm:ss)	DEC (dd:mm:ss)	Airmass
V445 Pup	07:09:02	1200	07:37:54.4	-25:57:30.0	1.142
V445 Pup	07:31:20	1200	07:37:54.5	-25:57:30.3	1.203
V445 Pup	07:53:39	900	07:37:54.6	-25:57:30.4	1.28

(c) Night 5: 10 January 2007

2.3.2 2007 Observations

Night 3 (8 January) was the clearest night in 2007. It is shown in Figure 2.7c that the seeing was very stable and less than 0″5 when the exposures were being taken from 5:23 am to 8:25 am (UT time). Along with V445 Pup; dome flats, the standard star, LTT2415 and twilight flats were observed. Six exposures of V445 Pup were made on this night.

Only three exposures of V445 Pup were made on both nights 4 and 5 (9 and 10 January respectively). Night 4 was cloudy and the seeing was very unstable during exposure times from 4:59 am to 06:04 am (UT time). On night 5, the seeing was better and, from 7 am to 8 am, varied between 0″5 and 0″7. However these conditions were still not as good as either night 1 or 3.

2.3.3 Final Data Set

In this dissertation, I have chosen to reduce and analyse only the high quality data of night 1 (4 January 2006) and night 3 (8 January 2007). These observations are approximately equal in quality and length, and allow for a good comparison of the spectral features of V445 Pup in 2006 and 2007.

Chapter 3

Data Reduction and Analysis

When working with raw data from the IMACS IFU, several hundred spectra need to be carefully reduced, extracted and processed into a data cube format. As no publically available pipeline exists, I had to process all of the reductions using standard IRAF* routines. Due to the complex nature of the data reduction procedure, I initially extracted a small subsample of spectra from CCD 1 to test the extraction routines. Once this extraction was processed successfully, I expanded the reduction procedure to run on the full dataset and assembled the data cube for analysis. The extraction process was also performed on spectra taken of the planetary nebula IC2165 to verify the accuracy of the wavelength solution and quantify the uncertainties in the radial velocities.

3.1 Extractions of Spectra

3.1.1 Extractions of a Small Subsample

The small subsample, consisting of 3 flats, 2 arcs and 1 object exposure, were taken during observations on the first and clearest night (4 January 2006). Each image contained 100 spectra from Object and Background Block 11, covering the [O II] λ7320/7330 doublet line. V445 Pup was centrally positioned across the Background Blocks and the Object Blocks consisted of sky exposures.

I reduced the raw data using tasks from the IRAF packages `hydra`, `imred`, `ccdred`, `stsdas`, `imutil` and `dohydra`. The task, `setinstrument` resets the instrument identification image header in order to be able to analyse multifibre data, which in turn allows the task `ccdproc` to trim and bias subtract the images. Although the images contain two bias regions; a strip along the top of the image and a strip along the right side of the image,

*IRAF is distributed by the National Optical Astronomy Observatories, which are operated by the Association of Universities for Research in Astronomy, Inc., under cooperative agreement with the National Science Foundation. (Tody 1993)

only the bias from the overscan region along the side was subtracted. In order to accurately define the bias and trim regions, the command `implot` was used to plot either a line or column from which the regions were measured directly. I then used the task `ccdproc` to fit a spline3 function of order 3 to the overscan region and subtracted this from the rest of the untrimmed image.

All the images contained a significant amount of cosmic rays. In order to subtract them, the slow but thorough `L.A.Cosmic` task in the `stsdas` package was run. This task works very well and minimal loss of line definition can be seen. Developed by van Dokkum (2001), the program uses a variation of Laplacian edge detection to identify and remove cosmic rays of arbitrary size and shape. In order to achieve a good subtraction, the gain and readout noise specifications of the instrument can be input to the task. These were found from the image header of CCD 1 to be 0.9 e^-/ADU and 4.9 e^-, respectively. The before and after images of Background Block 11 in the target image can be seen in Figure 3.1.

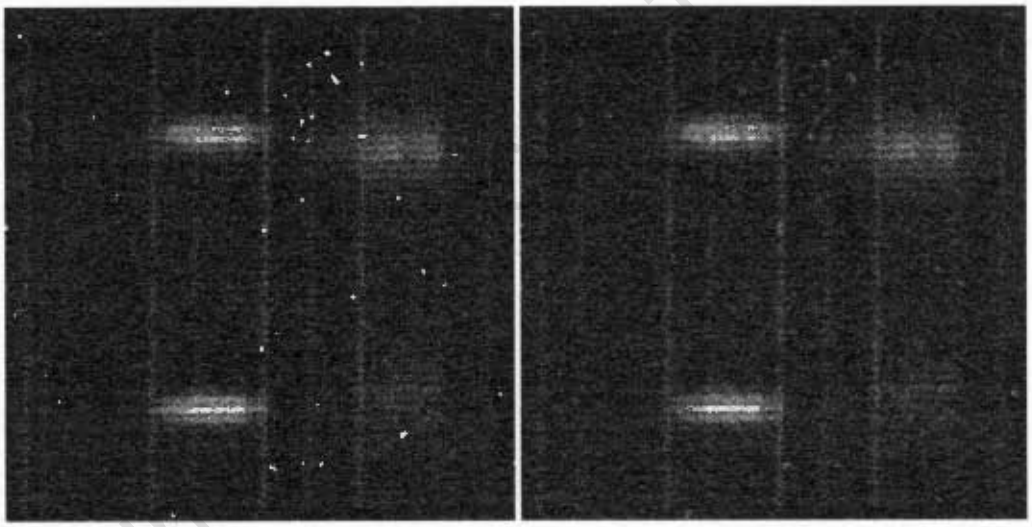

Figure 3.1: Background Block 11 of CCD 1 from the subsample targets image (Frame 84, 4 January 2006) before (left panel) and after (right panel) cosmic ray subtraction using `L.A.Cosmic` (van Dokkum 2001).

After the reductions had successfully processed the raw images, 100 spectra from the central Block 11 of CCD 1 were extracted using the multipurpose task, `dohydra`, along with its subtask, `params`. For this process, the object and sky images from Block 11 (each consisting of 50 spectra) were worked on separately.

`dohydra` first finds and extracts the relatively clearly defined apertures associated with the fibres from a flat field image. The task fits a trace that tracks the aperture positioning along the dispersion axis, and then applies this extraction matrix to the other arc and target

images. Pixel-to-pixel sensitivities in the images are corrected for by dividing the science image with an extracted uniformly-lit flat field, observed with the same instrument. This flat fielding is done in the `dohydra` task, using either a dome flat or a sky flat. Any differences in the sky throughput between each aperture across the CCD is normalised using the sky counts of each fibre in a sky flat. `dohydra` calculates a dispersion solution from the first arc spectrum which is then applied to the other arc spectra. Each arc image is associated with the appropriate target spectrum, which is in turn assigned the dispersion solution and, therefore, an appropriate wavelength scale. Finally the spectra are plotted using the task `splot`.

The size of the apertures were measured by carefully separating the peaks from the troughs using `implot` along a central column. Each aperture could be fit with a Gaussian curve that had a Full Width at Half Maximum (FWHM) of ~ 4 pixels. `dohydra` used the tasks `apfind` and `apedit` to automatically identify the 50 apertures with fixed widths of 6 pixels as seen in Figure 3.2. The trace was fit using a spline3 function of order 3 and a sky flat was used both for flat fielding and as a throughput image, fitted with a spline3 function of order 10. The aperture extraction was chosen to be weighted by the variance which uses the gain and readout noise specifications to create a Poisson CCD model that is compared to the data values. Once the spectra are extracted, the pixel axis can be calibrated into a more suitable wavelength axis. This is discussed in more detail in Section 3.2.

3.1.2 The Full Data Set

The extraction procedure used on the small subsample was expanded to run on the central eight blocks of the 12 Object and Background blocks from each of the 8 CCDs. After a visual inspection, only eight of the blocks were used as there was no signal in the remaining four blocks. Once a full spectrum was successfully extracted, the procedure was repeated for all science and calibration frames on night 1 (4 January 2006) and night 3 (8 January 2007). On night 1, V445 Pup was positioned over the Background Blocks and the background sky was positioned in the Object Blocks. Conversely, on night 3, V445 Pup was placed over the Object Blocks and the Background Blocks contained comparative sky exposures. Also, in 2007, the position angle of the spectrograph was changed so that the major axis of the nova shell was North-South aligned on the IFU.

Running the initial reductions on the other CCDs was straight-forward and, therefore, all the images were easily trimmed, bias-subtracted and cosmic-ray reduced using the same fitting parameters that was used in the subsample reductions. On the other hand, the flat fielding, throughput corrections and, in particular, aperture identifications became trickier when considering the rest of the data set. This was due to the gradual decrease in aperture clarity in CCDs 4 and 7, corresponding to the bluest portion of the dispersion axis. The apertures disappeared and blended into each other, making aperture identification very

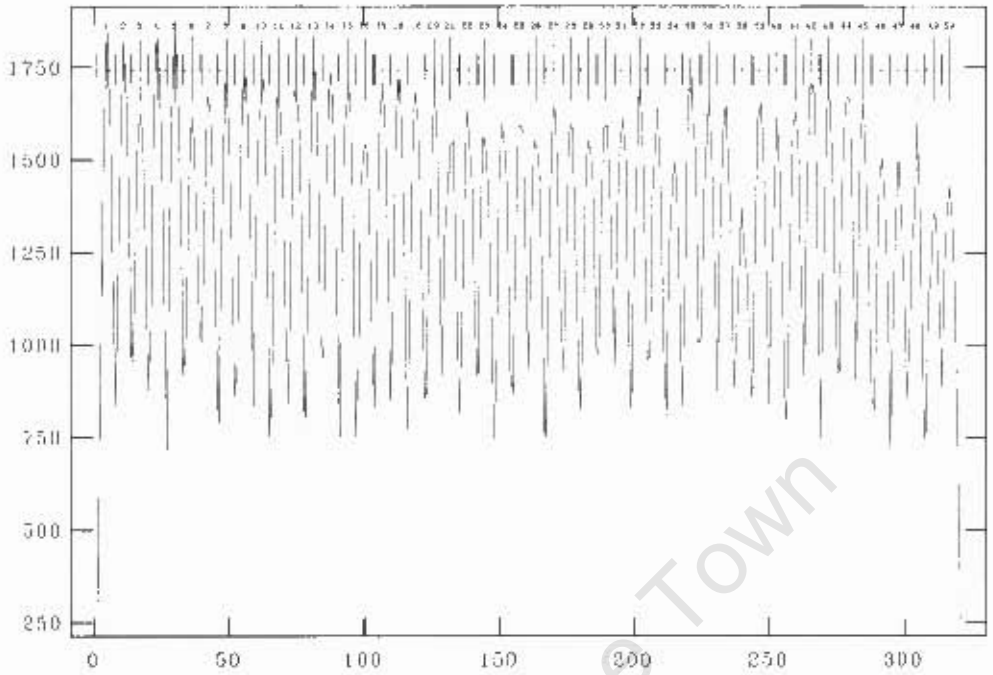

Figure 3.2: Identification of 50 apertures from the central Background Block 11 using **apfind**. The apertures are assigned a number from 1 - 50, with labeling above the apertures. The abscissa units are pixels and the ordinate units correspond to intensity.

difficult. In order to correct for this problem, the dome flats for each CCD were summed, reduced and used as aperture identification for the other images. As they were exposed in controlled settings, the summed dome flats were mostly very clear and identified the apertures well. Figure 3.3 compares the aperture identification from a twilight flat field and a dome flat in Background Block 14 of CCD 4.

The dome flats were also used as flat fields in order to correct for pixel-to-pixel sensitivities. Aperture throughput corrections were made using the flat fields taken during twilight. However, before the flats in CCDs 7 and 8 could be used, they had to be cleaned of any bad columns that added intensity spikes to the spectra . In most cases, this was done simply by interpolating the bad columns with adjacent good columns.

3.2 Wavelength Calibration

3.2.1 Calibration of a Small Subsample

In the initial subsample (Section 3.1.1), the first arc image (Frame 83 on night 1, see Table A.1) was used to identify the spectral lines for the dispersion solution. In order to adjust

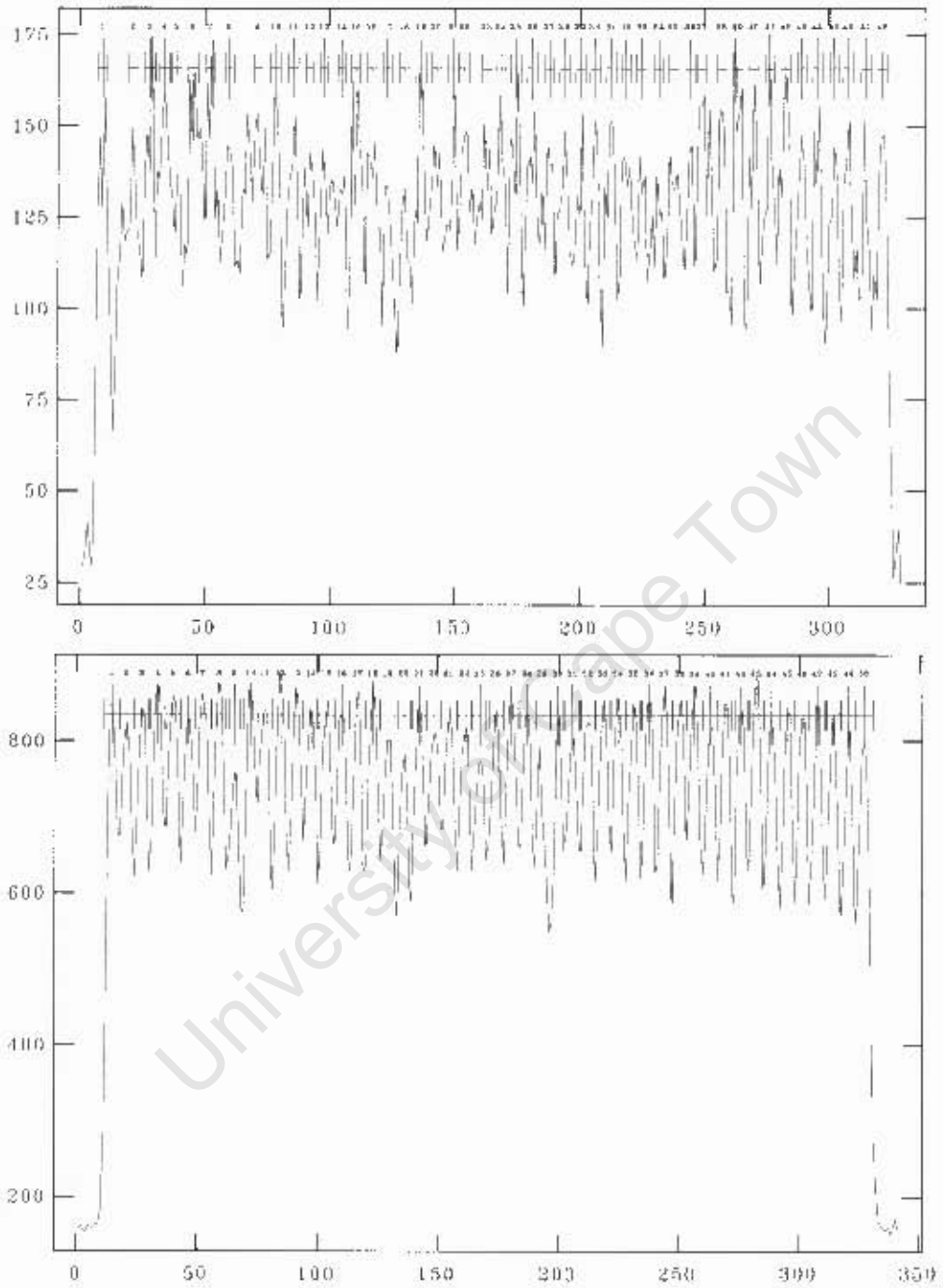

Figure 3.3: Top panel shows failed identification of 50 apertures using `apfind` on Background Block 14 from CCD 4 of an unsuitable twilight flat field. In the bottom panel, the same Background Block 14 of CCD 4 from the summed dome flats is far clearer with no aperture blending. Apertures are assigned a number from 1 - 50, with labeling above the apertures. The abscissa units are pixels and the ordinate units correspond to intensity.

the pixel scale to an appropriate wavelength scale, the unidentified emission lines in the arc were matched with those from the HeNeAr Spectral Atlas (Crosswhite 1975) which has known wavelengths in the 6850 Å to 7600 Å range (the same range as CCD 1). Line identification was straightforward as there was a good spread of $\sim$ ten strong emission lines across the entire wavelength range, as shown in Figure B.4 in Appendix B. From the solution, a dispersion of $\sim$ 0.38 Å pixel^{-1} could be deduced. The dispersion fit was interactively adjusted for each aperture of that first arc, and badly fit lines were deleted where necessary resulting in a good fit with an average Root Mean Squared (RMS) value of $\sim$ 0.011 Å. This dispersion solution was then applied to the other arc spectra using the `idhenear.dat` coordinate list in IRAF for general helium, neon and argon line identification. These solutions were fit using spline3 functions of order 3.

Next, the task `specplot` was used to compare groups of spectra at a time. By examining the changing emission line profiles across the two groups of 25 consecutive apertures from Background Block 11, a rough positioning of the spectra on the two-dimensional spatial image could be deduced. Firstly, the dominant emission lines (attributed to the target) had the greatest intensity in the spectra that were positioned in the middle of each of the two groups, implying that the spectra should be placed side-by-side along each row. Secondly, it was deduced that the placement of spectra snaked back and forth, as this would place similar line profiles next to each other. Lastly, it was reasoned that the spectra would read from top to bottom and from left to right in a logical sense. These three rules served as a starting point for the spectral mapping which is discussed in more detail in Section 3.3.

After the object spectra were extracted from the target image, the sky spectra needed to be subtracted in order to remove trends and sky lines. `dohydra` was run on all the background images, similarly to the previous extractions but with a few parameters changed appropriately. The target and the sky images were trimmed to be the same dimensions and the task `imarith` was then used to subtract the sky spectra from the target spectra. This produced a fairly linear, yet still noisy, spectra for each of the apertures. The extracted and calibrated sky-subtracted spectra for a central target aperture is shown in Figure 3.4.

From this process, some very strong helium and forbidden oxygen lines in the spectrum of V445 Pup could be identified, as seen in Figure 3.4 which is the extracted spectrum of the central target aperture 38 in Object Block 11 (CCD 1) from the 4 January 2006 observations.

3.2.2 Calibration of the Full Data Set

The other CCDs were similarly calibrated using the appropriate comparison charts from the HeNeAr Spectral Atlas (Crosswhite 1975), which are shown in the upper panels of Figures B.1, B.2, B.3 and B.4 in Appendix B. For comparison, the lower panels in these figures show the extracted spectrum from an arc image (Frame 83 on 4 January 2006 in Table A.1)

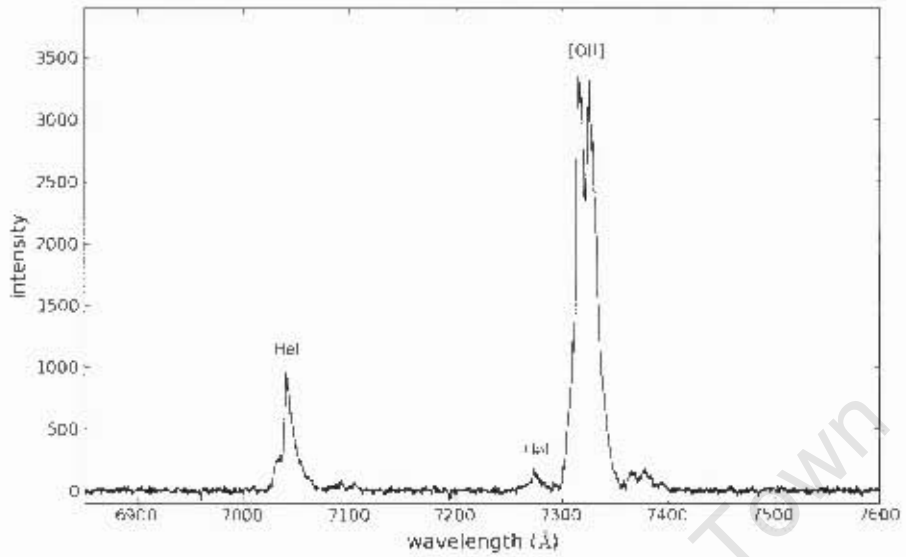

Figure 3.4: Extracted central target spectrum from aperture 38, Background Block 11 (CCD 1), after sky subtraction. The spectra is extracted from Frame 84 on the 4 January 2006 (see Table A.1). The [O II] λ7320/7330 doublet and the He I recombination line at 7065 Å are clearly identified.

that was used to create the dispersion solution for the other science images. Unfortunately, this identification technique means that the dispersion solution accuracy is dependent on the number of lines in the arc frame that can be identified from the spectral atlas. Therefore, in regions where few or no emission lines could be identified in the arcs, the solution increasingly worsened and became unreliable. Table 3.1 lists the wavelength range and the pixel scale with error for each CCD.

Both line charts for CCD 1 and CCD 2, seen in Figures B.4 and B.3 respectively, had $\sim$ 13 clear strong emission lines that were well spread across the wavelength range and easily identifiable in the arc spectrum. These identified lines provided a good dispersion solution with minimal error in the fit. On the other hand, the three identification lines in each of the charts corresponding to CCDs 3, 4, 7 and 8 (Figure B.2 and B.1 respectively) were not as well spread and therefore the σ_{fit} values (shown in Table 3.1) are unphysical. This is because `identify`, the task used to identify and compare lines, requires more lines in order to calculate a reasonable RMS value. Fortunately, both of the main emission lines in these regions; [O III] λ5007 in CCD 4 and He I λ5876 in CCD 3, fell within identifiable lines. Therefore, the fit is expected to be better in these regions which should allow for reliable analysis of these lines in future sections. Also, it is encouraging that the pixel scale is fairly constant at $\sim$ 0.38 Å pixel^{-1} across all of the CCDs.

Table 3.1: Table of pixel scale for each CCD

CCD	Wavelength Range (Å)	Number of Arc Lines Used	2006 Pixel Scale (Å/pixel)	2006 σ_{fit} [a] (Å)	2007 Pixel Scale (Å/pixel)	2007 σ_{fit} [a] (Å)
1	6850 to 7600	< 13	0.384	0.016	0.385	0.030
2	6000 to 6850	≤ 15	0.383	0.011	0.383	0.044
3 [b]	5250 to 6000	3	0.351	1.76E-10	0.369	1.42E-10
4 [b]	4500 to 5250	3	0.373	2.00E-12	0.375	2.25E-12
5	6000 to 6850	≤ 15	0.383	0.020	0.383	0.037
6	6850 to 7600	≤ 13	0.384	0.065	0.385	0.029
7 [b]	4500 to 5250	3	0.373	2.33E-10	0.375	2.46E-10
8 [b]	5250 to 6000	3	0.351	6.21E-10	0.369	7.94E-10

[a] σ_{fit} is the error to the fit, calculated by IRAF routines during the `identify` task
[b] As only three lines were fit in these CCDs, `identify` produced unrealistic σ_{fit} values

As the target was clearest on the 4 January 2006, spectra from this night were fully extracted and calibrated first. The resultant spectrum for all CCDs through the central fibres is presented in the results section of this dissertation (Chapter 4). The entire dataset from the third night, a year later, was also reduced and the spectra extracted, although the signal was weaker than in 2006.

3.2.3 Verification of the Wavelength Solution on IC 2165

In order to verify the dispersion solution, spectra from the planetary nebula IC 2165 were extracted and calibrated using the same reduction procedure that was used on the full data set of V445 Pup. The circular 8″-diameter nebula is ideal for verification purposes as it has published spectral lines and velocities that the observations can be compared with (Pottasch et al. 2004). The fully extracted, calibrated and sky-subtracted spectrum is shown in Figure 3.5.

By fitting a single Gaussian to each of the main observed emission lines, their respective wavelengths could be found. When compared to results found by Pottasch et al. (2004), all of the expected emission lines were identified, along with their respective intensities. The observed lines were converted into velocities using a standard Doppler shift conversion and the average radial velocity for the spectral lines of IC 2165 was found to be $v_r = 51.1 \pm 1.9\,\mathrm{km\,s^{-1}}$, as shown in Table 3.2. This agrees with the literature radial velocity for IC 2165 of 52.6 $\mathrm{km\,s^{-1}}$ retrieved from the SIMBAD database and calculated by Wilson (1953).

It is encouraging to see that the radial velocities derived for the bluest part of the spectra of IC2165 (CCDs 3 and 4) show no systematic offset from the mean (within the measured uncertainty), despite the earlier mentioned uncertainty in the wavelength calibration of these CCDs given the limited number of arc lines in this spectra range.

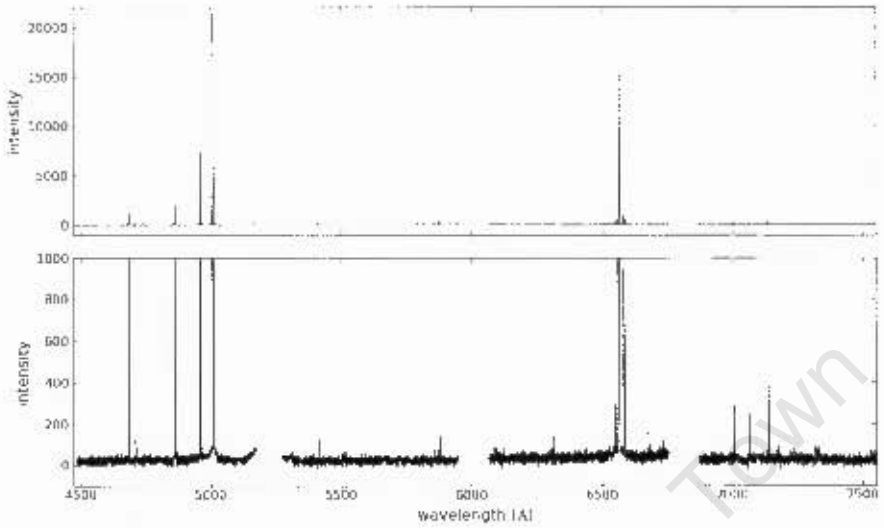

Figure 3.5: Upper Panel: fully extracted, calibrated and sky-subtracted spectrum of planetary nebula IC 2165, combining three 300s exposures from 4 January 2006. Lower panel: magnified view of the spectrum in the intensity range 1-1000.

Table 3.2: Table of observed emission lines and their respective velocities for IC 2165.

	$\lambda_{measured}$ (Å)		λ_{NIST} (Å)	Velocity[a] (km s^{-1})
CCD1	7331.28	[O II]	7330.19	44.6
	7321.07	[O II]	7319.99	44.3
	7137.1	[Ar III]	7135.79	55.1
	7007.07	[Ar V]	7005.67	59.9
CCD2	6731.98	[S II]	6730.82	51.7
	6584.28	[N II]	6583.45	37.8
	6564.03	H $_{\alpha}$	6562.82	55.3
	6313.02	[S III]	6312.06	45.6
CCD3	5876.66	He I	5875.61	53.4
CCD4	5007.78	[O III]	5006.84	56.1
	4862.17	H $_{\beta}$	4861.33	51.8
	4686.61	He II	4685.70	58.0
		Total Average (km s^{-1}):		51.1 ± 1.9

[a] All values are calculated with respect to their rest frame wavelength, λ_{NIST}, found in the NIST Atomic Spectral Database (Ralchenko et al. 2011).

3.3 Reconstructing the Data Cube

3.3.1 Fibre Allocation

Once the entire spectral set was extracted and calibrated, the spectra could be spatially mapped out according to their original fibre positioning. This created a 3D data cube with a 16 by 25 x/y axis and a z axis that spanned the entire wavelength range. The spectral placement was challenging as there was no documentation describing the positioning sequence for the observations and all of the CCDs had a few mis-identified apertures (due to blended or null apertures). Fortunately, standard star exposures were made for both years. As stars are expected to be point sources, their spectra need to be positioned such that the intensity is centred in a circular region on the CCD. The standard stars from each year were therefore ideal objects for testing fibre allocation once the basic layout had been deduced as mentioned in Section 3.2.1.

In Figure 3.6, a schematic is drawn up of the fibre allocation that best visualises the standard star mapping and consequently, the mapping of V445 Pup at both epochs. Each fibre is numbered and positioned, snaking back and forth as indicated in the figure with the pattern in one CCD mirrored in the other CCD on the other half of the image. This mapping was used to create the on-sky projections of the standard stars GD 50 (2006) and LTT2415 (2007) shown in the upper and lower panels, respectively, of Figure 3.7. Visually, both standard stars appear circular with a centralised intensity peak which is a promising indication that the mapping was successful. In order to quantify this result, intensity profiles across the horizontal and vertical axes of the star were plotted, with each profile consisting of nine summed pairs of fibres (as indicated in the figure). A Gaussian distribution was then fit to each profile to get an idea of the FWHM. In 2006, the FWHM of the horizontal axis was $0\farcs632 \pm 0\farcs029$ and $0\farcs628 \pm 0\farcs010$ across the vertical axis. In 2007, the respective axes values were slightly larger at $0\farcs655 \pm 0\farcs069$ and $0\farcs655 \pm 0\farcs011$. As these values indicate the stars are roughly circular, the mapping is therefore successful.

3.3.2 The Data Cubes of V445 Pup

With successful fibre allocations for both years, it was possible to create 3D pictures of the spectral emission from V445 Pup in the form of data cubes. Each of the spaxels in these data cubes are the combination of spectra from four CCDs to get the full wavelength range for each spaxel. In addition, each of these spaxels are also the combination of spectra from seven 30-minute exposures in 2006 and six 30-minute exposures in 2007.

Separate data cubes were created around prominent emission lines in order to compare the 3D emission of the nova for different elements. Unfortunately, spectra from CCD 3 and CCD 8 were poorly extracted as there were not enough emission lines to compare with arc

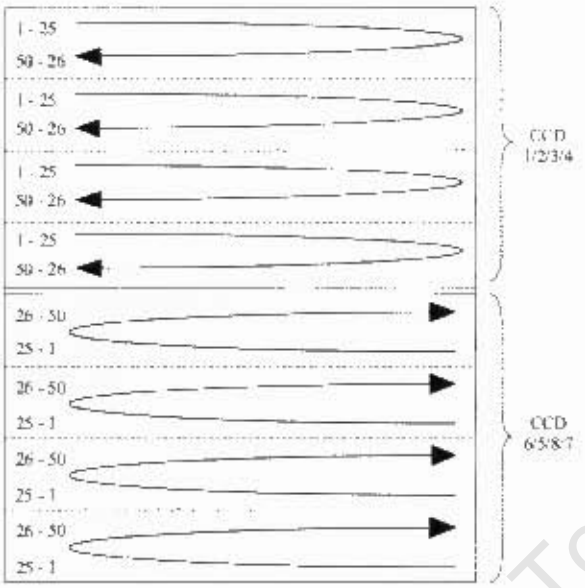

Figure 3.6: Schematic of the fibre allocation. Each image is the combination of spectra from two CCDs having the same wavelength range.

spectra and the three emission lines that were identified were centred to one side of the CCD (see Figure B.3). Therefore, although the prominent He I λ5876 emission line fell within this region, it can be assumed that any measurements are relatively unreliable. Also a bad column in CCD 8 fell over a large portion of the He I λ5876 line and distorted the line profile.

Since it is possible to highlight certain lines in data cubes, an in-depth study can be made into the velocity profiles of these lines. If light is traveling towards or away from the observer, the emission lines in the spectrum will respectively appear blue- or red- shifted, relative to the laboratory rest frame of the lines. Using the Doppler Shift equation, the amount of shift for an emission line (relative to its rest wavelength) can be used to calculate the radial velocity of the line. The Doppler Shift equation is:

$$v_r = \frac{\lambda_m - \lambda_o}{\lambda_o} \times c \tag{3.1}$$

where v_r is the radial velocity, λ_m is the measured wavelength, λ_o is the rest wavelength and c is the speed of light where $c = 2.9989 \times 10^8$ m s^{-2}.

A detailed analysis of V445 Pup in both wavelength and velocity space is made in Chapter 4. Data cubes of three prominent emission lines are compared and interesting features are interpreted.

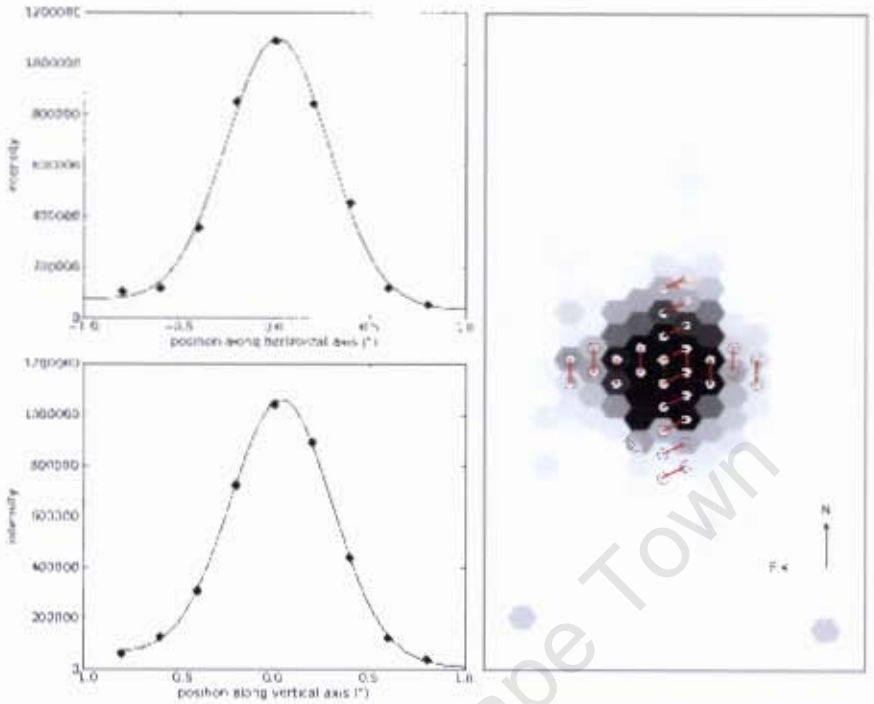

(a) 4 January 2006: Standard Star GD50

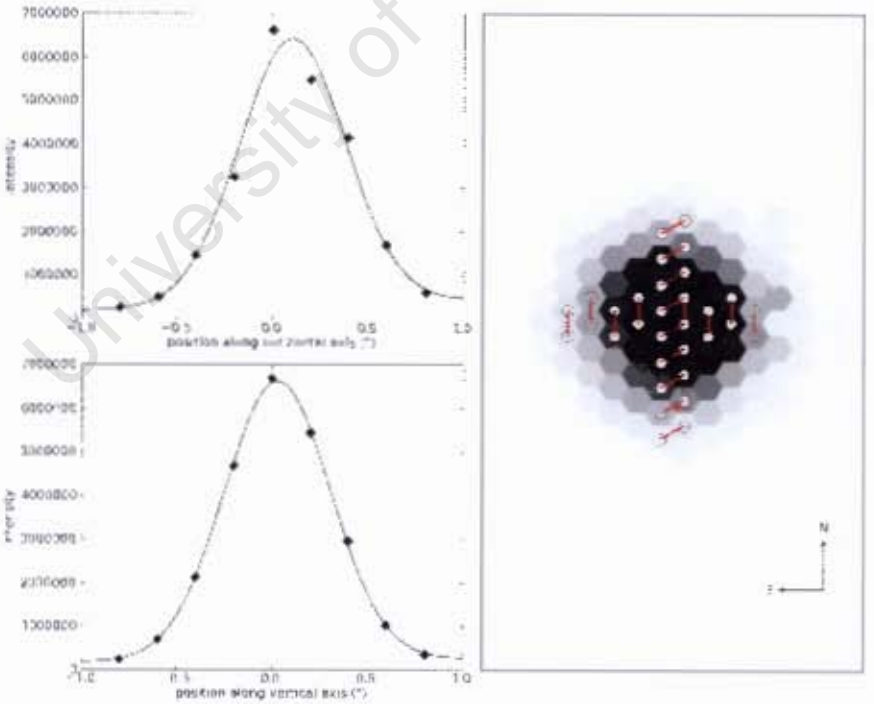

(b) 8 January 2007: Standard Star LTT2415

Figure 3.7: Right panels: Standard star on-sky projections of the summed emission from CCD 1 in 2006 and 2007 with intensity fits over summed fibre pairs across major and minor axes. Left panels: A Gaussian profile is fit to the intensity profile for each axis.

Chapter 4

Results

A combination of spectra from V445 Puppis, observed on 4 January 2006 and 8 January 2007, are analysed and assembled together to create a three dimensional picture of the changing nova shell. In this chapter, I analyse the summed spectra from the centre of the nova at the two epochs and identify prominent emission lines and discuss what they signify. I assemble a data cube of spectra for the three clearest emission lines: He I λ7065, [O III] λ5007 and the doublet [O II] λ7320/7330, and discuss and quantify interesting features, such as the apparent positional shift in peak intensity within the shell over a specific velocity range. Next I combine spectra from fibres in each of the lobes to identify and quantify their velocity structure. From position-velocity maps of each of the three lines, an unexpected excess of emission in the forbidden oxygen lines ([O II] λ7320/7330 and [O III] λ5007) is identified at both extremes of the shell. This excess is quantified and discussed.

Unless otherwise stated, all spectral analyses of V445 Pup in this Chapter, including all the figures shown, refer to the full data sets for 2006 and 2007, respectively. The data set in 2006 consists of seven 30-minute exposures (Frames 84-86, 88-89 and 93-94 in Table A.1), whereas the data set in 2007 consists of six 30-minute exposures (Frames 138, 141, 143-144 and 146-147 in Table A.3). The date of outburst, t_0, was chosen to be 1 November 2000.

4.1 Spectrum of V445 Puppis

Before I analyse individual features in the spectra, I present the 2006 spectrum of V445 Pup in Figure 4.1. The spectrum was created by summing the extracted spectra from the seven fibres positioned around the central region of the nova shell, with the positioning indicated in the left inset of the figure by star markers placed over an on-sky projection. The major axis of the nova shell is indicated in the right inset. Both insets display a map of the summed He I λ7065 intensity in the -900 km s^{-1} to -700 km s^{-1} range.

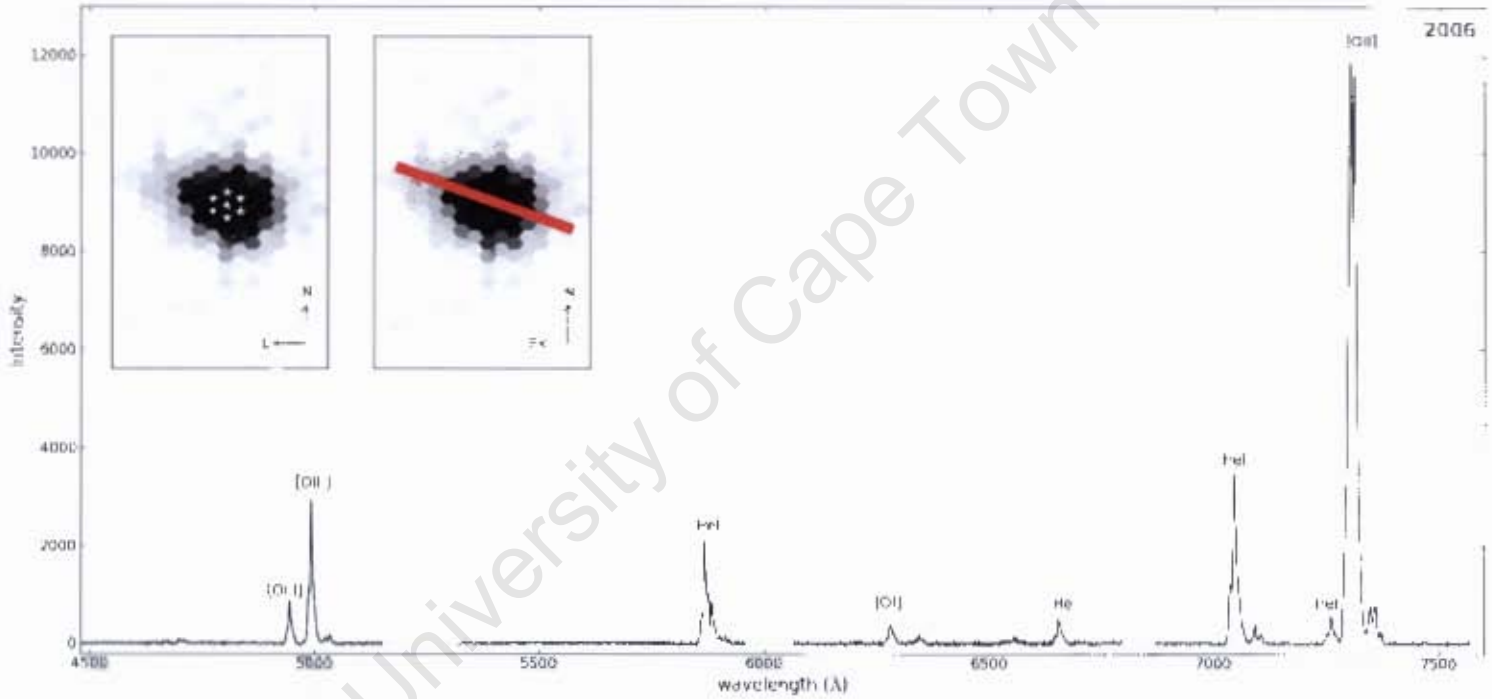

Figure 4.1: Central spectrum of V445 Puppis (2006). Inset, left: The markers indicate fibre positions. Inset, right: The major axis of the nova is indicated. Both insets are plotted over a spatial map of the combined intensity centred around the He I λ7065 emission of the nova in the region of -900 km s^{-1} to -700 km s^{-1}. The spectrum consists of four segments, each relating to the combination of two of the eight CCDs. Prominent emission lines are marked.

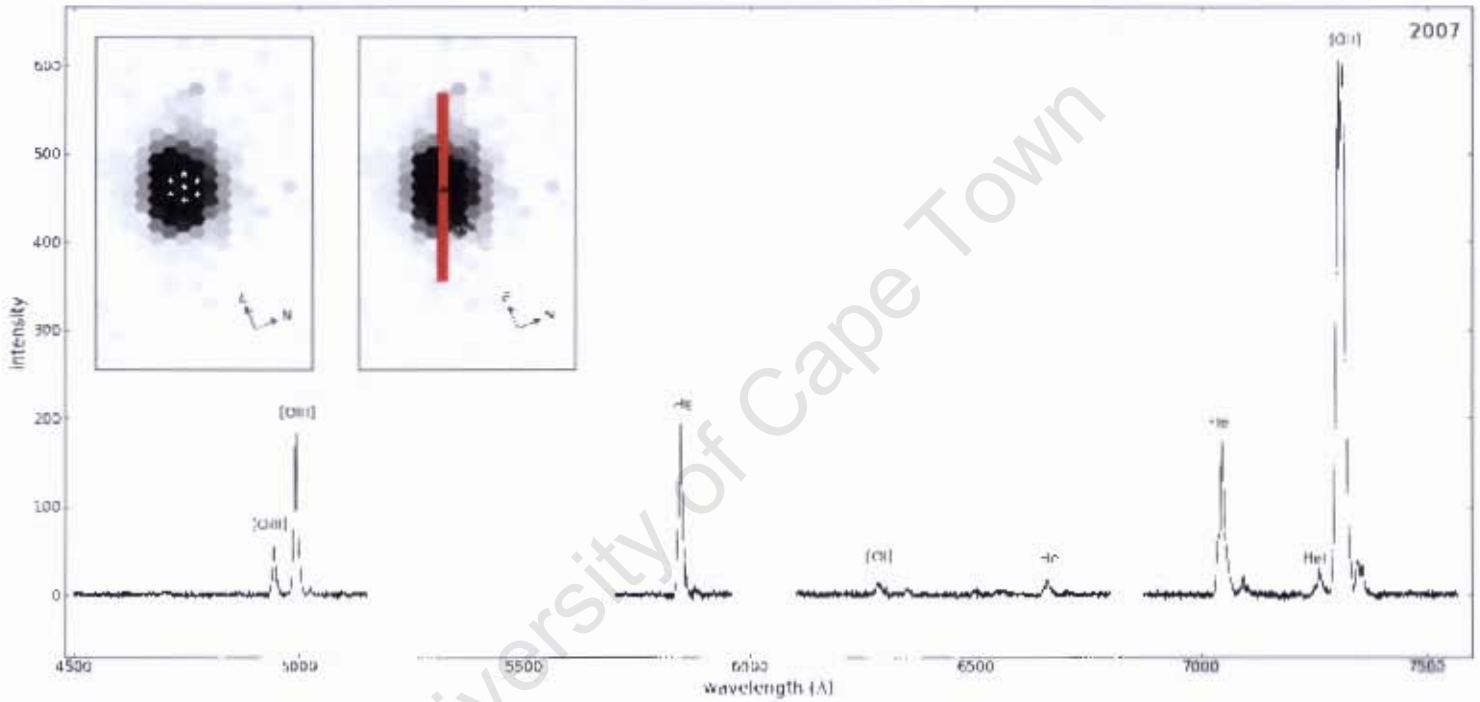

Figure 4.2: Central spectrum of V445 Puppis (2007). Inset, left: The markers indicate fibre positions. Inset, right: The major axis of the nova is indicated. Both insets are plotted over a spatial map of the combined intensity centred around the He I λ7065 emission of the nova in the region of -900 km s^{-1} to -700 km s^{-1}. The spectrum consists of four segments, each relating to the combination of two of the eight CCDs. Prominent emission lines are marked.

Table 4.1: Noise (Standard Deviation in the Mean) for each segment in the full spectra of V445 Puppis

CCD	2006 noise	2007 noise
1/6	16.9	1.96
2/5	19.4	1.82
3/8	16.3	1.68
4/7	14.0	1.45

Each of the four wavelength segments in both Figures 4.1 and 4.2 represent the sum of spectra extracted from two of the eight CCDs. A slight difference in noise level between the segments is observable, with CCD 2 and CCD 5 (both between 6000 Å and 6850 Å) being the noisiest in 2006. This is quantified in Table 4.1, where the noise levels (standard deviation in the mean) are calculated from small 50 Å wavelength regions containing no lines within each segment. Table 4.1 also shows a factor of ten decrease in overall intensity from 2006 to 2007. This is likely due to a different gain setting in 2007 and a decrease in system brightness from 2006 to 2007.

The prominent emission lines are identified in Figure 4.1 and presented in Table 4.2. As expected for this object, no hydrogen is observed, and emission lines of He I, [O I], [O II] and [O III] are clearly identified. Along with the lack of continuum emission, these lines suggest that the nova is in the nebular phase of its spectral transitions during post-outburst decline, reminiscent of a planetary nebula spectrum. This is also clear from the presence of forbidden lines which indicate that the nova consists of a low density gas (similar to what is seen in planetary nebulae). The lack of absorption lines suggests that the absorbing gas has dissipated and that wind and radiation from the white dwarf is causing increased ionisation (Williams et al. 2008). The presence of [O I] λ6300 either indicates that a neutral outer envelope (due to inner ionising photons) is causing the ionised gas to be ionisation-bound, or that there are higher density 'blobs' in the ejecta (Williams 1994). The forbidden ionised emission lines of [O II] and [O III] most likely originated in lower density regions in the shell. According to Lynch et al. (2004), the He I recombination lines probably appeared once the white dwarf unveiled a sufficiently hard photosphere sometime between October 2001 and January 2004. The He I lines are thought to originate from the hot interior region of the nova as viewed through the dust shell, thus giving rise to their observed velocity structure which matches that of the shell.

In Table 4.2, a single Gaussian was fit to each of the emission lines in order to get the peak intensity of the line and the wavelength at that peak intensity. Also in this table, the peak intensity for each line has been normalised to the peak intensity of He I λ7065. From these normalised intensities, it can be seen that the doublet [O II] λ7320/7330 has the strongest emission of all the lines. The ratio of [O III] λ5007 to [O III] λ4958 is $\sim 3.6 \pm 0.2$.

Table 4.2: Intensity and radial velocity of the highest peaked emission of V445 Puppis lines identified in 2006

2006	λ_{NIST} (Å)	$\lambda_{measured}$ (Å)	Velocity ($km\,s^{-1}$)	Peak Intensity$_{norm}$ [b]
[O III]	4958.31	4945.07 ± 0.42	−801 ± 25	0.210 ± 0.012
[O III]	5006.84	4992.75 ± 0.37	−844 ± 22	0.909 ± 0.046
He I [a]	5875.62	5866.60 ± 0.55	−461 ± 28	0.518 ± 0.027
[O I]	6300.30	6283.73 ± 0.51	−789 ± 24	0.098 ± 0.005
[O I]	6363.78	6346.50 ± 0.69	−814 ± 32	0.037 ± 0.003
He I	6678.15	6659.84 ± 0.50	822 ± 23	0.122 ± 0.006
He I	7065.19	7045.04 ± 0.38	−855 ± 16	1.000 ± 0.037
He I	7281.35	7260.75 ± 0.55	−848 ± 23	0.125 ± 0.007
[O II]	7319.92	7300.34 ± 0.39	−802 ± 16	3.518 ± 0.122
[O II]	7330.19	7308.12 ± 0.39	−903 ± 16	3.244 ± 0.101

[a] Since He I λ5876 was positioned on CCD 3 and CCD 8, it was poorly extracted and thus any measurements for this line are unreliable.
[b] Intensities are normalised with respect to the He I λ7065 peak intensity.

This approximately agrees with the expected 3:1 ratio deduced by Storey & Zeippen (2000).

All of the emission lines exhibit two clear components separated in radial velocity by $\sim 2360\,km\,s^{-1}$: a strong blue-shifted component and a much weaker red-shifted component. The blue-shifted components are the result of the material in the nova shell moving towards the observer. Conversely, the red-shifted components are due to the material seen moving away from the observer, just visible through an optically thick shell. In the spectrum, each of these blue and red components can be further broken down into two parts separated in radial velocity by $\sim 450\,km\,s^{-1}$. This is evidence that the lobe axis is slightly inclined away from the plane of the sky, with one lobe more inclined towards the observer. This is not so obvious in Figure 4.1 as only central region apertures are taken into account. A more in-depth study of the difference between the lobes is made in Section 4.2.2.

The 2007 spectrum remains largely unchanged, as shown in the final nova spectrum in Figure 4.2. Similarly to Figure 4.1, the spectrum is the result of seven summed fibres from the central region, the positions demarcated by stars in the inset of the figure. In 2007, the overall counts are lower than in the 2006 data. This is in part due to a decrease in brightness from 2006 to 2007 ($V = 18.95$ mag in 2006 vs. $V = 19.74$ mag in 2007, D. Steeghs, private communication), which results in a factor of 2 intensity decrease. Also, the change of gain setting of the IMACS/IFU spectrograph from 0.9 in 2006 to 1.2 in 2007 will contribute to the decrease in intensity. Despite the lower intensity in 2007, most of the same emission lines (along with their respective components) can be observed. Prominent emission lines in the 2007 spectra are presented in Table 4.3.

In a comparison of Table 4.2 with Table 4.3, only He I λ5876 shows a significant difference

Table 4.3: Intensity and radial velocity of the highest peaked emission of V445 Puppis lines identified in 2007

2007	λ_{NIST} (Å)	$\lambda_{measured}$ (Å)	Velocity ($km\,s^{-1}$)	Peak $Intensity_{norm}$ [b]
[O III]	4958.31	4944.27 ± 0.40	−849 ± 24	0.290 ± 0.013
[O III]	5006.84	4992.17 ± 0.40	−879 ± 24	0.960 ± 0.043
He I[a]	5875.62	5845.38 ± 0.39	−1543 ± 20	0.940 ± 0.037
[O I]	6300.30	6284.29 ± 0.79	−762 ± 38	0.070 ± 0.005
[O I]	6363.78	6346.67 ± 0.66	−806 ± 31	0.040 ± 0.003
He I	6678.15	6659.03 ± 0.56	−858 ± 25	0.090 ± 0.005
He I	7065.19	7046.19 ± 0.40	−807 ± 17	1.000 ± 0.044
He I	7281.35	7262.21 ± 0.42	−788 ± 17	0.150 ± 0.008
[O II]	7319.92	7302.83 ± 0.36	−700 ± 15	3.530 ± 0.113
[O II]	7330.19	7310.33 ± 0.37	−813 ± 15	3.580 ± 0.117

[a] Since He I λ5876 was positioned on CCD 3 and CCD 8, it was poorly extracted and thus any measurements for this line are unreliable.
[b] Intensities are normalised with respect to the He I λ7065 peak intensity.

in its normalised intensity from 2006 to 2007. Also, He I λ5876 has a largely different radial velocity from the other lines in both years. This is most likely due to the poor dispersion solution in CCDs 3 and 8 resulting from a lack of arc identification lines (See Appendix B.2). The ratio of [O III] λ5007 to [O III] λ4958 in 2007 is now $\sim 3.3 \pm 0.2$. This is in better agreement with the 3:1 ratio deduced by Storey & Zeippen (2000) than the 2006 ratio. The average velocity (without considering He I λ5876) is $-831 \pm 12\,km\,s^{-1}$ in 2006 and $-807 \pm 18\,km\,s^{-1}$ in 2007.

The blending of these various components with each other make identification of the specific wavelengths difficult. For further kinematic analysis of V445 Pup in both years, I chose to analyse the most dominant lines; namely He I λ7065, [O III] λ5007 and the doublet [O II] λ7320/7330. Although He I λ5876 is also a very strong line, it was not analysed as a bad column in CCD 8 fell directly over it and the line falls within the CCD 3 and 8 segment (which has poorly fit dispersion solutions due to limited arc identification lines, see Appendix B.2). The He I λ7065 emission line provides the clearest view of the velocity structure of the nebula for the two epochs.

4.2 Intensity Profiles of V445 Puppis

4.2.1 General Appearance of V445 Puppis

The extracted spectra of V445 Pup can be arranged to create a data cube with two spatial axes and a velocity axis, which can then be used to obtain a three-dimensional picture of the nova shell for various emission lines. This is shown for 2006 and 2007 in the He I λ7065

on-sky projections in Figures 4.3 and 4.4, in the [O II] λ7320/7330 on-sky projections in Figures 4.5 and 4.6 and in the [O III] λ5007 on-sky projections in Figures 4.7 and 4.8.

In all the projections, the data cube is presented in 20 snapshots across the velocity range of the respective emission line with each snapshot a combination of summed intensity maps in 200 km s^{-1} intervals. The snapshots cover the range -1700 km s^{-1} to $+2300$ km s^{-1}; where panel A covers -1700 km s^{-1} to -1500 km s^{-1}, panel B covers -1500 km s^{-1} to -1300 km s^{-1}, etc. The mean radial velocity of V445 Puppis is covered in panel K (224 $\pm$ 0.8 km s^{-1} (Iijima & Nakanishi 2008)).

In all of the figures, the blue-shifted and red-shifted components can be distinguished. The blue-shifted component is mostly seen in panels A to J (corresponding to a displacement of 2000 km s^{-1}) and the red-shifted component is mostly visible in panels M to T (corresponding to a displacement of 1600 km s^{-1}). As the intensity of the red-shifted components is far smaller than that of the blue-shifted components, panels M to T are presented with a lower intensity range in order to be able to make out the emission features. In all figures, the intensity peaks in panel E (-900 km s^{-1} to -700 km s^{-1}).

Each of the panels in Figures 4.3 and 4.4 consist of fibres from CCD 1 (left eight columns) and CCD 6 (right eight columns). There is only a marginal difference in the noise level between the two CCDs; the average σ for background regions consisting of seven fibres across the entire wavelength range is 12.27 in CCD 1 and 16.40 in CCD 6.

In Figure 4.3, the nova reaches a peak intensity in panel E and has a major axis that is slightly inclined to the horizontal axis. In this panel, the intensity peaks in the centre of the nova and gradually decays outward along the major axis. As V445 Pup is known to have a bipolar shell, this appearance is the result of a seeing-limited projection of the nova and its lobes. For further analysis, I will refer to the the two respective lobes as North-East (NE) and South-West (SW), relative to the North-East configuration marker in panel T. Although V445 Pup exhibited a pinched waist in Figure 1.4 (Woudt et al. 2009), it cannot be seen in the figures as a result of seeing-limited observations (as opposed to the adaptive optics data shown in Figure 1.4).

The on-sky projections from 2006 (Figure 4.3) and 2007 (Figure 4.4) do not differ greatly from each other. The extent of emission from the red-shifted and blue-shifted components and the ratio between them remains the same in 2006 and 2007. In both Figures 4.3 and 4.4, the peak intensity appears to move from the NE lobe to the SW lobe as you step through the panels for each of the shifted components, e.g. the peak intensity appears to shift from the NE lobe in panel B to the SW lobe in panel H, back to the NE lobe in panel M and finally to the SW lobe in panel R. This feature arises from the fact that the lobe axis is at an inclination to the plane of the sky. As the material in the NE lobe is moving faster

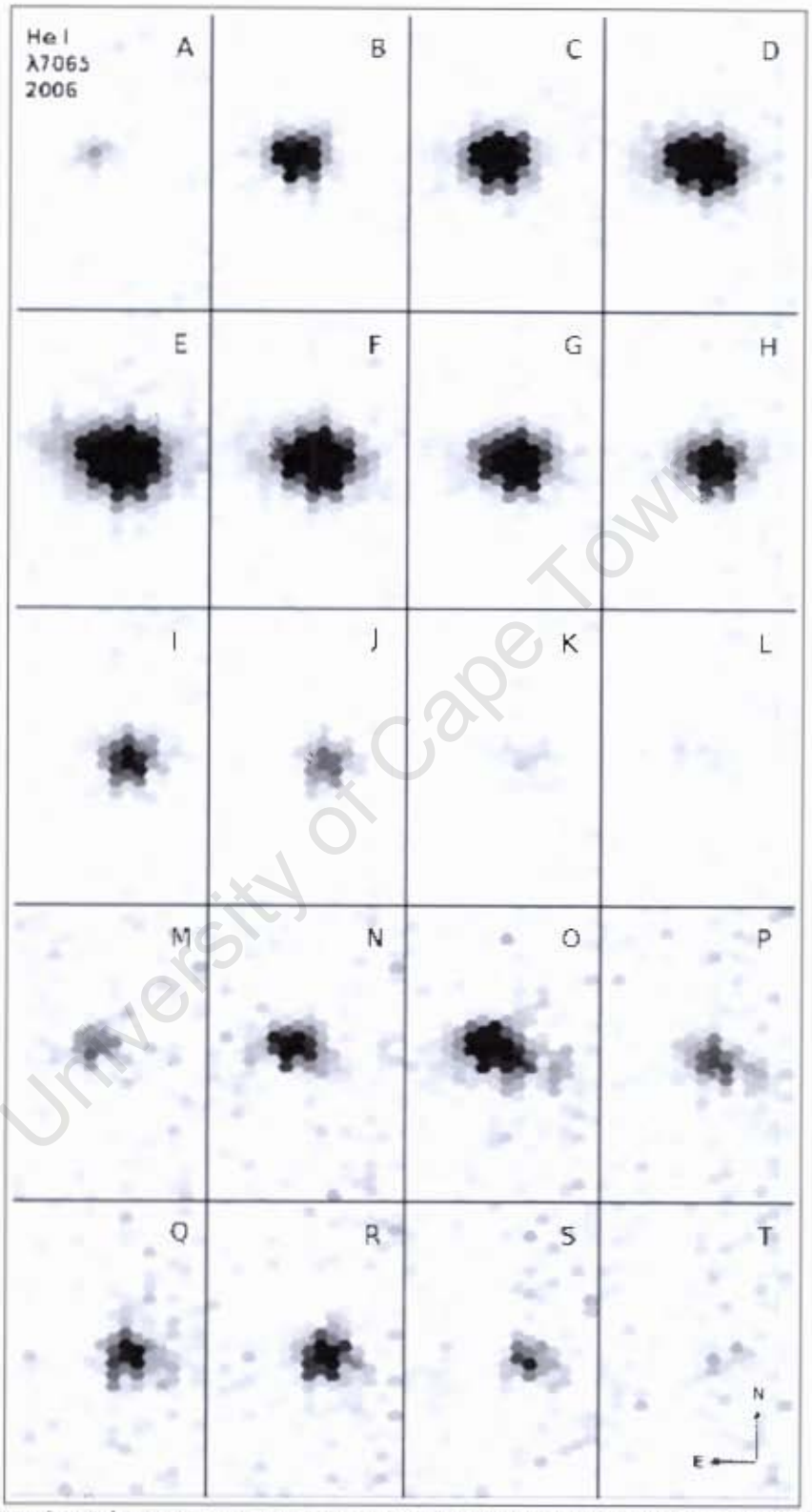

Figure 4.3: Spatial intensity maps of the summed spectra around the He I λ7065 emission line from − 1700 km s $^{-1}$ to + 2300 km s^{-1} from panels A to T, in steps of 200 km s $^{-1}$ observed on 1 January 2006. Panels A to L have an intensity range of 1-1900 and M to T have an intensity range of 1 500. Each of the 400 apertures have a 0.2″ diameter. The North East configuration is indicated in panel T and applies to all panels.

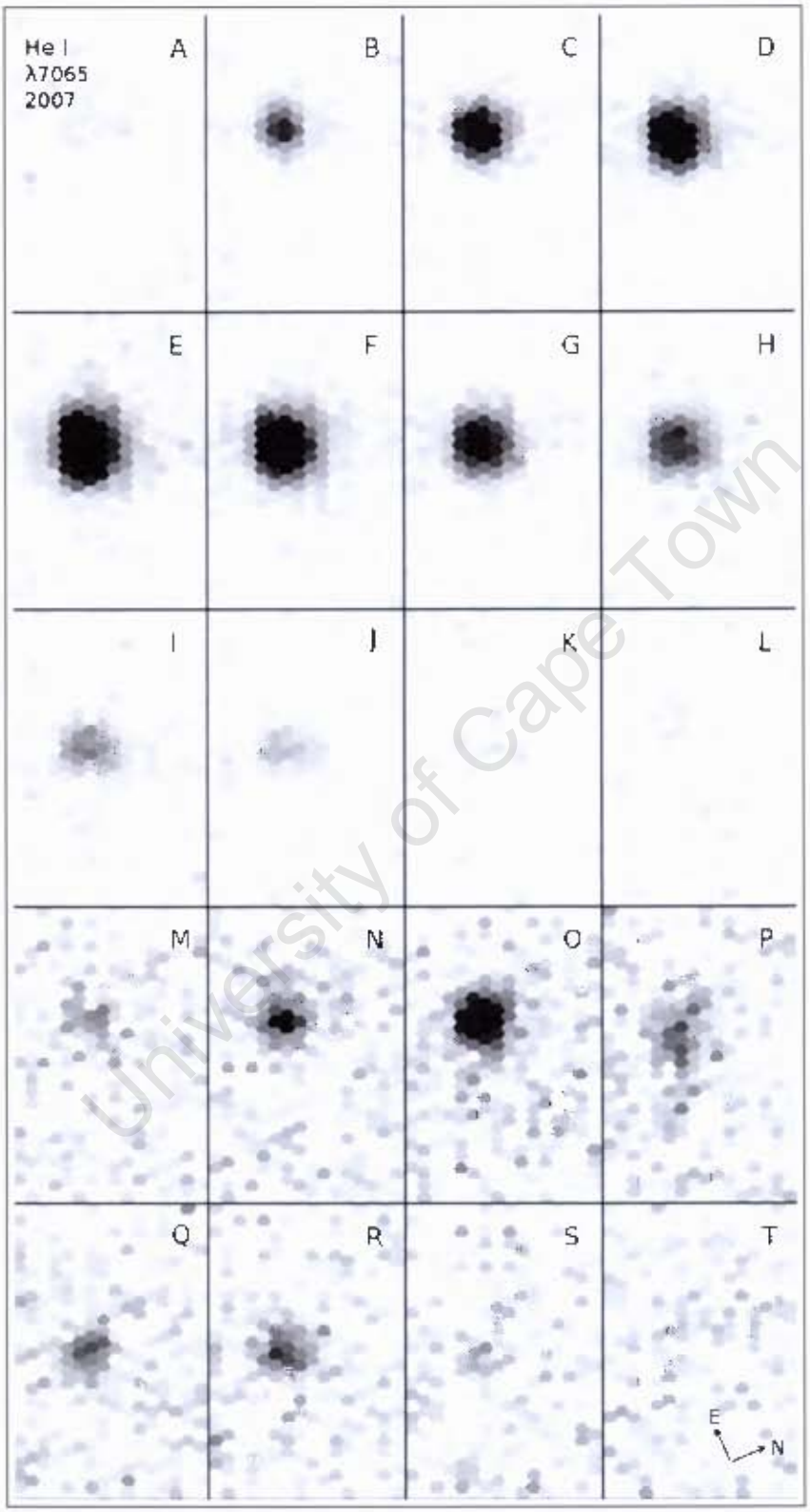

Figure 4.4: Spatial intensity maps of the summed spectra around the He I λ7065 emission line from $-1700\,\mathrm{km\,s^{-1}}$ to $+2300\,\mathrm{km\,s^{-1}}$ from panels A to T, in steps of $200\,\mathrm{km\,s^{-1}}$ observed on 8 January 2007. Panels A to L have an intensity range of 1-600 and M to T have an intensity range of 1-300. Each of the 400 apertures have a 0.2″ diameter. The North-East configuration is indicated in panel T and applies to all panels.

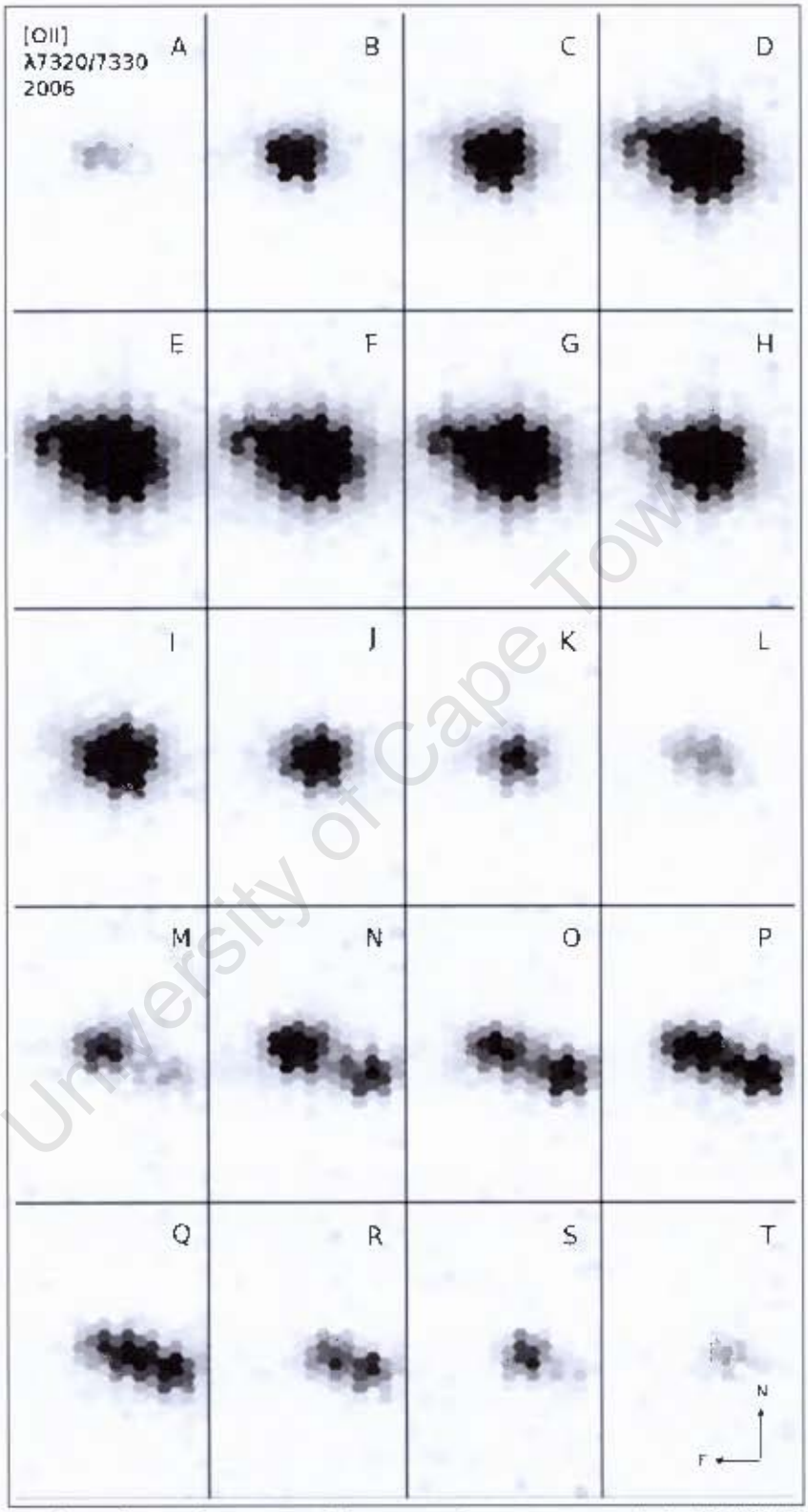

Figure 4.5: Spatial intensity maps of the summed spectra around the [O II] λ7320/7330 doublet emission line from −1700 km s^{-1} to +2300 km s^{-1} from panels A to T, in steps of 200 km s^{-1} observed on 4 January 2006. Panels A to L have an intensity range of 1-2000 and (M) to (T) have an intensity range of 1-1000. Each of the 400 apertures have a 0.2″ diameter. The North-East configuration is indicated in panel T and applies to all panels.

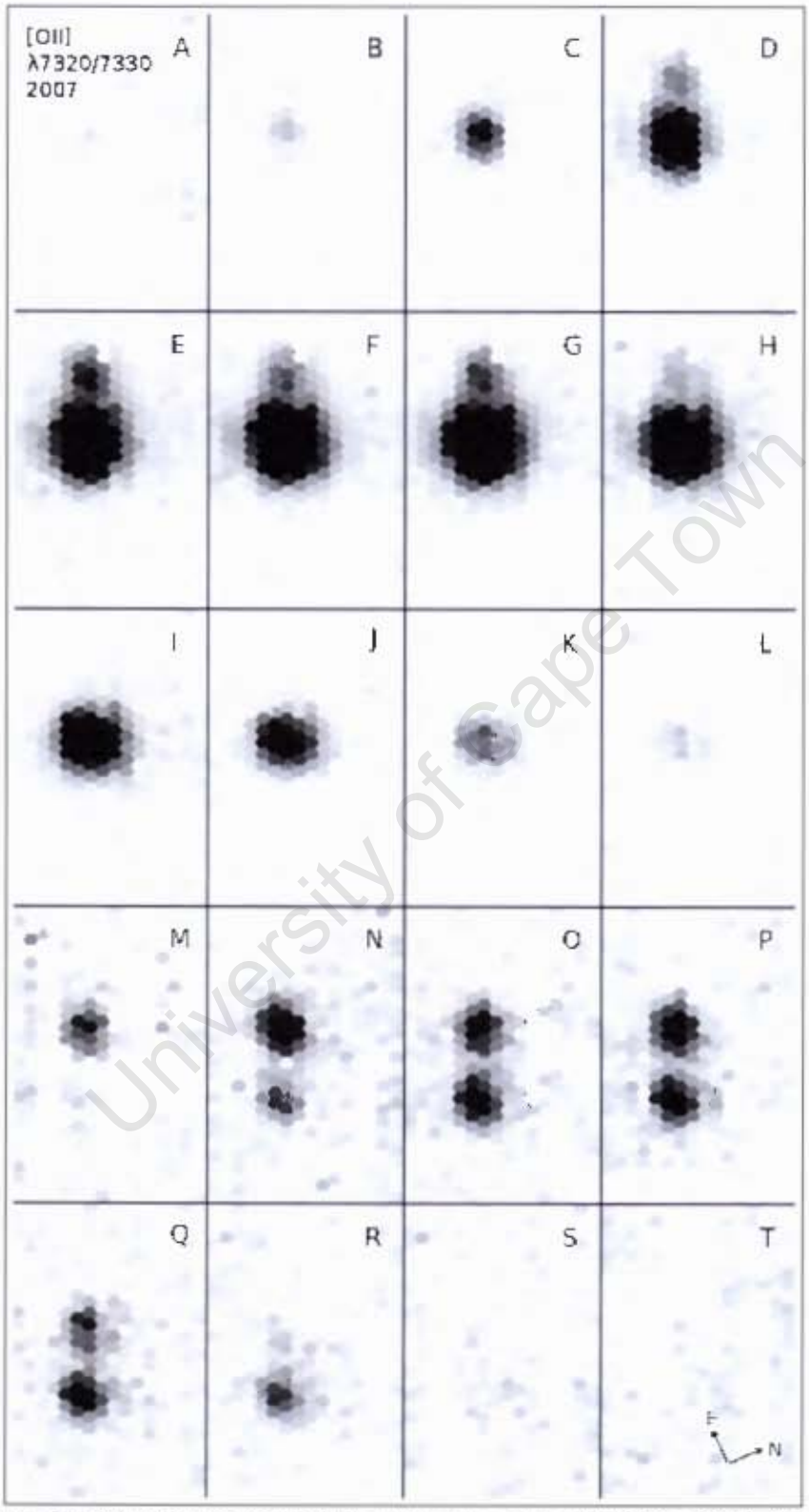

Figure 4.6: Spatial intensity maps of the summed spectra around the [O II] λ7320/7330 doublet emission line from -1700 km s^{-1} to $+2300$ km s^{-1} from panels A to T, in steps of 200 km s^{-1} observed on 8 January 2007. Panels A to L have an intensity range of 1-900 and M to T have an intensity range of 1-400. Each of the 400 apertures have a 0.2″ diameter. The North-East configuration is indicated in panel T and applies to all panels.

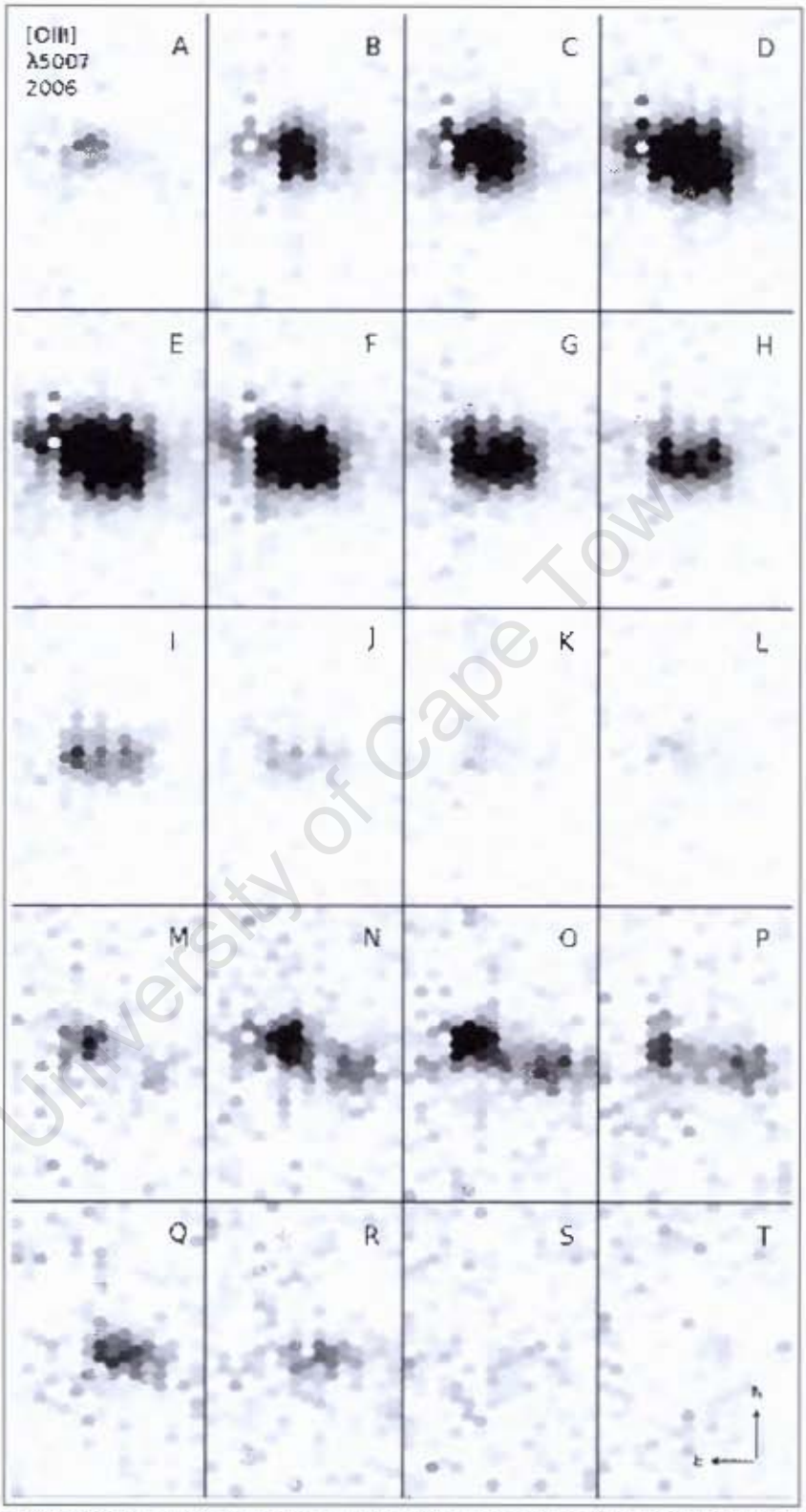

Figure 4.7: Spatial intensity maps of the summed spectra around the [O III] λ5007 emission line from $-1700\,\mathrm{km\,s^{-1}}$ to $+2300\,\mathrm{km\,s^{-1}}$ from panels A to T, in steps of $200\,\mathrm{km\,s^{-1}}$ observed on 4 January 2006. Panels A to L have an intensity range of 1-700 and M to T have an intensity range of 1-350. Each of the 400 apertures have a 0.2″ diameter. The North-East configuration is indicated in panel T and applies to all panels.

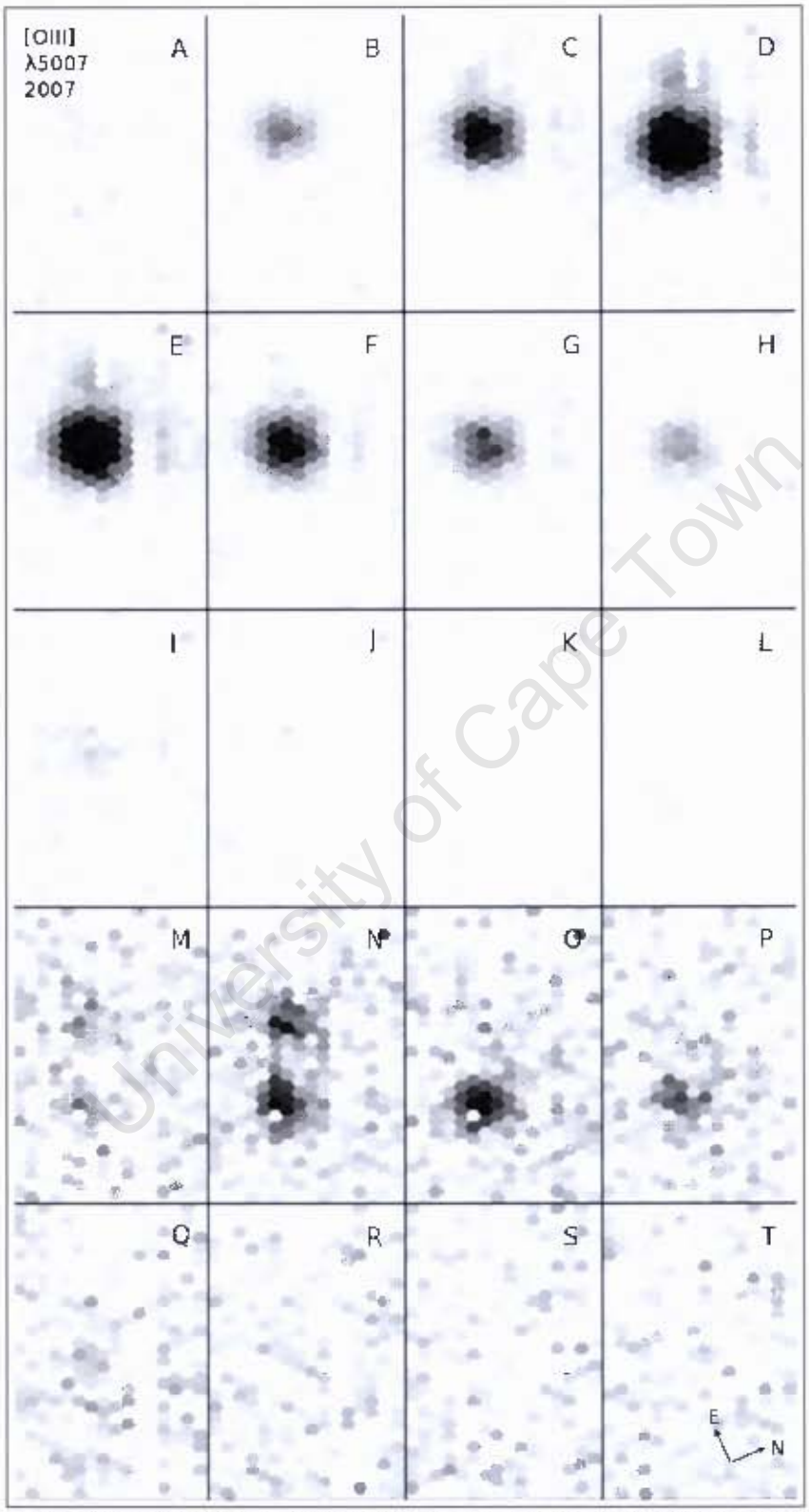

Figure 4.8: Spatial intensity maps of the summed spectra around the [O III] λ5007 emission line from −1760 km s^{-1} to +2300 km s^{-1} from panels A to T, in steps of 200 km s^{-1} observed on 8 January 2007. Panels A to L have an intensity range of 1-600 and M to T have an intensity range of 1-150. Each of the 400 apertures have a 0.2″ diameter. The North-East configuration is indicated in panel T and applies to all panels.

towards us than the SW lobe material, we can deduce that the NE lobe is inclined slightly towards us with respect to the plane of the sky. This feature is studied further in Section 4.2.2.

The on-sky projections of [O II] λ7320/7330 in 2006 and 2007 are presented in Figures 4.5 and 4.6 respectively. The general appearance of the nova emission in these figures remains the same as in the projections of He I λ7065 (Figures 4.3 and 4.4). Also, the same shift in intensity of the blue- and red-shifted components can be seen.

There is an interesting difference between the on-sky projections of He I λ7063 and [O II] λ7320/7330 that manifests itself in panels D through H and then again in panels M through R. In the [O II] λ7320/7330 emission of Figure 4.5, there appears to be an excess of emission in both the NE region and more clearly in the SW region of the nova at distinctly different locations than the bipolar shell. This feature is not apparent in the He I λ7065 emission (Figure 4.3). As each of the apertures is sampled at 0.″2, the excess regions appear $\sim$1.″0 away from the centre of the nova in 2006. In a comparison of the [O II] λ7320/7330 emission from 2006 (Figure 4.5) and 2007 (Figure 4.6), they are mostly similar in appearance except for the excess regions which appear to be expanding linearly outwards from 2006 to 2007. According to results presented by Woudt et al. (2009), these emission peaks could possibly relate to the NE and SW knots of the nova. A more detailed analysis of these regions is presented in Section 4.3.2.

In Figures 4.7 and 4.8, on-sky projections of [O III] λ5007 emission in 2006 and 2007 are visualised. The spatial maps centred around the [O III] λ5007 emission are clear with a few blank fibres in a bad column due to blended apertures. In these two figures, the general appearance resembles the on-sky projections of He I λ7065 except for an excess of oxygen. As seen in Figure 4.5, the excess region features in panels M to P of this figure, but with a weaker intensity than the excess in [O II] λ7320/7330. In 2006, the SW excess emission of [O III] λ5007 (Figure 4.7) has a weaker intensity than the SW lobe. On the other hand, in 2007 (Figure 4.8) the same SW excess emission is now brighter than the SW lobe. This can be seen when comparing panels N, O and P from both years. This does not feature in the [O II] λ7320/7330 emission over the two years. Possible explanations are discussed in Section 5.1.

4.2.2 Shift of Intensity Peak Across Major Axis

The on-sky projections of Figure 4.3 and Figure 4.5 reveal a shift in peak intensity from the NE lobe to the SW lobe relative to the blue- or red-shifted components of the He I λ7065 emission line or the [O II] λ7320/7330 doublet. It was remarked in the previous section that this is the result of an inclination of the polar outflow axis, such that the central axis of the NE lobe is closer to the observers line-of-sight than the SW lobe. In Figure 4.9, this result is quantified.

For 18 of the 20 on-sky projections shown in Figure 4.3 (panels B to S), an intensity profile was constructed along the major axis. A Gaussian was fit to the intensity profile (in each velocity interval) which gave a peak intensity and position along the major axis (relative to the centre of the nova where the peak occurred). The positions of the summed fibres along the major axis (over a He I λ7065 on-sky projection in the interval $-900\,\mathrm{km\,s^{-1}}$ to $-700\,\mathrm{km\,s^{-1}}$) are indicated in the upper right panel of Figure 4.9. The shift in peak intensity of the He I λ7065 emission line from the nova centre is quantified with uncertainties in the upper left panel. This process was repeated for the [O II] λ7320/7330 doublet line in 2006 and then again for both lines in 2007 (Figure 4.10).

In the left panel of Figure 4.9a, the trend line can be broken up into three sections: The first section runs from $-1400\,\mathrm{km\,s^{-1}}$ to $+200\,\mathrm{km\,s^{-1}}$ which corresponds to the blue-shifted component of the He I λ7065 line (panels B to J in Figure 4.3). The second runs from $+800\,\mathrm{km\,s^{-1}}$ to $-1800\,\mathrm{km\,s^{-1}}$ and corresponds the red-shifted component of the line (panels N to T in Figure 4.3). In the third section, at $-400\,\mathrm{km\,s^{-1}}$ and $-600\,\mathrm{km\,s^{-1}}$, there is no signal from either shifted line component and therefore the uncertainty is high. These three sections can be seen clearly at the same velocity intervals in Figure 4.9b and a year later in Figure 4.10.

The trends for both lines in Figures 4.9 and 4.10 appear to approximately follow the same pattern. In each of the sections relating to specific line components, the peak intensity shifts by about 0$''$.5 from East to West. A year later in 2007, a shift of $\sim$ 0$''$.5 can still be identified. This quantity is reasonable as it falls within the nova ejecta span of 2$''$ - 3$''$ observed by Woudt et al. (2009).

When analysing the [O II] λ7320/7330 doublet line in all of the figures, a second Gaussian has to be fit to the red-shifted component or to the blue-shifted component. Shown in Figures 4.9b and 4.10b, there are two extra trends between $+1000\,\mathrm{km\,s^{-1}}$ and $-1600\,\mathrm{km\,s^{-1}}$, relating to the SW excess region and between $-1000\,\mathrm{km\,s^{-1}}$ and $+200\,\mathrm{km\,s^{-1}}$, relating to the NE excess region. In 2006, the NE excess was not bright enough and too close to the NE shell to successfully distinguish between the components with Gaussian profiles. Therefore, in Figure 4.9, a red dashed line indicates the expected position of the excess from visual inspection. These trend cannot be seen in the He I λ7065 figures from either year. Interestingly, the trend appears to move outwards by $\sim$ 0$''$.2 from the centre of the nova shell from 2006 to 2007.

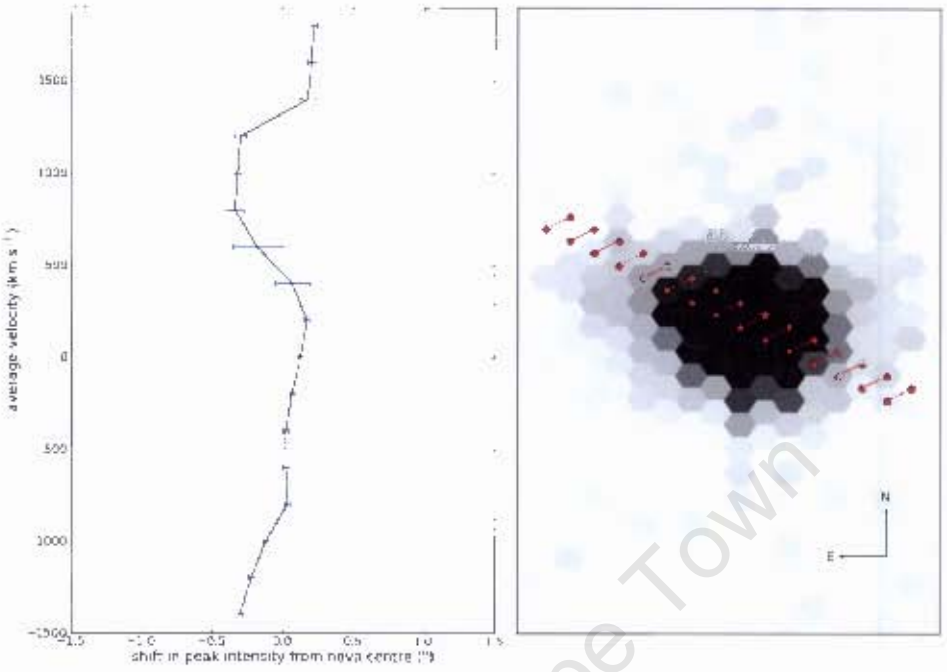

(a) He I λ7065

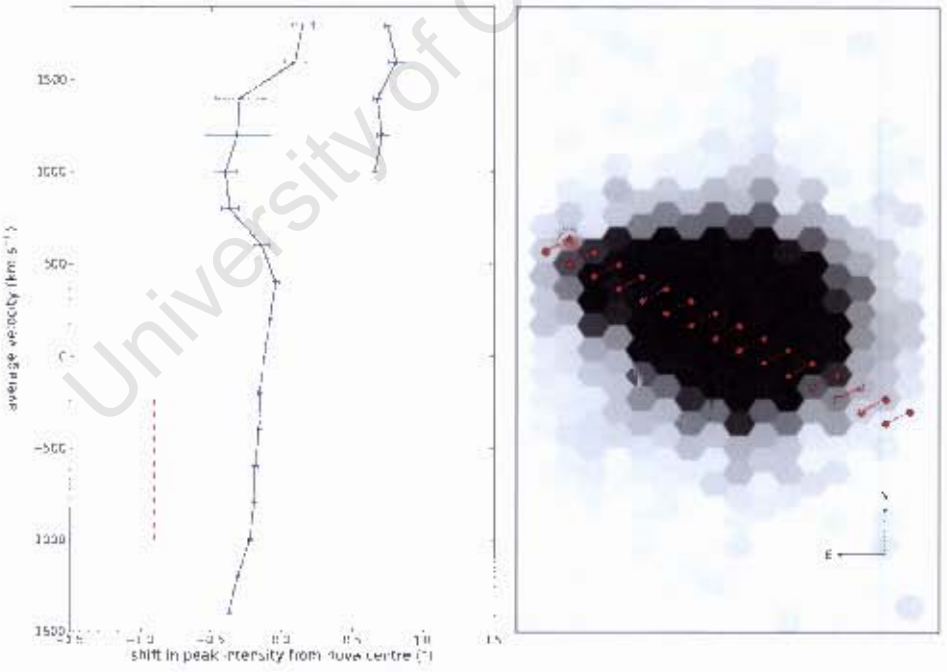

(b) [O II] λ7320/7330

Figure 4.9: Top panel (a), left: Shift in arcsec of the peak intensity of the He I λ7065 line from 4 January 2006, along the major axis of the shell relative to the centre of V445 Puppis (negative offset = North-East) across 18 velocity intervals. Top panel (a), right: The position of the major axis of the nova shell overplotted on the HeI 7065 summed intensity in the −900 to −700 km/s velocity interval. Lower panels (b): As above, but for the [O II] λ7320/7330 line. Dashed line indicates likely position of NE excess from visual inspection.

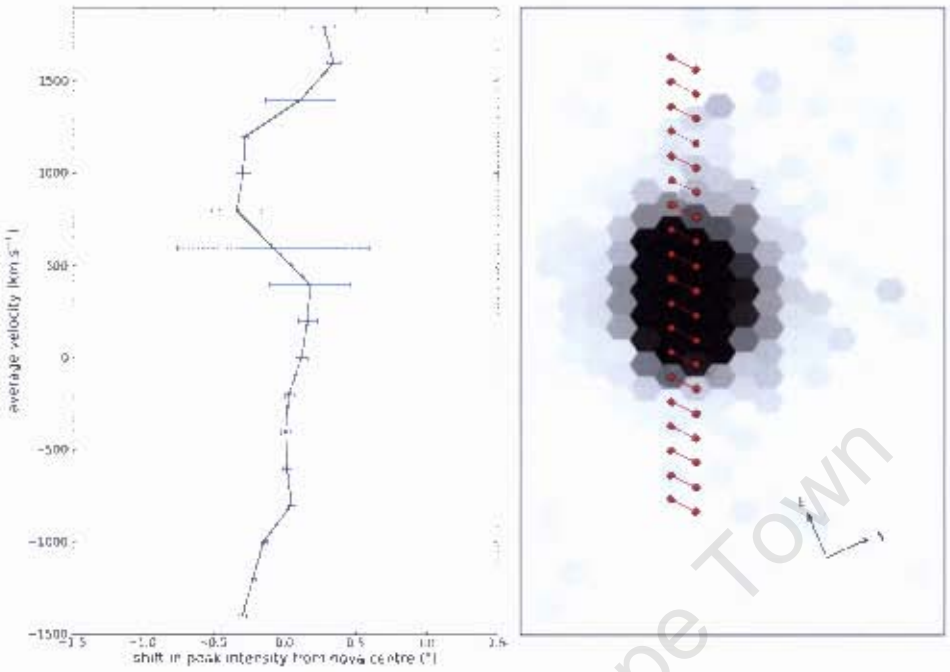

(a) He I λ7065

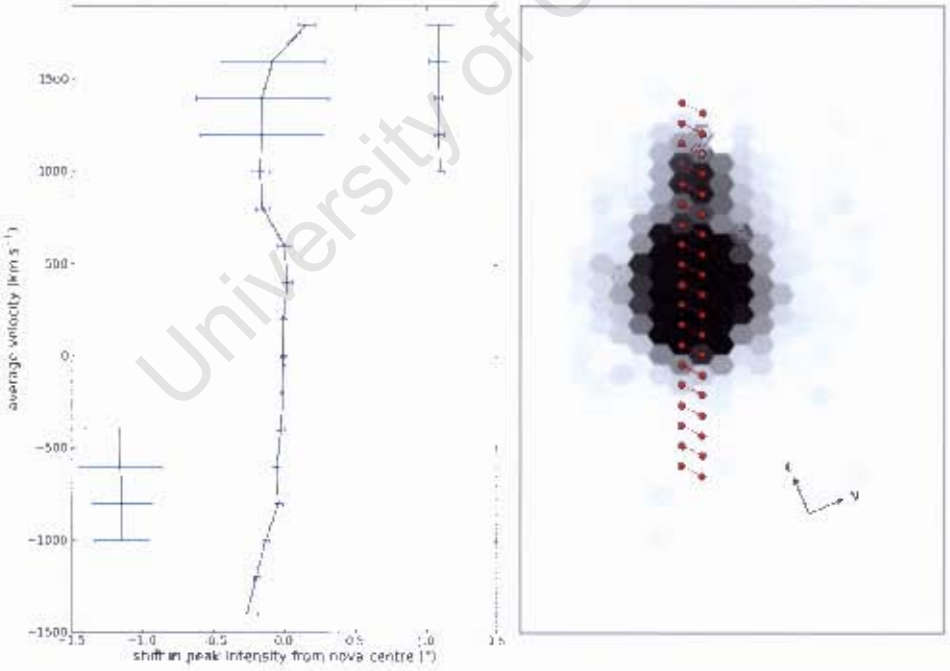

(b) [O II] λ7320/7330

Figure 4.10: Top panel (a), left: Shift in arcsec of the peak intensity of the He I λ7065 line from 8 January 2007, along the major axis of the shell relative to the centre of V445 Puppis (negative offset = North-East) across 18 velocity intervals. Top panel (a), right: The position of the major axis of the nova shell overplotted on the HeI 7065 summed intensity in the −900 to −700 km/s velocity interval. Lower panels (b): As above, but for the [O II] λ7320/7330 line.

4.3 Velocity Profiles of V445 Puppis

4.3.1 Position-Velocity Plots

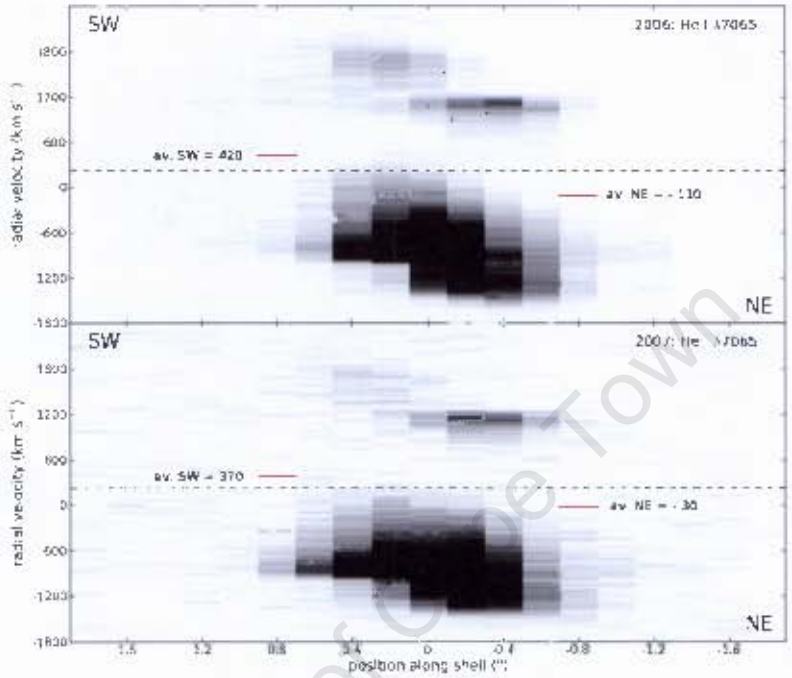

Figure 4.11: Spatially-resolved velocity profiles of emission line He I λ 7065 in 2006 (upper panel with intensity range 1-450) and in 2007 (lower panel with intensity range 1-150). In both images, spectra from summed pairs of fibres are plotted along the major axis of V445 Pup, running from West to East (left to right). Dashed lines indicate the systematic velocity ($224 - 8$ km s^{-1} (Iijima & Nakanishi 2008)) and the mean radial velocities for each lobe are indicated.

In order to analyse the spatio-kinematic properties of V445 Puppis, position-velocity (PV) maps are presented for each of the three prominent emission lines in 2006 and 2007. The PV plots of He I λ7065 from 2006 and 2007 are compared in Figure 4.11. In this figure, the velocity profiles of the He I lines from 15 summed pairs of fibres are plotted. The fibres are sampled at 0".2 across the major axis from East to West on the sky, as indicated in the right panels of Figures 4.9 and 4.10. A dashed line in the figures indicates the systematic velocity of V445 Pup at 224 ± 8 km s^{-1}, as reported by Iijima & Nakanishi (2008).

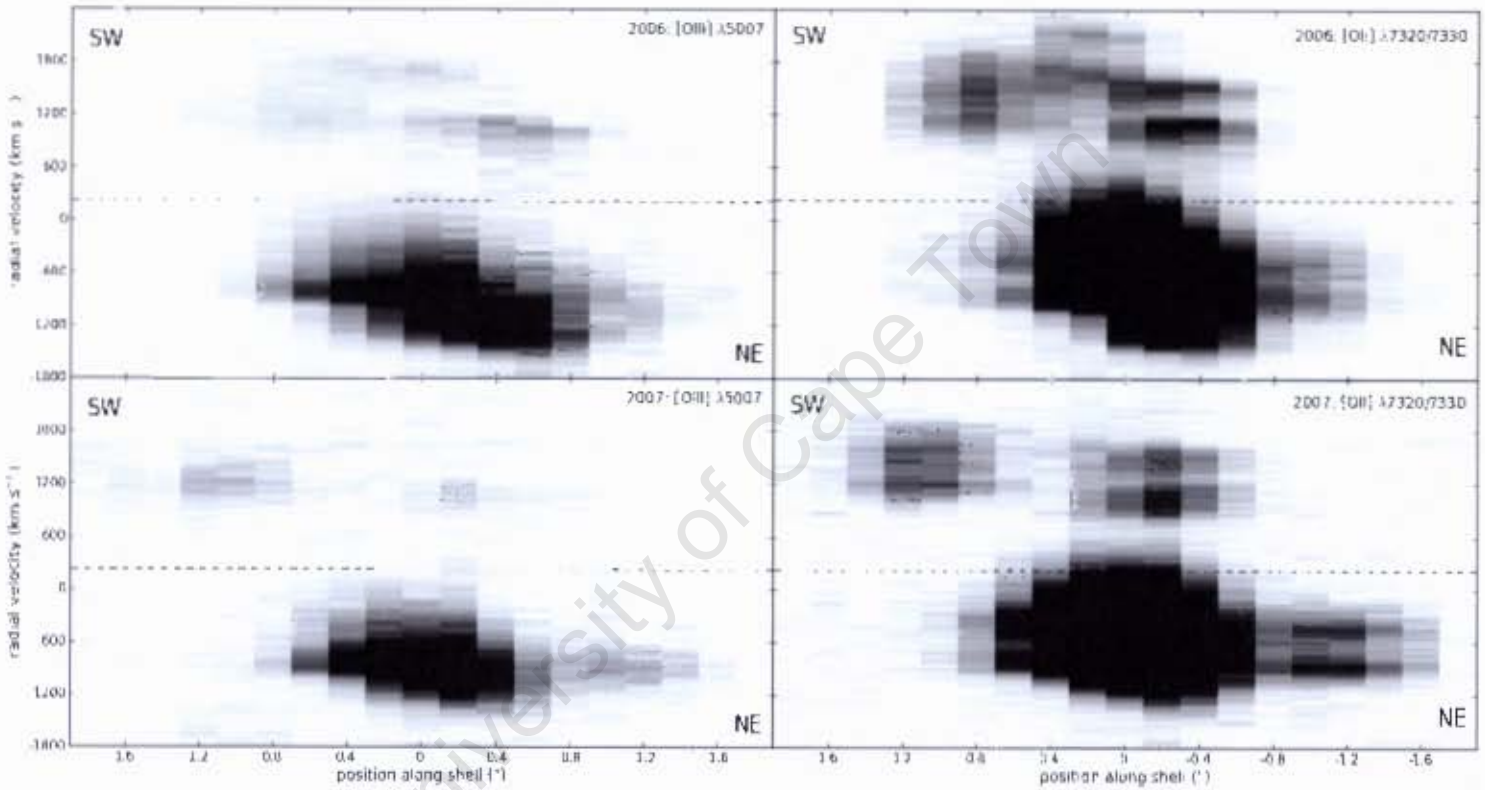

Figure 4.12: Comparison of spatially-resolved velocity profiles of the emission line [O III] λ5007 (left panels) and the [O II] λ7320/7330 doublet (with respect to the [O II] λ7320 line, right panels). In both images, several spectra, observed in 2006 (upper panel) and 2007 (lower panel), are summed along the major axis of V445 Pup, running from West to East (left to right). Dashed lines indicate the systematic velocity (224 ± 8 km s^{-1}, (Iijima & Nakanishi 2008)). Intensity ranges are 1-450 for the both lines in 2006 and 1-150 for both lines in 2007.

In the 2006 He I λ7065 line PV plot in Figure 4.11, there are two separate regions of increased intensity (to either side of the dashed line) centred around $+1200\ \mathrm{km\,s^{-1}}$ and $-900\,\mathrm{km\,s^{-1}}$ between $\sim -0\farcs8$ and $+0\farcs5$. These regions correspond to the red- and blue-shifted components of the He I λ7065 line. Each region also contains two distinct components, one on the western side (left of the nova centre) and one on the eastern side (right of the nova centre), corresponding to emission from each side of the nova shell. The offset of the components is due to the inclination of the nova ejecta to the plane of the sky. Although the velocity structure of the nova for the He I λ7065 line does not appear to change significantly from one year to the next, the western red-shifted component is relatively weaker in 2007 than in 2006, perhaps indicating changes in transparency of the SW nova shell.

In 2006, the peak intensity for the red-shifted and blue-shifted components of the NE lobe is at $\sim +1110\ \mathrm{km\,s^{-1}}$ and $-1270\ \mathrm{km\,s^{-1}}$ respectively. Similarly, the components of the SW lobe are situated at $\sim +1700\ \mathrm{km\,s^{-1}}$ and $-860\ \mathrm{km\,s^{-1}}$ respectively with a measurement error of $\pm$ 40 $\mathrm{km\,s^{-1}}$ for both lobes. It follows that the mean radial velocities for the NE and SW lobes are then $-80\ \mathrm{km\,s^{-1}}$ and $+420\ \mathrm{km\,s^{-1}}$, respectively. This results in a mean radial velocity for both lobes of $\sim +170\ \mathrm{km\,s^{-1}}$. Considering possible measurement errors, this agrees with the systematic velocity of $+224 \pm 8\ \mathrm{km\,s^{-1}}$.

The 2006 and 2007 PV plots of [O III] λ5007 and [O II] λ7320 7330 are compared in Figure 4.12. In this figure, the velocity profiles from 15 pairs of summed fibres along the major axis from West to East (left to right) are plotted for the two lines in 2006 and 2007 and the dashed line indicates where the systematic velocity lies. The intensity range of the [O III] λ5007 line profile is smaller than that of the [O II] λ7320 7330 line profile for easier comparison of the different components at the two epochs.

Compared to the PV profiles of the He I λ7065 line previously shown in Figure 4.11, the general appearance of the emission remains the same. The red- and blue-shifted components of the lines can clearly be seen between $-0\farcs6$ and $+0\farcs6$ at around $-900\ \mathrm{km\,s^{-1}}$ and $+1350\,\mathrm{km\,s^{-1}}$ respectively, with the blue component having the greatest intensity. As the [OII] λ7320/7330 line is a blended doublet, the emission appears to extend further than that of the He I lines. Most clearly seen in 2006 for both oxygen lines, each component has separate emission from the NE and SW lobes, such that the emission from the NE lobe is traveling faster towards us.

In the PV profiles of both forbidden oxygen lines, the western red-shifted line component is relatively weaker in 2007 than in 2006. This was also the case in the PV profile of the He I λ7065 line and therefore implies that this feature is possibly the result of an evolving nova shell. This is discussed in more detail in Chapter 5.1.

The forbidden oxygen PV line profiles differ from the He I line profiles at the extremes

of the shell, where there appears to be an extra amount of emission, more clearly seen in the [O II] λ7320/7330 profile. These excesses relate to the excess regions seen in the on-sky projections of the forbidden oxygen lines (Figures 4.5, 4.6, 4.7 and 4.8). According to the [O II] λ7320/7330 PV profile, the excess emission for the NE lobe and SW lobes lies $\sim \pm 1''.0$ from the novae centre in 2006 and $\sim \pm 1''.2$ from the nova centre in 2007. This increase in distance from the centre, from one epoch to the next, can be clearly seen by comparing the two [O II] λ7320/7330 PV plots.

4.3.2 Velocity Measurements

Table 4.4: Measured blue-shifted (v_{blue}) and red-shifted (v_{red}) He I λ7065 radial velocities

	NE LOBE			
Year	v_{blue}	FWHMv_{blue}	v_{red}	FWHM$_{red}$
2006	-1280 ± 16	450	$+1065 \pm 17$	249
2007	-1174 ± 17	503	$+1118 \pm 17$	230
	SW LOBE			
Year	v_{blue}	FWHMv_{blue}	v_{red}	FWHM$_{red}$
2006	-822 ± 17	320	$+1703 \pm 19$	515
2007	-835 ± 17	253	$+1578 \pm 48$	899

Year	NE average	SW average	Total average
2006	-107 ± 23	$+441 \pm 25$	$+167 \pm 35$
2007	-28 ± 24	$+371 \pm 51$	$+172 \pm 56$

All calculated values have units of km s^{-1}.

In order to improve the accuracy of velocity measurements for each of the line components, I extracted and summed spectra from a group of seven fibres in each lobe for the He I λ7065 line at both epochs (fibre positions are indicated in the right panels of Figures 4.13 and 4.14). The He I λ7065 line was chosen since it provides the clearest view of the velocity structure of the nebula for the two epochs with no significant contamination from neighbouring lines. Although some seeing-limited blending occurred, I was able to fit a Gaussian to each of the components and could therefore calculate separate velocities, as shown in Table 4.4. In Figures 4.13 and 4.14, the separate line components of He I λ7065 for the two lobes are compared in 2006 and 2007 respectively.

From 2006 to 2007, the line profiles and their ratios do not change significantly and the FWHM appears to stay approximately constantly between each component. Most of the line profiles have one steep side and one gradually declining side (except for the red components of the SW lobe where the signal was too weak). This profile shape is possibly due to an optical depth effect within the nova shell (Bode & Evans 2008).

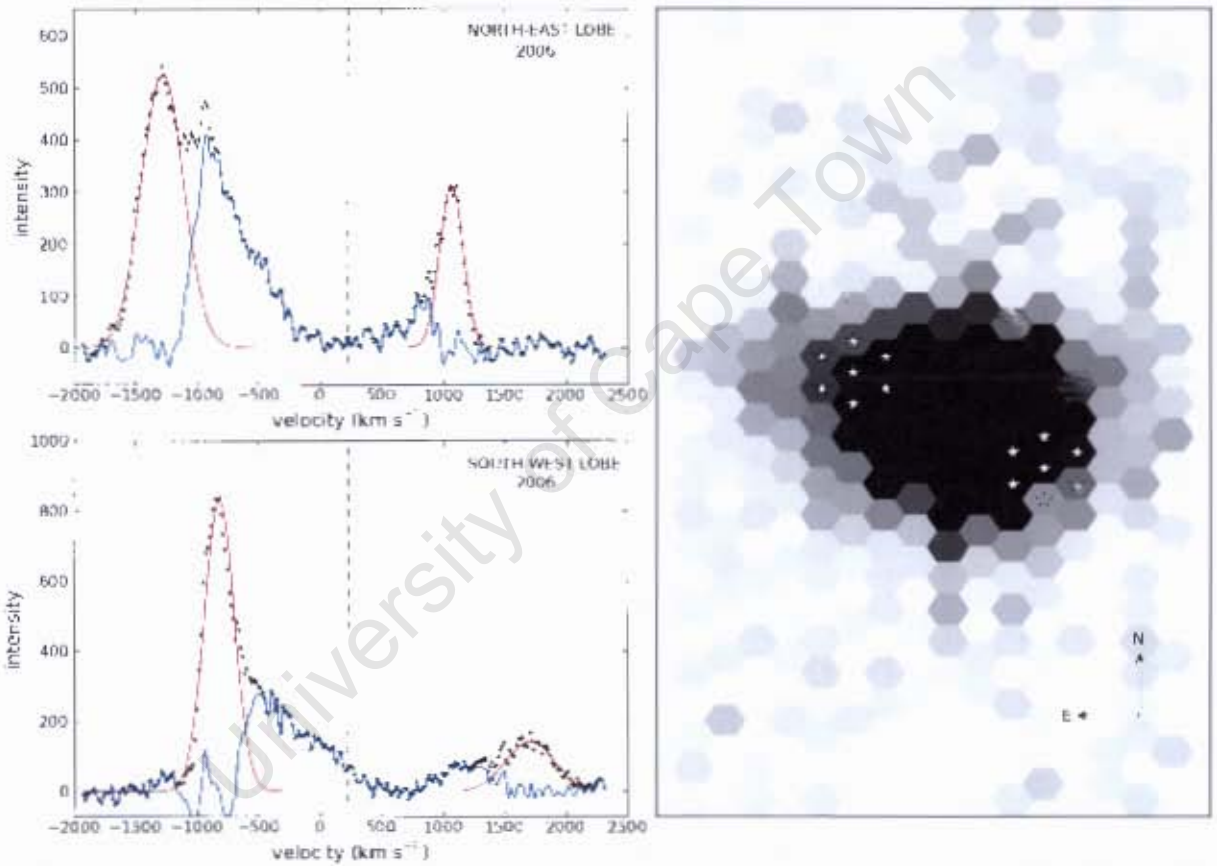

Figure 4.13: Left: Velocity line profiles of the NE (top) and SW (bottom) shell in 2006 as seen in the He I λ7065 line. Right: On-sky projection showing the placement of the seven fibres across each of the two shells. A Gaussian is fit per component (red lines) and subtracted from the full data set (black circles) to get the resultant curve (blue solid line). The systematic velocity is marked by a vertical dashed line.

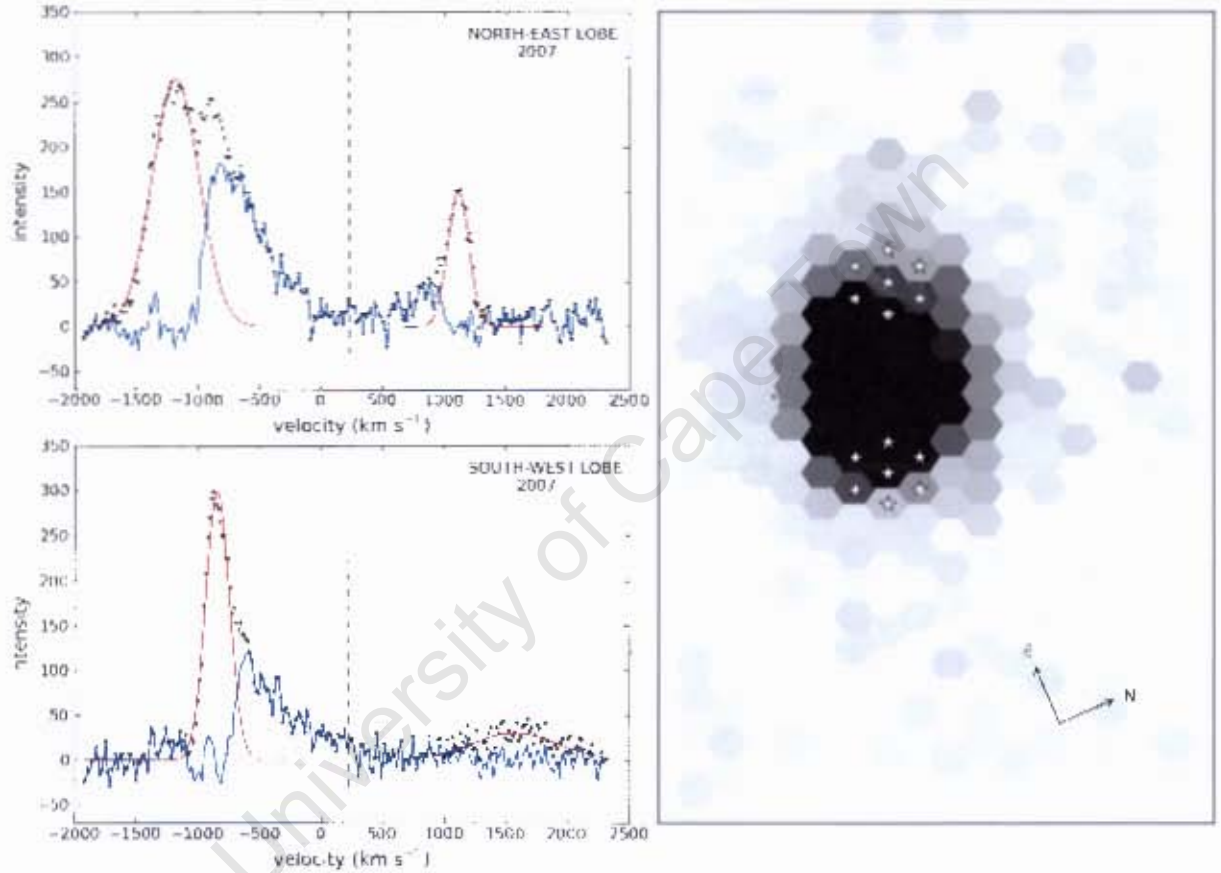

Figure 4.14: Left: Velocity line profiles of the NE (top) and SW (bottom) shell in 2007 as seen in the He I λ7065 line. Right: On-sky projection showing the placement of the seven fibres across each of the two shells. A Gaussian is fit per component (red lines) and subtracted from the full data set (black circles) to get the resultant curve (blue solid line). The systematic velocity is marked by a vertical dashed line.

4.3.3 The Excess Oxygen Emission

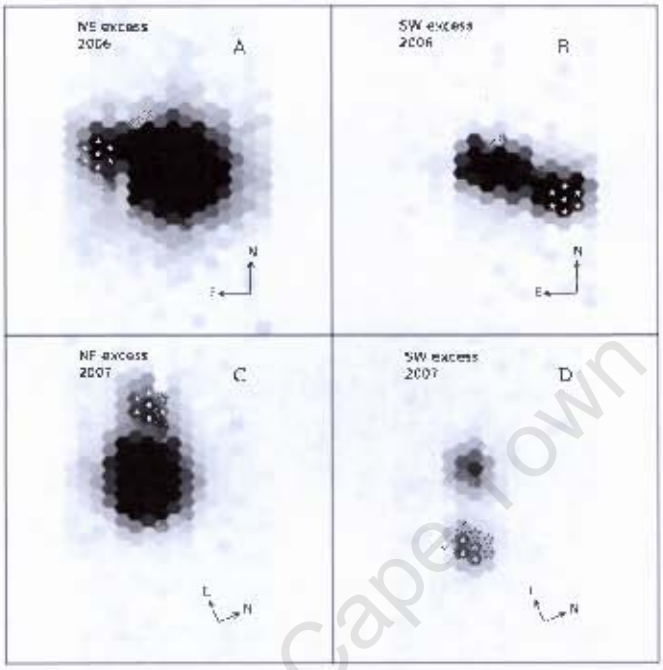

Figure 4.15: Comparative on-sky projections of the [O II] λ7320/7330 doublet line showing the NE and SW excess emission (indicated by white stars in the left and right panels, respectively) observed in 2006 (upper panels) and 2007 (lower panels). Maps in panels A and C consist of summed spectra from -900 km s^{-1} to -700 km s^{-1} and panels B and C are summed spectra from $+1300$ km s^{-1} to -1500 km s^{-1}. All maps have an intensity range of 1-1000.

In Section 4.2.1, I discussed the on-sky projections of the prominent emission lines in V445 Pup. In the spatial intensity maps of the [O II] λ7320/7330 and [O III] λ5007 lines in 2006 and 2007 (Figures 4.5, 4.6, 4.7 and 4.8), unexpected regions of emission occur at the extremes of the nova shell with velocities exceeding that of the main shell components. Also intriguing is that the excess emission is not obvious in the on-sky projections of the He I λ7065 line at the same velocities. In Figure 4.15, the NE and SW excess regions are highlighted (using white star markers) and compared in on-sky projections of the [O II] λ7320/7330 doublet for 2006 and 2007. Each projection is the summed spectra from a 200 km s^{-1} velocity range, with summed spectra from -900 km s^{-1} to -700 km s^{-1} in panels A and C, and from $+1300$ km s^{-1} to -1500 km s^{-1} in panels B and D.

The middle panels of Figures 4.16, 4.17, 4.18 and 4.19 show the spectra centred on each region of excess emission as identified in Figure 4.15. In the middle panel of Figure 4.16, the

2006 excess emission along the SW extension of the major axis is presented. In this spectrum, the presence of blue-shifted emission from the [O II] λ7320/7330 line indicates that there is some contamination from the SW shell (due to seeing smearing). The spectrum of the SW shell (in 2006) is shown in the top panel of Figure 4.16 and indeed, the [O II] blue-shifted emission is the dominant component here. In order to subtract this contamination, I first scaled the SW shell spectrum to the peak of the [O II] blue-shifted emission in the excess emission spectrum and then subtracted the scaled shell spectrum from the excess emission spectrum. This resulted in the 'cleaned' spectrum of the excess emission shown in the lower panel of Figure 4.16. This procedure was repeated for 2007 in order to remove a similar contamination from the SW shell in the excess emission spectrum of 2007 (Figure 4.17).

In the lower panel of Figure 4.16, two emission lines, [O III] λ5007 and [O II] λ7320/7330, are clearly present and can be cleanly resolved with one or two Gaussian profiles at red-shifted velocities. These two emission lines are also present in 2007 (visible in the lower panel of Figure 4.17), in addition to a weak [O III] λ4959 line which is not clearly visible in the 2006 spectrum. Comparing 2007 data with 2006 data, the [O III] λ5007 intensity peak is relatively stronger compared to the [O II] λ7320/7330 intensity peak in 2007. For future reference, I will refer to the line ratio of [O III] λ5007 to [O II] λ7330 as $O_{3/2}$.

The procedure to subtract the NE shell contamination from the excess emission region along the NE axis in 2006 and 2007 was more difficult. In the middle panel of Figure 4.18, the NE excess emission spectrum is presented. In this spectrum, the [O II] and [O III] lines that are due to shell contamination have blended with the blue-shifted excess emission lines. Therefore, in order to subtract the contamination, the NE shell spectrum (upper panel of Figure 4.18) is first scaled to the He I λ7065 line in the excess spectrum. This scaled spectrum is then subtracted from the excess emission spectrum to get the 'clean' excess emission spectrum shown in the lower panel of Figure 4.18. This procedure was repeated for the spectrum of the excess emission along the NE axis in 2007.

The cleaned NE excess emission spectra in 2006 exhibits three emission lines: [O II] λ7320/7330, [O III] λ5007 and a weaker [O III] λ4959 line. In 2007, only the two emission lines, [O II] λ7320/7330 and [O III] λ5007 are clearly visible in the excess emission spectrum. In the NE excess spectrum, $O_{3/2}$ appears to be greater in 2006 than in 2007 (in contradiction with the SW excess spectrum).

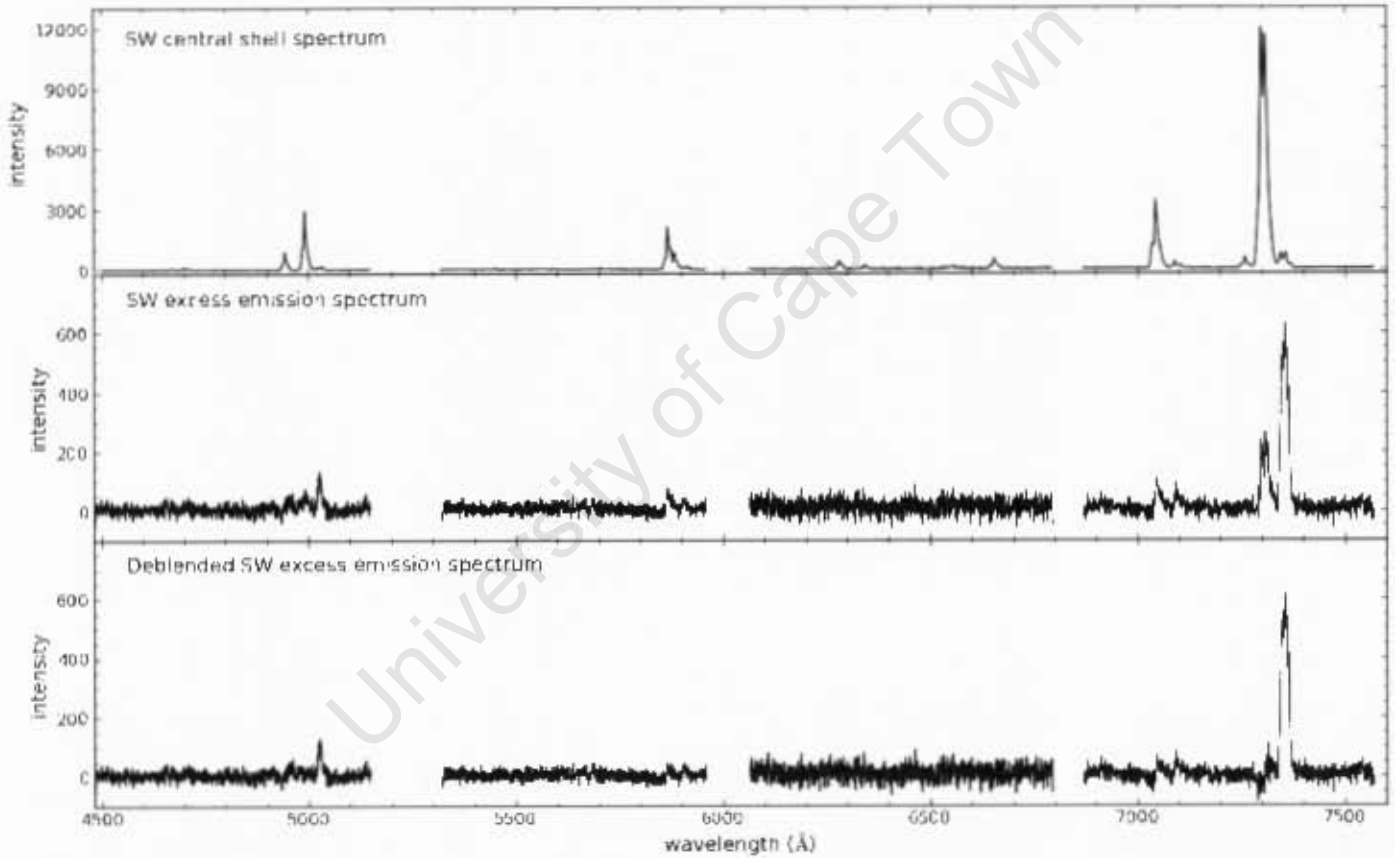

Figure 4.16: Middle panel: The 2006 spectrum centred on the region of excess [O II] λ7320/7330 and [O III] λ5007 emission along the SW extension of the major axis of V445 Puppis (sampled over 7 fibres, see Figure 4.15, panel B). Lower panel: The 2006 difference spectrum, where the 2006 SW shell emission (upper panel) has been scaled and subtracted from the excess emission spectrum (middle panel) showing the residual emission along the extremes of the SW extension of the nova.

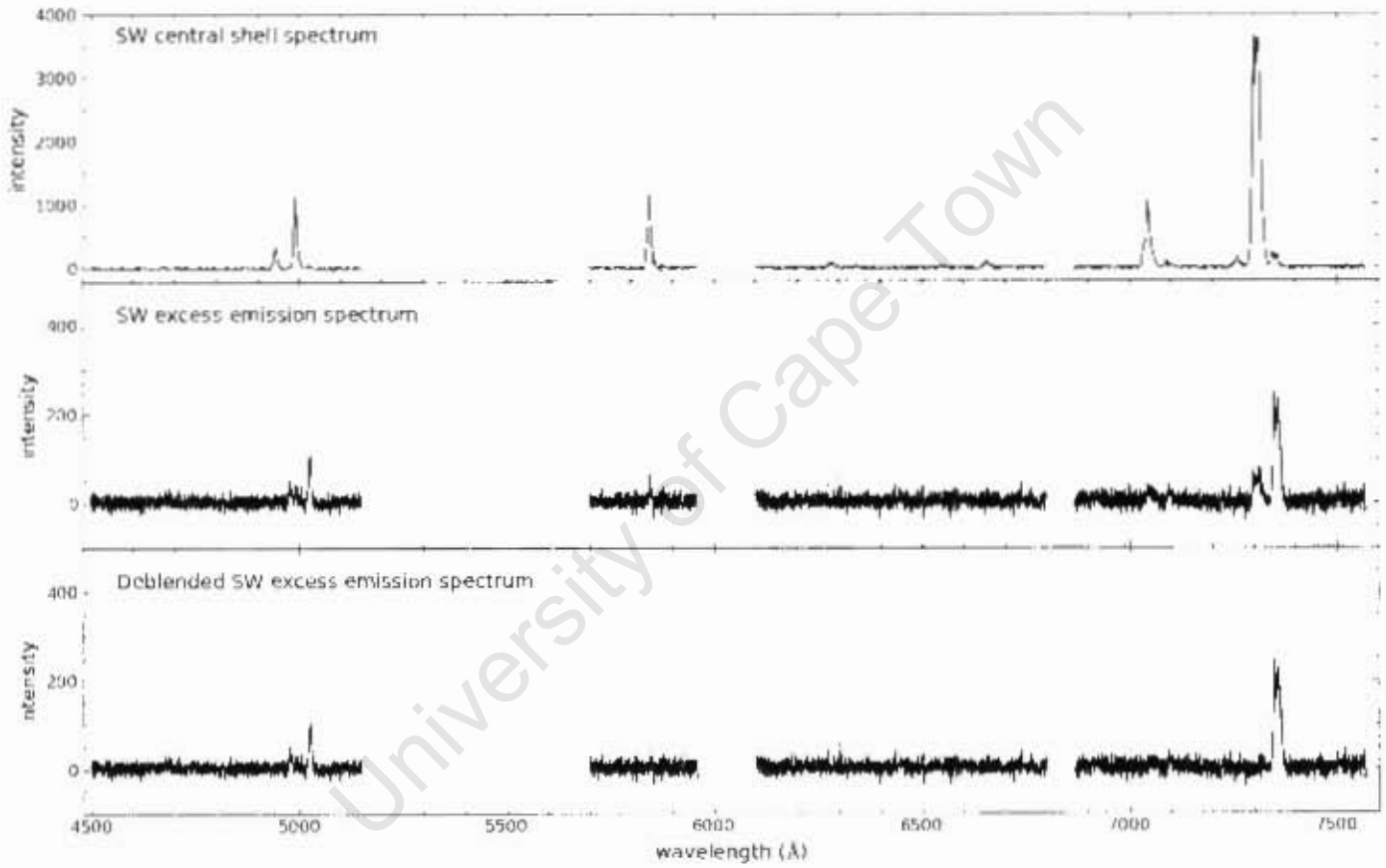

Figure 4.17: Middle panel: The 2007 spectrum centred on the region of excess [O II] λ7320/7330 and [O III] λ5007 emission along the SW extension of the major axis of V445 Puppis (sampled over 7 fibres, see Figure 4.15, panel D). Lower panel: The 2007 difference spectrum, where the 2007 SW shell emission (upper panel) has been scaled and subtracted from the excess emission spectrum (middle panel) showing the residual emission along the extremes of the SW extension of the nova.

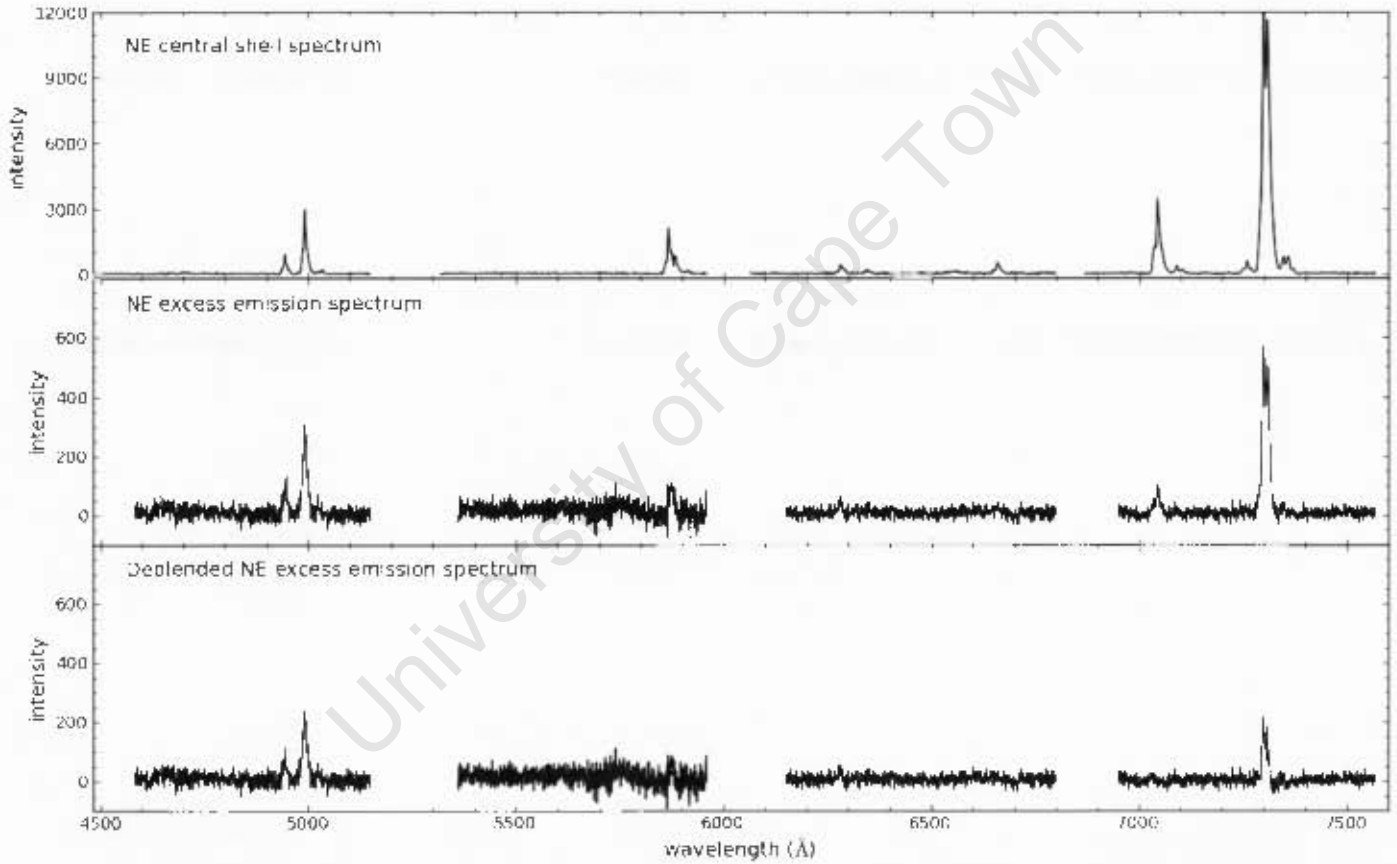

Figure 4.18: Middle panel: The 2006 spectrum centred on the region of excess [O II] λ7320/7330 and [O III] λ5007 emission along the NE extension of the major axis of V445 Puppis (sampled over 7 fibres, see Figure 4.15, panel A). Lower panel: The 2006 difference spectrum, where the 2006 NE shell emission (upper panel) has been scaled and subtracted from the excess emission spectrum (middle panel) showing the residual emission along the extremes of the NE extension of the nova.

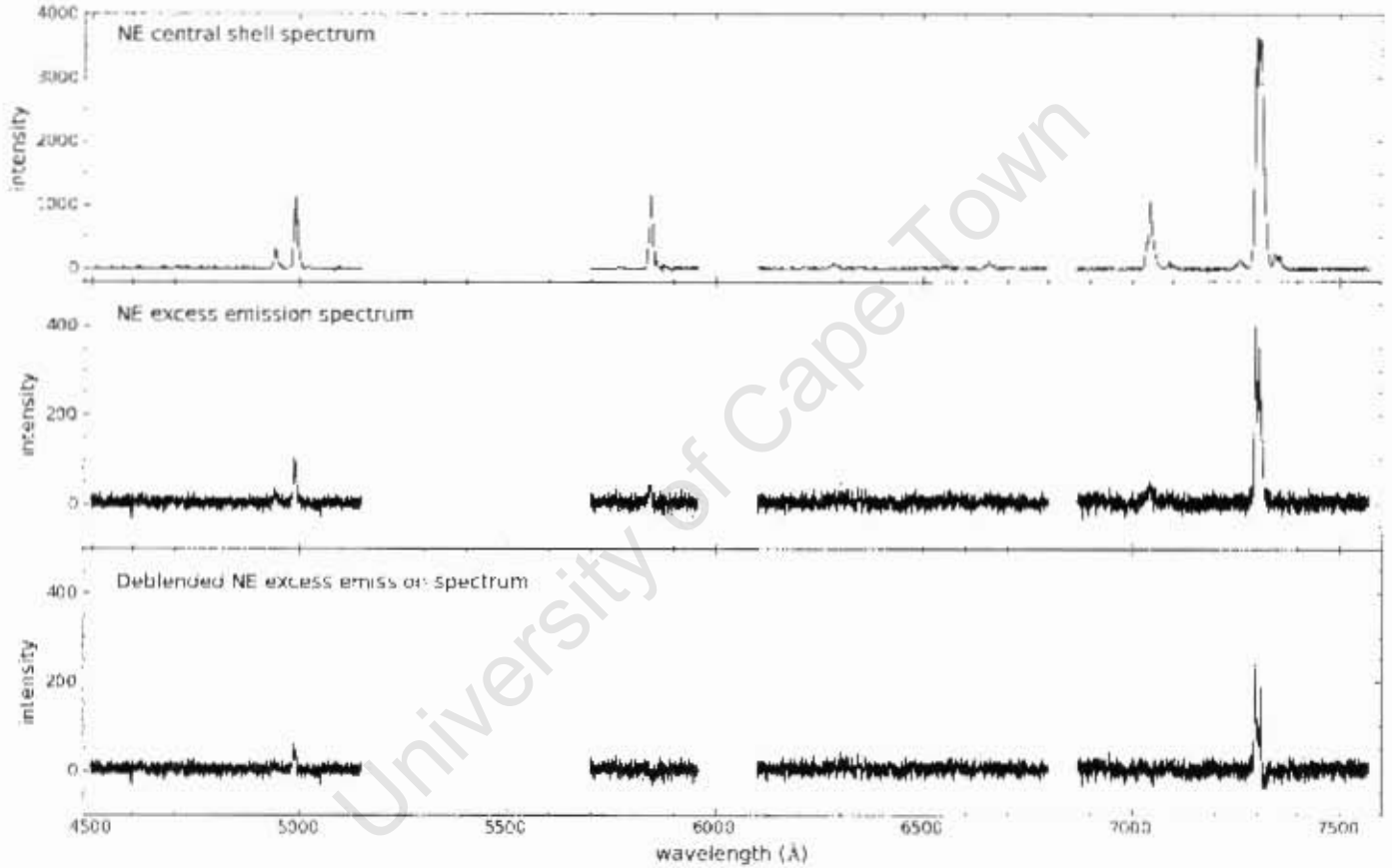

Figure 4.19: Middle panel: The 2007 spectrum centred on the region of excess [O II] λ7320/7330 and [O III] λ5007 emission along the NE extension of the major axis of V445 Puppis (sampled over 7 fibres, see Figure 4.15, panel C). Lower panel: The 2007 difference spectrum, where the 2007 NE shell emission (upper panel) has been scaled and subtracted from the excess emission spectrum (middle panel) showing the residual emission along the extremes of the NE extension of the nova.

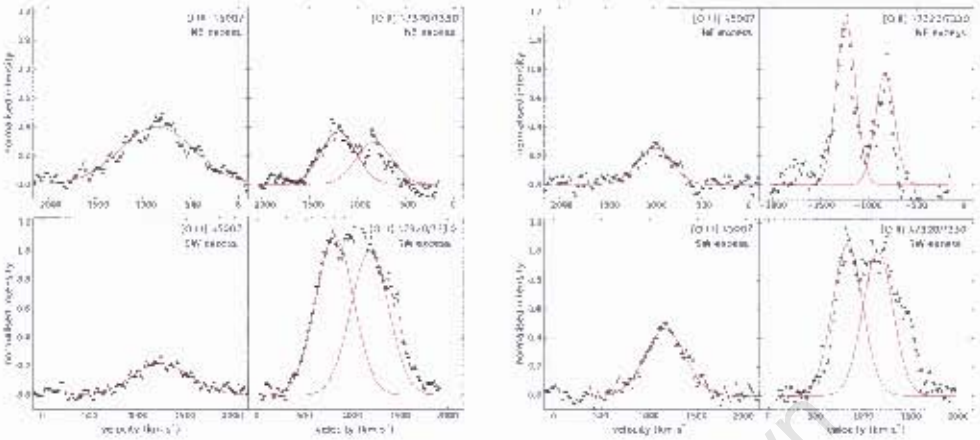

(a) Epoch 1: 4 January 2006 (b) Epoch 2: 8 January 2007

Figure 4.20: Comparison of [O III] λ5007 and [O II] λ7320, 7330 excess lines for the NE and SW knots in 2006 (left panels) and 2007 (right panels). A Gaussian (red solid line) is fit over the spectrum (black points), which is the combination of seven fibres containing the respective knot (see Figure 4.15). Intensities in all figures are normalised to the peak intensity of the [O II] λ7330 line in the 2006 SW excess spectrum.

A closer inspection of the excess lines is displayed in Figure 4.20. A single Gaussian is fit to the [O III] λ5007 line profile for both knots in 2006 and 2007. As two peaks are clear in the [O II] λ7320/7330 doublet, these line profiles need to be fit with two Gaussians. This is shown in Figure 4.20. The central wavelength for each line is documented in Table 4.5, along with their respective radial velocities calculated using the Doppler Shift equation. In Table 4.5, $O_{3/2}$ in the NE excess region is greater in 2006 ($O_{3/2} = 0.40 \pm 0.02$) than in 2007 ($O_{3/2} = 0.26 \pm 0.02$). On the other hand, in the SW excess region, $O_{3/2}$ is smaller in 2006 ($O_{3/2} = 0.22 \pm 0.01$) than in 2007 ($O_{3/2} = 0.46 \pm 0.03$).

The average velocity for each knot in 2006 and 2007, respectively, are listed in Table 4.6. In each year, the average radial velocities, relative to the systematic velocity, of the NE and SW knot are approximately equal in opposite directions ($\sim \pm 1000$ km s^{-1}). This is what is expected from a bipolar outflow. The velocities listed in Table 4.6 result in excessively high deprojected velocities which could be the result of bow-shocks or an ionisation front in the nova. This is discussed in detail in Chapter 5.1.

Table 4.5: Excess emission velocity measurements

[O III]	Wavelength (Å)	Intensity$_{norm}$ [b]	Velocity (km s^{-1})
NE 2006	4992.68 ± 1.35	0.398 ± 0.016	−848 ± 81
SW 2006	5027.74 ± 1.40	0.218 ± 0.012	+1252 ± 84
NE 2007	4990.32 ± 1.33	0.256 ± 0.021	−989 ± 80
SW 2007	5026.41 ± 1.25	0.461 ± 0.029	+1172 ± 75
[O II][a]	Wavelength (Å)	Peak Intensity$_{norm}$ [b]	Velocity (km s^{-1})
NE 2006 $G1$	7300.30 ± 1.41	0.362 ± 0.017	−779 ± 58
NE 2006 $G2$	7309.96 ± 1.35	0.293 ± 0.081	−823 ± 55
SW 2006 $G1$	7349.34 ± 1.36	1.100 ± 0.028	+1238 ± 56
SW 2006 $G2$	7355.66 ± 1.43	1.000 ± 0.028	+1184 ± 58
NE 2007 $G1$	7299.64 ± 1.46	1.146 ± 0.066	−816 ± 60
NE 2007 $G2$	7309.49 ± 1.16	0.764 ± 0.057	−826 ± 47
SW 2007 $G1$	7350.57 ± 1.43	1.052 ± 0.056	+1256 ± 58
SW 2007 $G2$	7358.31 ± 1.43	1.000 ± 0.066	+1151 ± 59

[a] This doublet line is fit with two Gaussians, $G1$ and $G2$.
[b] Intensities are normalised with respect to the [OII] λ7330 peak intensity of the SW knot at each epoch.

Table 4.6: Average velocity, $< v >$, for each knot

2006 Knot	$< v >$ (km s^{-1})	$< v >_{rel}$ [a] (km s^{-1})
NE	−817 ± 114	−1041 ± 114
SW	+1224 ± 117	+1000 ± 117
2007 Knot	$< v >$ (km s^{-1})	$< v >_{rel}$ [a] (km s^{-1})
NE	−877 ± 110	−1101 ± 111
SW	+1193 ± 155	+969 ± 155

[a] $< v >_{rel}$ is the $< v >$ with respect to the systematic velocity of V445 Pup (v_{sys} = 224 ± 8 km s^{-1}, (Iijima & Nakanishi 2008))

Chapter 5

Discussion

The velocity profiles of the emission lines observed in this thesis can be modeled using the bipolar velocity field model described in Chapter 1, Equation 1.2 (Solf & Ulrich 1985). Woudt et al. (2009) derived best-fit model parameters while using this equation to model the velocity profile of He I λ7065. In this chapter, I analyse the similarities and differences between this model and the results presented here. In addition, two main results are discussed in this chapter, namely the variations and similarities in the data between 2006 and 2007 and the possibility of highly-collimated outflows and jets within the nova shell.

5.1 Spatio-kinematic Modeling of V445 Pup

The best-fit model parameters calculated by Woudt et al. (2009) are shown in Table 5.1. In Figure 5.1, these parameters are used in the bipolar velocity model to illustrate the velocity profile of V445 Pup at the two epochs analysed in this dissertation (4 January 2006 and 8 January 2007). In this figure, the bipolar lobes of the nova and the narrow waist are clearly visible. The inclination is such that the NE lobe is closer to the observer. With the aid of the illustration in the lower panel of Figure 5.1, it is possible to visualize some of the results in this dissertation, such as the on-sky projections of the nova emission in Figures 4.3 to 4.8. The peak intensity in each of the on-sky projections shift from the NE lobe to the SW lobe, back to the NE lobe and then to the SW lobe again. This is understandable in light of the observed inclination of the nova axis to the plane of the sky in Figure 5.1.

In Figure 5.2, I plotted some results of this dissertation over the spatio-kinematic model shown in Figure 5.1. While the radial velocities of He I λ7065 agree well with the model, the model fails when trying to describe the radial velocities associated with the excess emission regions. This is discussed in more detail later in this section.

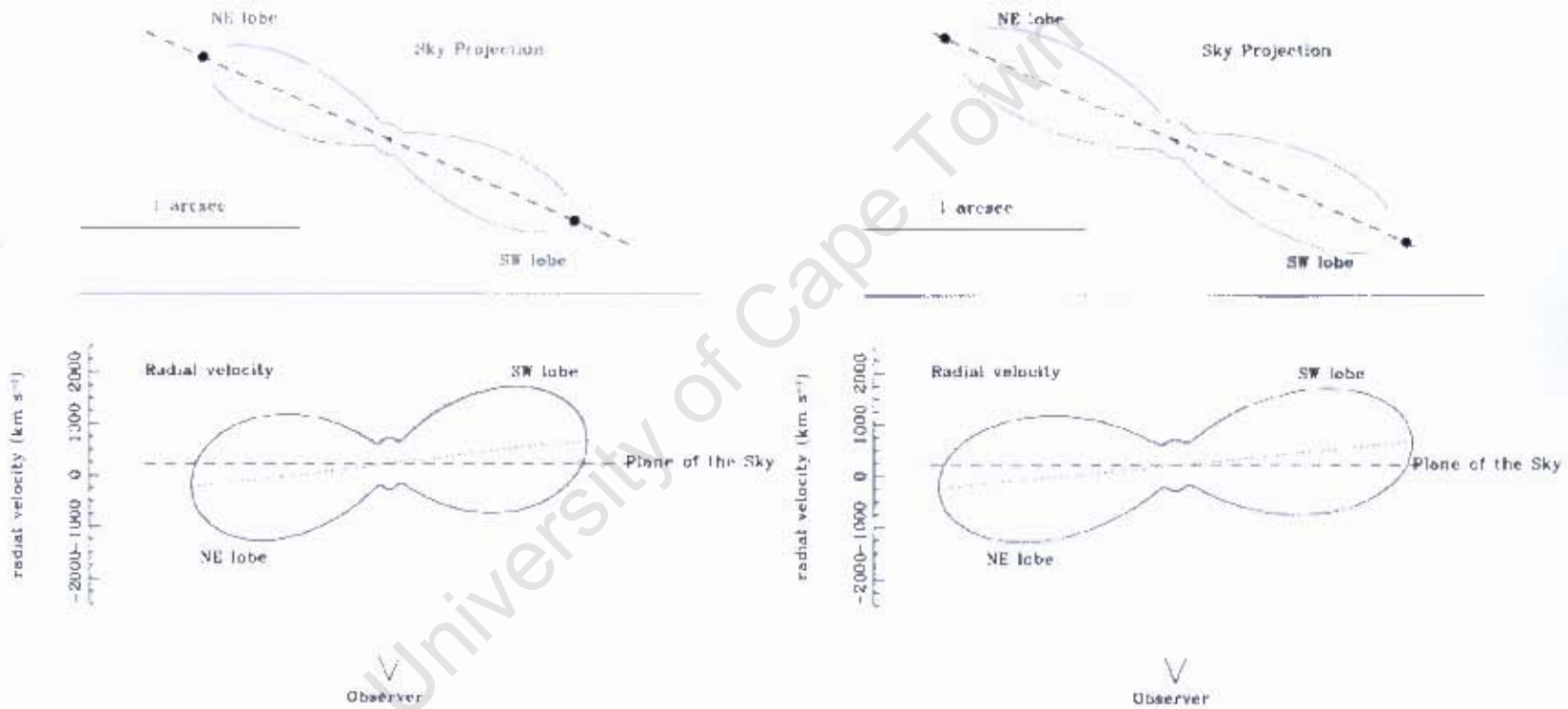

(a) Epoch 1: 4 January 2006

(b) Epoch 2: 8 January 2007

Figure 5.1: Spatio-kinematic model of V445 Pup for 4 January 2006 (Left) and 8 January 2007 (Right) using the best-fit model parameters deduced by Woudt et al. (2009). Each upper panel shows the on-sky projection of the model, whereas the lower panels display the expected radial velocity from the different parts of the nova shell.

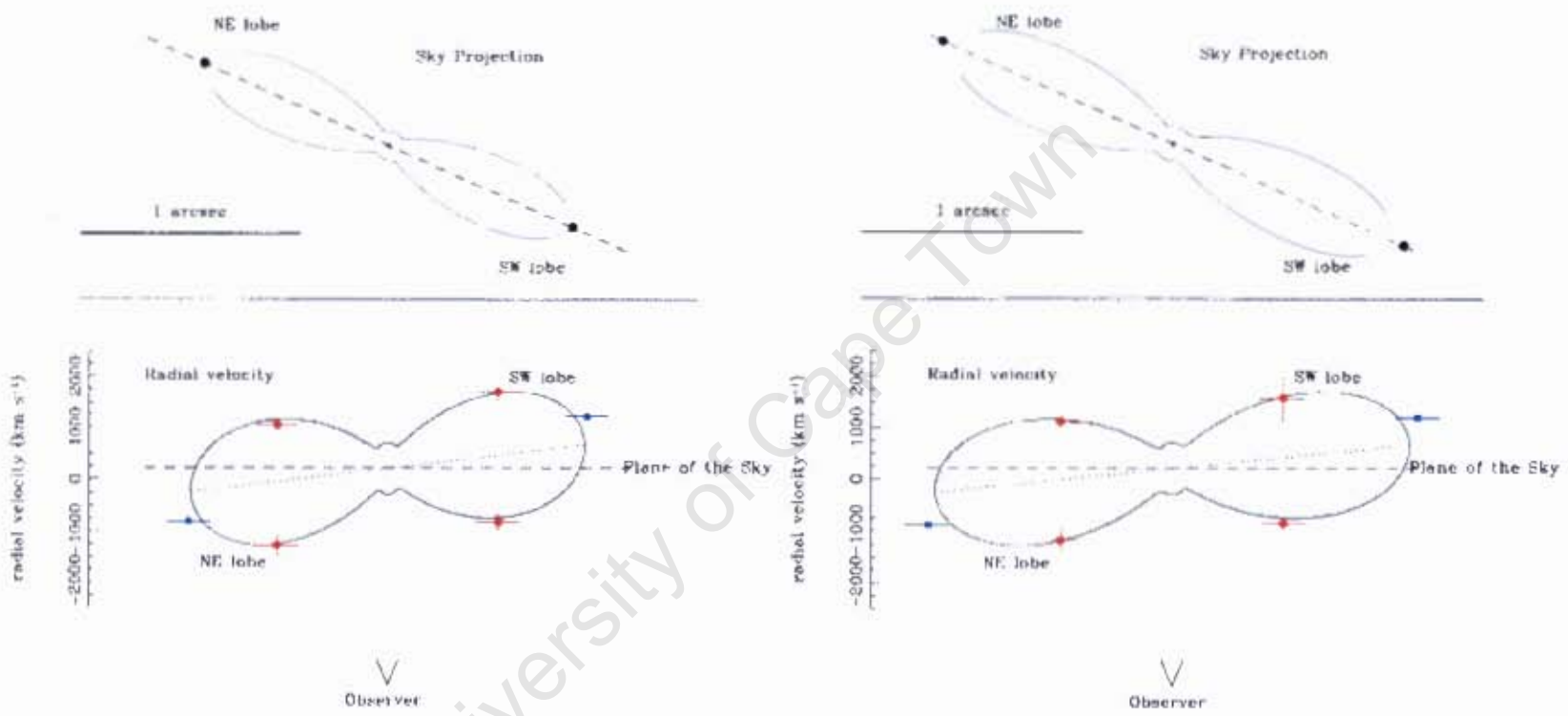

(a) Epoch 1: 4 January 2006

(b) Epoch 2: 8 January 2007

Figure 5.2: Dissertation results are plotted over the spatio-kinematic model of V445 Pup for 4 January 2006 (Left) and 8 January 2007 (Right) using the best-fit model parameters deduced by Woudt et al. (2009). Each upper panel shows the on-sky projection of the model, whereas the lower panels display the expected radial velocity from the different parts of the nova shell. The model agrees with the radial velocities for the He I λ7065 line (red circles) but fails with the excess emission radial velocities (blue squares).

Table 5.1: Best-fit bipolar velocity model parameters calculated by Woudt(2009)

Model Parameter	Value
PA shell	66 deg
α	12
i_{shell}	3.9 ± 0.4 deg
v_c	500 km s^{-1}
v_p	6720 ± 250 km s^{-1}
v_{knots}	$8450 \pm$ km s^{-1}
d	8.2 ± 0.3 kpc

From 2006 to 2007, the radial velocities in the spatio-kinematic model shown in Figure 5.1 did not change significantly. This agrees with the results presented in this work. For example, the central spectrum of the nova shell (Figures 4.1 and 4.2) did not change significantly from 2006 to 2007. In both years, the spectra featured strong emission lines of [O III] λ5007, He I λ5876, He I λ7065 and the doublet [O II] λ7320 7330. It also featured a few weaker emission lines and no evidence of hydrogen, which is consistent with previous spectrographic observations (Woudt et al. 2009). As the spectra from both years feature these specific emission lines, it follows that the shell maintained its chemical composition from 2006 to 2007, consisting of regions of high- and low-density ionised gas with a hot ionising interior, associated with the white dwarf. The normalised intensity (with respect to the He I λ7065 emission line) of all but one of the emission lines remained approximately constant from 2006 to 2007. Although the exception to this, He I λ5876, increased significantly from 2006 to 2007, this is most probably due to the poor extraction in CCD 3 and CCD 8.

While analysing the differences between 2006 and 2007 position-velocity maps of three of the lines (He I λ7065, [O III] λ5007 and [O II] λ7320 7330), it became apparent that a portion of the nova shell had evolved differently from the rest of the shell. In the maps, the red-shifted component of the SW shell was relatively weaker in 2007 than in 2006. This component originates in the material moving away from the observer in the South-Western lobe. Therefore, it is possible some event occurred between the two epochs to cause the SW lobe to become less transparent to light on the far side of the nova. This event would have to be localised to the SW lobe as the NE lobe did not exhibit the same features. More recent observations of the nova shell should help to determine the source of this spectral feature.

The appearance of He I λ7065 emission within the nova shell remains largely unchanged from 2006 to 2007. On the other hand, in both years, an interesting excess of oxygen is observed at the extremes of both lobes in the spatial intensity maps of the doublet [O II] λ7320 7330 (Figures 4.5 and 4.6) and in the maps of [O III] λ5007 (Figures 4.7 and 4.8). This should be compared to the intensity and velocity maps of He I λ7065 where no excess was observed in the same regions. It is in these excess emission regions that the bipolar shell velocity model begins to fail. This is shown in Figure 5.2 where the excess emission points clearly lie outside the model.

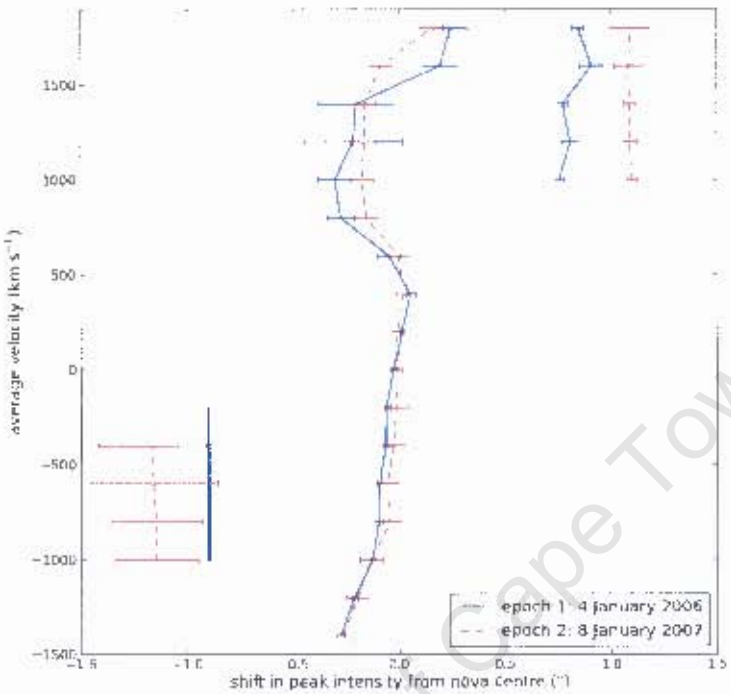

Figure 5.3: Comparison of the 2006 and 2007 shift in arcsec of the peak intensity of the [O II] λ7320/7330 doublet, along the major axis of the shell relative to the centre of V445 Pup (negative offset = North-East) across 18 velocity intervals.

In Figure 5.3, the peak intensity shifts of the [OII] λ7320/7330 doublet from 2006 and 2007 are compared. As there is an uncertainty of around 0.″1 in the position of the nova centre, the 2006 data has been shifted by 0.″1 with respect to its original position in Figure 1.9 in order to align with the 2007 data. In Figure 5.3, the intensity shifts associated with the nova shell in 2006 and 2007 agree well with each other. On the other hand, the excess clearly moves outward from $\sim$ 0.″9 from the nova centre in 2006 to $\sim$ 1.″1 from the nova centre in 2007. According to a linear expansion model devised by Woudt et al. (2009), the knots are expected to lie around 0.″914 in 2006 and around 1.″134 in 2007. It is therefore likely that the excess regions are associated with the knots, expanding linearly outwards by $\sim$ 0.″217 + 0.″010 per year. The expected positions of the knots in 2006 and 2007, respectively, are plotted over the bipolar velocity field model in the upper panel of Figure 5.1. From an extrapolation of the linear expansion of the knots back to the nova centre, Woudt et al. (2009) found that the knots could have coincided with a strong radio flare $\sim$ 345 days after outburst observed by Rupen et al. (2001). Shortly following the radio flare, there was a drop in the V band which could indicate a radio jet ejection, as was the case with the

symbiotic nova CH Cygni (Weston & Sokoloski 2011).

In 2007, the intensity of the [O III] λ5007 SW excess appears to be greater than the intensity of the nova shell. Yet in 2006, for the same line emission, the SW excess intensity is weaker than the nova shell intensity which can be seen when comparing Figures 4.8 and 4.7. This observation possibly implies that the ratio of low-density ionised gas surrounding the fast-moving SW knot to the low-density ionised gas in the nova shell was greater in 2007 than in 2006. This is not observed in a comparison of the [O II] λ7320/7330 excess emission where, in both years, the intensity of the excess emission is weaker than the nova shell emission.

V445 Pup exhibits unusually large expansion velocities for the typical classical nova, especially for the knots and in the excess emission regions. From their spatio-kinematic model, Woudt et al. (2009) deduced a bulk velocity of $v_p \sim 6720 \pm 650\,\mathrm{km\,s^{-1}}$ and a knot expansion velocity of $v_{knots} \geq 8000\,\mathrm{km\,s^{-1}}$ from measurements of the knots' motion across the sky. For comparison, the average classical nova has an expansion velocity of $\geq 2000\,\mathrm{km\,s^{-1}}$ (Bode & Evans 2008). Although V445 Pup has a comparatively higher expansion velocity, the nova can be compared to the recurrent nova RS Oph, which expands at $\sim 5600 \pm 1100\,\mathrm{km\,s^{-1}}$ (Bode et al. 2007).

Due to the inclination of the nova axis to the plane of the sky, the deprojected velocities are going to be significantly higher than the observed radial velocities. Therefore in 2006, the deprojected radial velocities of the [O III] λ5007 excess emission regions for the NE and SW lobes (in the frame of the nova) are $\sim -15300\,\mathrm{km\,s^{-1}}$ and $+14700\,\mathrm{km\,s^{-1}}$, respectively, and then $\sim -16200\,\mathrm{km\,s^{-1}}$ and $+14200\,\mathrm{km\,s^{-1}}$, respectively, in 2007. Such huge high-velocity jets ($\geq 10000\,\mathrm{km\,s^{-1}}$) indicate the presence of a massive white dwarf in V445 Pup, as was modeled in U Sco by Kato & Hachisu (2003a).

These deprojected polar velocities are a factor 2.2 larger than the documented bulk velocity of $v_p \simeq 6720\,\mathrm{km\,s^{-1}}$ and a factor 1.8 larger than the velocity of the knots, $v_{knots} \simeq 8450\,\mathrm{km\,s^{-1}}$ (Woudt et al. 2009). There are two possible explanations for these excessively high velocities. The high velocities either result from an ionisation front or they arise from bow shocks due to highly collimated outflows in the nova shell. Both explanations are discussed further in Section 5.2.

5.2 Collimated Outflow and Jets in Novae

Highly collimated outflows in novae has been discussed briefly in Chapter 1 of this thesis, where RS Oph was used as an example. This is because it consists of jets of relativistic particles that are accelerated by shocks, producing synchrotron emission that can be de-

tected at radio wavelengths (Sokoloski et al. 2008). In this nova, particles are accelerated by shocks caused by the interaction of the WD ejecta with the surrounding nebula (Sokoloski et al. 2008). From high resolution adaptive optics observations of V445 Pup, Woudt et al. (2009) observed an initially narrow waist and two high speed knots in the NE and SW lobes expanding outwards at the extremes of the nova shell. They associated these features with highly collimated outflows (Woudt et al. 2009).

Although there are other novae that also feature a bipolar shell with collimated outflows, such as the RS Oph and the classical nova HR Del (Harman & O'Brien 2003), V445 Pup has the most highly collimated outflow. As it is possible to model the nova expansion of V445 Pup on the expansion of a narrow-waisted bipolar planetary nebula (Woudt et al. 2009), the narrow waist of V445 Pup is possibly formed from collimated fast winds in high density gas regions within the equatorial plane (Soker & Rappaport 2000).

It is possible that the excess oxygen, discussed in Section 5.1, arises from shock fronts at the edge of the outward ejecta in the nova lobes. This can be compared to one-dimensional hydrodynamical planetary nebula models (Schönberner et al. 2005, Raga et al. 2008) where the measured edges of the planetary nebula shell have different velocities to those measured with spectroscopy. Some planetary nebulae have been shown to have compact knots or jet structures called FLIERS (fast low ionisation emission regions) moving away from the central system with high velocities, similar to those seen in V445 Pup (Raga et al. 2008). In planetary nebulae, FLIERS are typically characterised by low-ionisation spectra consisting of prominent [O I], [N II] and [S II] lines. In the planetary nebula IC 4634, there is an observed enhancement of [O III] λ5007 to Hα due to ionising bow shocks that originate when the highly collimated outflows interact with the surrounding nebula material (Guerrero et al. 2008). Bow shocks are also used to explain the caps of excess [O III] λ5007 associated with jets in the planetary nebula NGC6543 (Balick & Hajian 2004).

In order to test if there was evidence of shocks in the excess regions of V445 Pup, I tried to identify any shock lines in the excess only spectra (Figures 4.16 to 4.19). I found that, while the full NE and SW excess spectra for 2006 and 2007 featured strong emission lines of [O II] λ7320/7330 and [O III] λ5007 (a good indication of bow shocks (Guerrero et al. 2008)), there was no evidence of [N II] and [S II] λ6717/6731 that would relate to shock ionisation (Woudt et al. 2009), cf RS Oph (Iijima 2009). It is possible this could just be an indication that the density in the nova is too high for these lines to form according to models by Allen et al. (2008). Unfortunately, these models have only been tested on velocities less than 1000 km s^{-1} and therefore needs to be expanded for greater velocity systems like V445 Pup.

On the other hand, the extreme deprojected velocities could be due to a moving ionisation front. If this were the case, one-dimensional hydrodynamical models of planetary

nebulae suggest these extreme velocities do not represent the bulk motion of the ejecta or of the knots (Schönberner et al. 2005). Although this mechanism was initially proposed by Fernández et al. (2004) to explain the high velocities originating from the complex structure of the planetary nebula NGC 7009, Steffen et al. (2009) later amended this, reasoning that the high velocities could possibly represent the true bulk velocity as they had found that the nebulae was fully ionised.

Further modeling of the results in this thesis may help to determine which of the two explanations, either an ionisation front or shock waves, is the most likely reason for the high measured velocities of the excess regions.

Chapter 6

Future Outlook

V455 Pup is the only observed helium nova to date and it therefore provides significant insight into the properties of helium novae. The spectrographic analysis results from this thesis can be used in various hydrodynamical models to further constrain the spatial kinematic properties of the nova and get a three dimensional picture of the expansion of the nova. Also, more monitoring of V445 Pup across a range of wavelengths is required for a better understanding of the nova source, the chemical abundances within the shell and excess regions, and the likelihood that this nova is a possible supernova Ia progenitor.

In Chapter 5 of this dissertation, the velocity profiles of the emission lines were modeled using best-fit model parameters (Woudt et al. 2009) in the bipolar velocity field model described by Solf & Ulrich (1985). Using the results of their best fit model, along with high resolution observations of the expanding nova shell, Woudt et al. (2009) were able to deduce a distance to the nova. As a more in depth study was made into the emission lines in this thesis, an improved distance estimate can be obtained using the same procedure that Woudt et al. (2009) used, by including two epochs of radial velocity information. I expect this will not change much to the derived distance as the velocity profile has not changed significantly over one year. By reducing the current uncertainty in the distance estimate, certain measured properties of the nova (such as the mass of the dust shell) will be improved and the nature of the helium nova progenitor can be better determined.

More importantly, it is possible to model the nova using the velocity measurements from this work in hydrodynamic simulations of axis-symmetric planetary nebulae. Among other possibly interesting results, this will help to estimate by what amount the documented expansion parallax underestimates the true distance to V445 Pup (Woudt et al. 2009). One such simulation, designed by Raga et al. (2008), is used to model planetary nebula knots that move supersonically with respect to the main ejecta (called FLIERS) as ionisation fronts, bow shocks or photo-evaporated clumps. In this model, clumps of gas form a complex shock field as they move rapidly through a uniform field and exhibit strong ionisation lines of

[O III] λ5007. This model, adapted for the higher velocities observed in novae, could be used to understand the high speed knots and excess oxygen observed in V445 Pup.

It is very important that future observations of V445 Pup be made across a wide range of wavelengths to understand all aspects of the nova. Recent optical observations, 11 years after outburst, should be able to reveal the current state of the nova shell and jet structures in V445 Pup. This can be combined with high resolution spectrographic observations in a range of wavelengths to constrain the spatial kinematic properties of the nova for improved hydrodynamical modeling. It would be of special interest to see how far the knots have progressed and whether the excess spectrum has evolved sufficiently to indicate shock ionisation. In their paper, Woudt et al. (2009) mention that mid- to far-infrared observations had been obtained using *Spitzer* that could better constrain the nova shell temperature, although these results have yet to be published. Using radio observations, Sokoloski et al. (2008) were able to model the highly collimated outflows of RS Oph. Such observations at radio wavelengths may therefore reveal and help to explain some of the jet structure within V445 Pup. Strong soft X-rays were not observed prior to outburst which is possibly due to the substantial equatorial dust disc obscuring the nova remnant. Once the nova shell has cooled enough to become transparent to the inner binary system, soft luminous X-rays are expected to be observed but as of yet, the X-ray satellite ROSAT has not identified V445 Pup (Woudt et al. 2009).

The results in this thesis, in addition to previous research on this nova, indicates that V445 Pup is a very unique and interesting object and is therefore a prime candidate for future observations. Once the equatorial dust disc fades, the binary system components can properly be deduced and therefore, the source of the collimated outflows can be investigated. As the axis of the outward ejecta is almost aligned with the plane of the sky, it is expected that the orbital plane of binary system is $\sim 86^{\circ}$, implying that it will be an eclipsing binary system (Woudt et al. 2009). If this is the case, masses of the individual components can be obtained from detailed light curves and the possibility that V445 Pup could be the progenitor of a SN Ia can properly be explored.

Appendices A

Observing Log

Table A.1: Night 1: 4 January 2006

Frame	Object	UT Start	Exposure Time (s)	RA (hh:mm:ss)	DEC (dd:mm:ss)	Airmass
16	Dome Flat	19:21:13	300	21:40:10.9	-29:04:17.2	1
17	Dome Flat	19:28:15	300	21:47:14.1	-29:04:19.3	1
18	Dome Flat	19:34:48	300	21:53:48.2	-29:04:21.1	1
19	Dome Flat	19:41:22	300	22:00:23.0	-29:04:22.9	1
20	Dome Flat	19:47:54	300	22:06:57.1	-29:04:24.6	1
21	Dome Flat	19:54:43	300	22:13:46.9	-29:04:26.2	1
22	Dome Flat	20:01:17	300	22:20:22.1	-29:04:27.8	1
23	Dome Flat	20:07:50	300	22:26:56.1	-29:04:29.2	1
24	Dome Flat	20:14:23	300	22:33:34.4	-29:04:30.6	1
68	GD50	01:10:22	300	03:48:49.3	-00:59:20.6	1.138
70	GD50	01:23:30	600	03:48:49.3	-00:59:20.0	1.134
71	GD50	01:35:42	600	03:48:49.3	-00:59:21.7	1.133
72	ARC GD50	01:48:02	90	03:48:49.3	-00:59:21.9	1.135
75	ARC IC 2165	02:08:27	90	06:21:41.8	-12:59:54.3	1.175
76	IC 2165	02:11:40	300	06:21:41.8	-12:59:54.1	1.167
77	IC 2165	02:18:21	300	06:21:41.9	-12:59:54.1	1.151
78	IC 2165	02:24:54	300	06:21:41.9	-12:59:53.9	1.137
79	ARC IC 2165	02:32:02	90	06:21:41.9	-12:59:54.0	1.123
83	ARC V445Pup	03:07:58	90	07:37:56.0	-25:57:35.1	1.153
84	V445 Pup	03:11:31	1800	07:37:56.1	-25:57:33.7	1.144
85	V445 Pup	03:43:10	1800	07:37:56.1	-25:57:33.0	1.079
86	V445 Pup	04:14:43	1800	07:37:56.0	-25:57:34.0	1.036
87	ARC V445 Pup	04:46:56	90	07:37:55.9	-25:57:34.1	1.011
88	V445 Pup	04:50:46	1800	07:37:55.8	-25:57:46.1	1.009
89	V445 Pup	05:22:26	1800	07:37:56.6	-25:57:52.9	1.001
90	ARC V445 Pup	05:56:55	90	07:37:56.6	-25:57:53.0	1.011
93	V445 Pup	06:16:41	1800	07:37:56.7	-25:57:50.8	1.024
94	V445 Pup	06:48:18	1800	07:37:56.6	-25:57:50.5	1.06
95	ARC V445Pup	07:20:32	90	07:37:56.6	-25:57:50.4	1.117
96	Skyflat	07:24:01	300	07:37:56.6	-25:57:50.4	1.124
97	Skyflat	07:30:34	300	07:37:56.6	-25:57:50.4	1.139
98	Skyflat	07:37:07	300	07:37:56.6	-25:57:50.4	1.156

Table A.2: Night 2: 5 January 2006

Frame	Object	UT Start	Exposure Time (s)	RA (hh:mm:ss)	DEC (dd:mm:ss)	Airmass
13	Dome Flat	18:58:26	300	21:21:16.8	-29:02:58.6	1
14	Dome Flat	19:05:10	300	21:28:02.2	-29:03:00.8	1
15	Dome Flat	19:11:43	300	21:34:36.2	-29:03:02.8	1
16	Dome Flat	19:18:16	300	21:41:10.5	-29:03:04.8	1
17	Dome Flat	19:24:49	300	21:47:44.5	-29:03:06.7	1
18	Dome Flat	19:31:23	300	21:54:19.4	-29:03:08.5	1
19	Dome Flat	19:37:56	300	22:00:53.6	-29:03:10.3	1
20	Dome Flat	19:44:29	300	22:07:27.8	-29:03:12.0	1
21	Dome Flat	19:51:03	300	22:14:02.6	-29:03:13.6	1
22	Dome Flat	19:57:36	300	22:20:36.9	-29:03:15.1	1
23	Dome Flat	20:04:09	300	22:27:11.1	-29:03:16.5	1
24	Dome Flat	20:10:51	300	22:33:55.0	-29:03:17.9	1
50	GD50	01:04:22	600	03:48:51.0	-00:59:20.2	1.139
51	GD50	01:16:01	600	03:48:50.9	-00:59:19.1	1.135
52	ARC GD50	01:28:09	90	03:48:51.0	-00:59:19.0	1.133
54	ARC IC2156	01:43:27	90	06:21:43.1	-13:00:02.0	1.235
55	IC2156	01:46:36	300	06:21:43.1	-13:00:02.0	1.225
56	IC2156	01:53:15	300	06:21:43.1	-13:00:01.9	1.205
57	IC2156	01:59:48	300	06:21:43.2	-13:00:01.7	1.187
58	ARC IC2156	02:07:00	90	06:21:43.2	-13:00:02.0	1.169
62	ARC V445 Pup	02:30:27	90	07:37:57.2	-25:57:44.9	1.255
63	V445 Pup	02:33:37	1800	07:37:57.2	-25:57:44.1	1.244
64	V445 Pup	03:05:34	1800	07:37:57.3	-25:57:43.1	1.149
65	V445 Pup	03:37:07	1800	07:37:57.3	-25:57:42.1	1.083
66	ARC V445 Pup	04:08:54	90	07:37:57.2	-25:57:42.8	1.039

Table A.3: Night 3: 8 January 2007

Frame	Object	UT Start	Exposure Time (s)	RA (hh:mm:ss)	DEC (dd:mm:ss)	Airmass
50	Dome Flat	21:41:06	180	00:13:18.4	-29:04:54.3	1
51	Dome Flat	21:46:24	180	00:18:37.6	-29:04:54.2	1
52	Dome Flat	21:51:42	180	00:23:56.8	-29:04:54.1	1
53	Dome Flat	21:57:00	180	00:29:16.0	-29:04:53.8	1
54	Dome Flat	22:02:19	180	00:34:35.1	-29:04:53.5	1
55	Dome Flat	22:07:37	180	00:39:54.1	-29:04:53.1	1
56	Dome Flat	22:12:55	180	00:45:13.3	-29:04:52.7	1
57	Dome Flat	22:18:13	180	00:50:32.2	-29:04:52.1	1
58	Dome Flat	22:23:31	180	00:55:51.4	-29:04:51.5	1
59	Dome Flat	22:28:49	180	01:01:10.4	-29:04:50.9	1
60	Dome Flat	22:34:07	180	01:06:29.5	-29:04:50.1	1
131	ARC LTT2415	04:23:03	90	05:56:26.0	-27:52:16.7	1.025
132	LTT2415	04:26:57	600	05:56:25.9	-27:52:15.1	1.028
137	ARC V445 Pup	05:19:07	90	07:37:59.4	-25:56:39.9	1.002
138	V445 Pup	05:23:03	1800	07:37:59.8	-25:56:35.9	1.003
141	V445 Pup	06:06:56	1800	07:37:59.8	-25:56:33.9	1.029
142	ARC V445 Pup	06:40:02	90	07:37:59.8	-25:56:33.8	1.07
143	V445 Pup	06:43:57	1800	07:37:59.8	-25:56:33.5	1.076
144	V445 Pup	07:16:20	1800	07:38:00.0	-25:56:33.8	1.141
145	ARC V445 Pup	07:48:46	90	07:38:00.0	-25:56:33.9	1.234
146	V445 Pup	07:52:44	1800	07:38:00.1	-25:56:35.7	1.247
147	V445 Pup	08:25:05	1800	07:38:00.2	-25:56:37.8	1.384
148	ARC V445 Pup	08:57:34	90	07:38:00.2	-25:56:37.9	1.581
159	Skyflat	09:41:20	30	12:12:56.9	-29:00:28.2	1
160	Skyflat	09:44:11	30	12:15:48.0	-29:00:28.2	1

Table A.4: Night 4: 9 January 2007

Frame	Object	UT Start	Exposure Time (s)	RA (hh:mm:ss)	DEC (dd:mm:ss)	Airmass
40	Dome Flat	20:00:55	180	22:36:44.2	-29:04:59.9	1
41	Dome Flat	20:06:25	180	22:42:14.7	-29:05:01.1	1
42	Dome Flat	20:11:43	180	22:47:34.1	-29:05:02.2	1
43	Dome Flat	20:17:02	180	22:52:53.1	-29:05:03.3	1
44	Dome Flat	20:22:20	180	22:58:12.2	-29:05:04.2	1
45	Dome Flat	20:27:38	180	23:03:31.2	-29:05:05.1	1
46	Dome Flat	20:32:56	180	23:08:50.2	-29:05:06.0	1
47	Dome Flat	20:38:14	180	23:14:09.3	-29:05:06.7	1
48	Dome Flat	20:43:32	180	23:19:28.3	-29:05:07.4	1
49	Dome Flat	20:48:50	180	23:24:47.3	-29:05:08.1	1
101	ARC V445 Pup	04:55:32	90	07:37:58.8	-25:56:29.3	1.002
102	V445 Pup	04:59:27	1800	07:37:59.3	-25:56:37.9	1.002
103	V445 Pup	05:31:48	1800	07:37:59.5	-25:56:36.0	1.008
104	V445 Pup	06:04:12	1800	07:37:59.5	-25:56:34.5	1.03
105	ARC V445 Pup	06:36:48	90	07:37:59.4	-25:56:34.7	1.071
124	LTT3864	08:44:27	300	10:32:10.3	-35:37:56.9	1.022
125	LTT3864	08:52:35	300	10:32:10.3	-35:37:57.4	1.028
126	LTT3864	08:59:58	300	10:32:10.2	-35:37:54.9	1.035
127	ARC LTT3864	09:07:21	90	10:32:10.2	-35:37:54.9	1.042

Table A.5: Night 5: 10 January 2007

Frame	Object	UT Start	Exposure Time (s)	RA (hh:mm:ss)	DEC (dd:mm:ss)	Airmass
15	Dome Flat	19:47:15	180	22:24:10.0	-29:21:12.3	1
16	Dome Flat	19:52:33	180	22:29:29.9	-29:21:22.7	1
17	Dome Flat	19:57:51	180	22:34:49.7	-29:21:32.5	1
18	Dome Flat	20:03:09	180	22:40:09.7	-29:21:41.8	1
19	Dome Flat	20:08:27	180	22:45:29.7	-29:21:50.4	1
20	Dome Flat	20:13:45	180	22:50:49.5	-29:21:58.5	1
21	Dome Flat	20:19:03	180	22:56:09.5	-29:22:06.0	1
22	Dome Flat	20:24:22	180	23:01:29.3	-29:22:13.0	1
23	Dome Flat	20:29:40	180	23:06:49.1	-29:22:19.3	1
24	Dome Flat	20:34:58	180	23:12:09.1	-29:22:25.0	1
25	Dome Flat	20:40:16	180	23:17:29.2	-29:22:30.1	1
77	GD50	00:42:29	300	03:48:51.0	-00:59:13.9	1.141
78	ARC GD50	00:50:28	90	03:48:51.0	-00:59:14.7	1.137
127	ARC V445 Pup	06:46:54	90	07:37:54.5	-25:57:20.4	1.095
131	V445 Pup	07:09:02	1200	07:37:54.4	-25:57:30.0	1.142
132	V445 Pup	07:31:20	1200	07:37:54.5	-25:57:30.3	1.203
133	V445 Pup	07:53:39	900	07:37:54.6	-25:57:30.4	1.28
134	ARC V445 Pup	08:11:00	90	07:37:54.6	-25:57:30.6	1.355
138	LTT3864	08:59:24	300	10:32:14.6	-35:38:25.1	1.038
139	LTT3864	09:06:52	300	10:32:14.7	-35:38:24.8	1.045
140	ARC LTT3864	09:14:19	90	10:32:14.7	-35:38:24.8	1.054

Appendices B

Line Identification

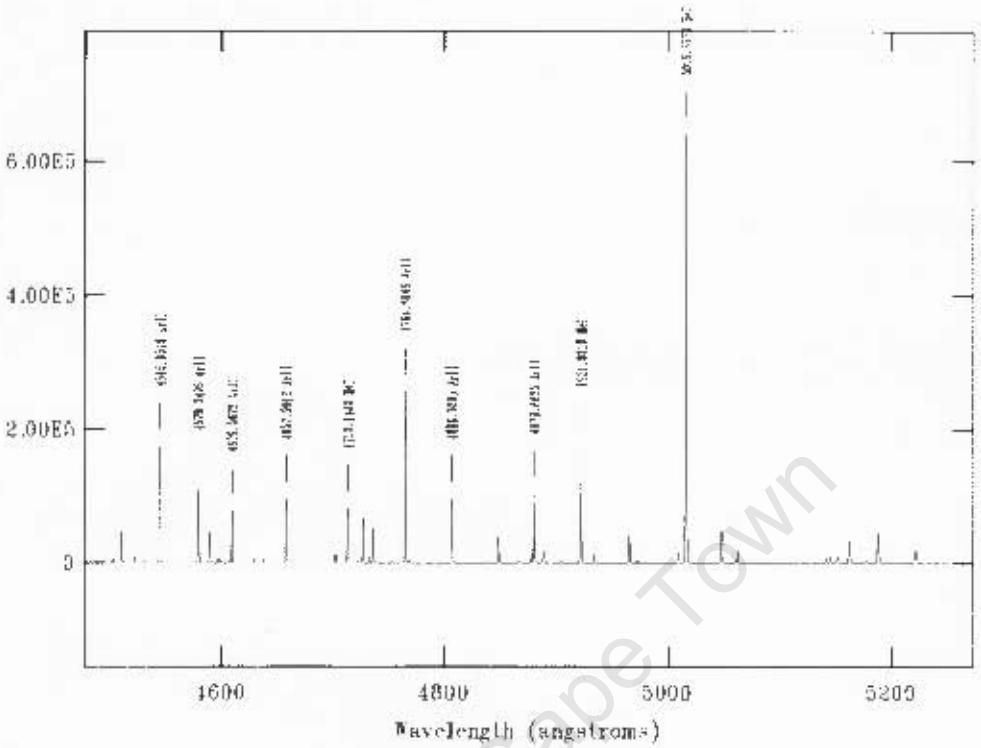

(a) HeNeAr Spectral Atlas Chart: 4500 Å to 5250 Å (Crosswhite 1975)

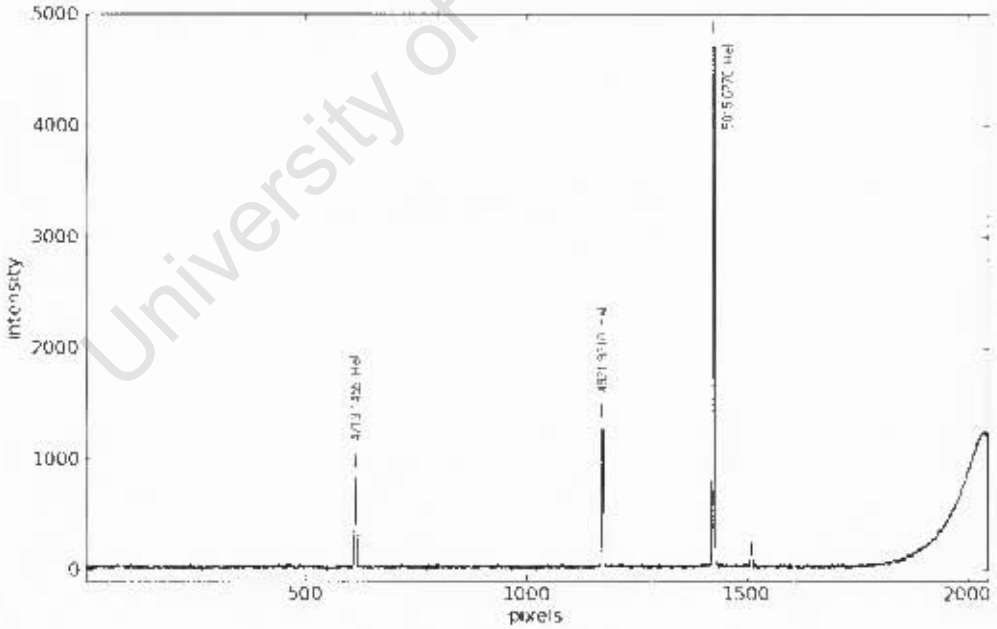

(b) Identification Arc Spectrum: Frame 83, CCD 4

Figure B.1: Lines are identified in the example arc image (Frame 83, 4 January 2006, in lower panel) using the Spectral Atlas line identification chart (upper panel) in the wavelength range 1500 Å to 5250 Å (associated with CCD 4 and CCD 7).

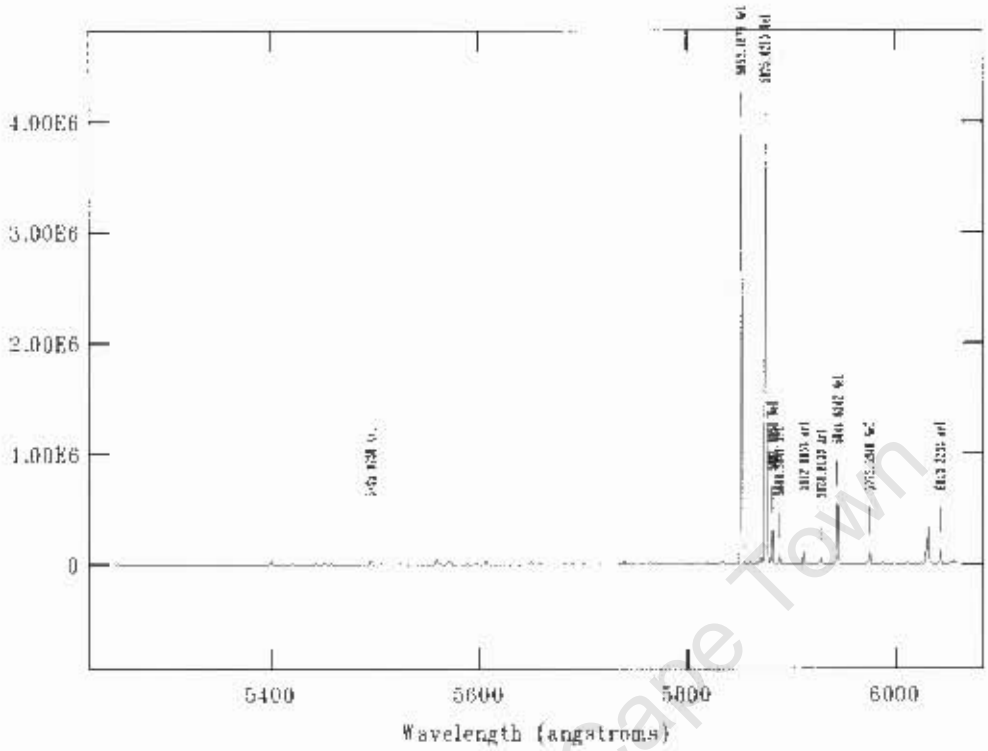

(a) HeNeAr Spectral Atlas Chart: 5250 Å to 6000 Å (Crosswhite 1975)

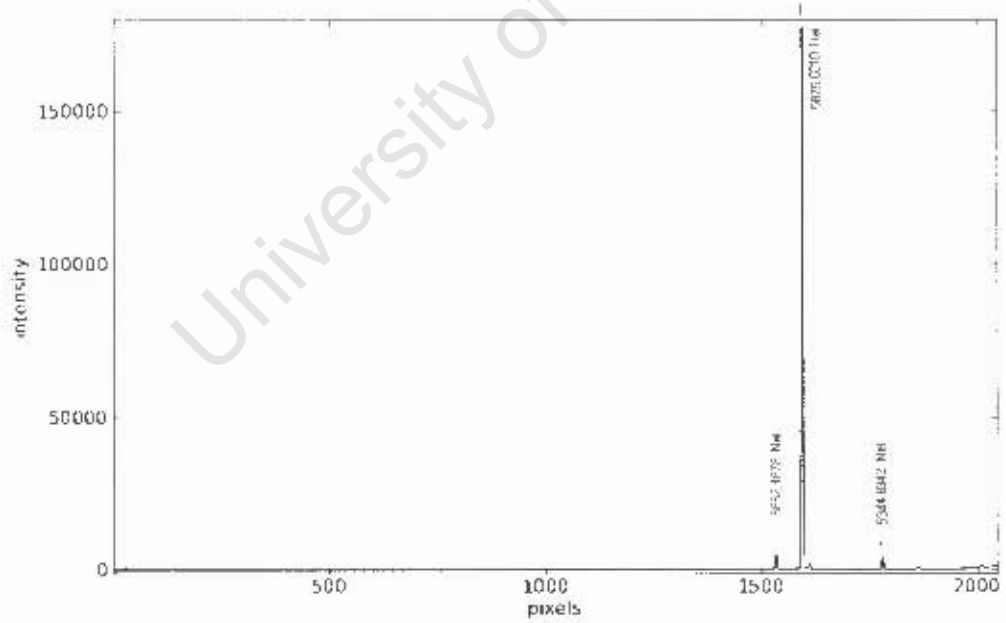

(b) Identification Arc Spectrum: Frame 83, CCD 3

Figure B.2: Lines are identified in the example arc image (Frame 83, 4 January 2006, in lower panel) using the Spectral Atlas line identification chart (upper panel) in the wavelength range 5250 Å to 6000 Å (associated with CCD 3 and CCD 8).

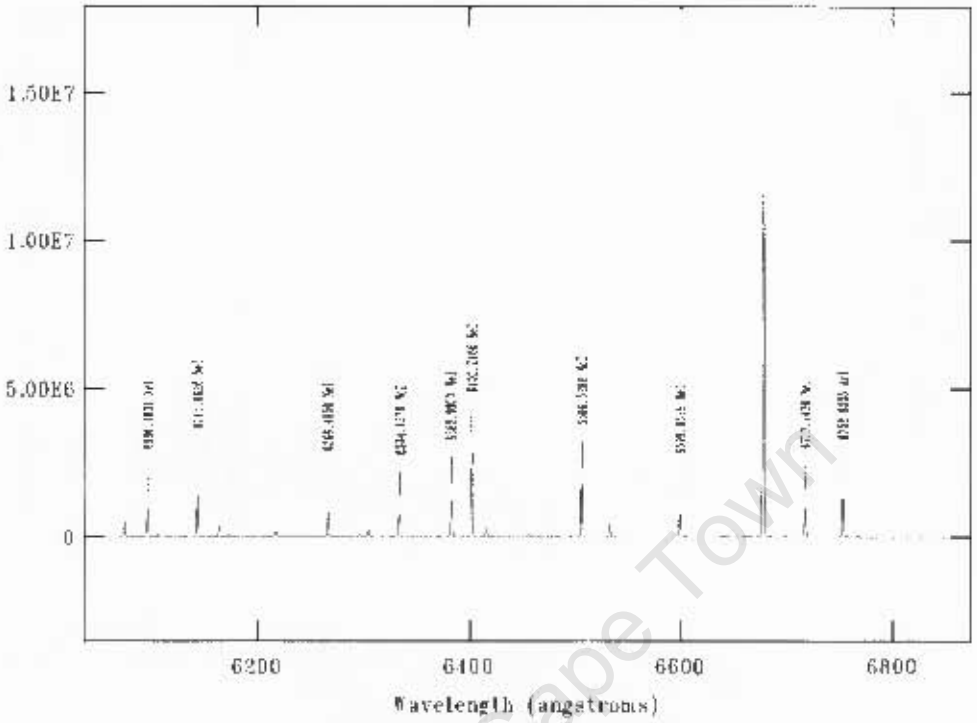

(a) HeNeAr Spectral Atlas Chart: 6000 Å to 6850 Å (Crosswhite 1975)

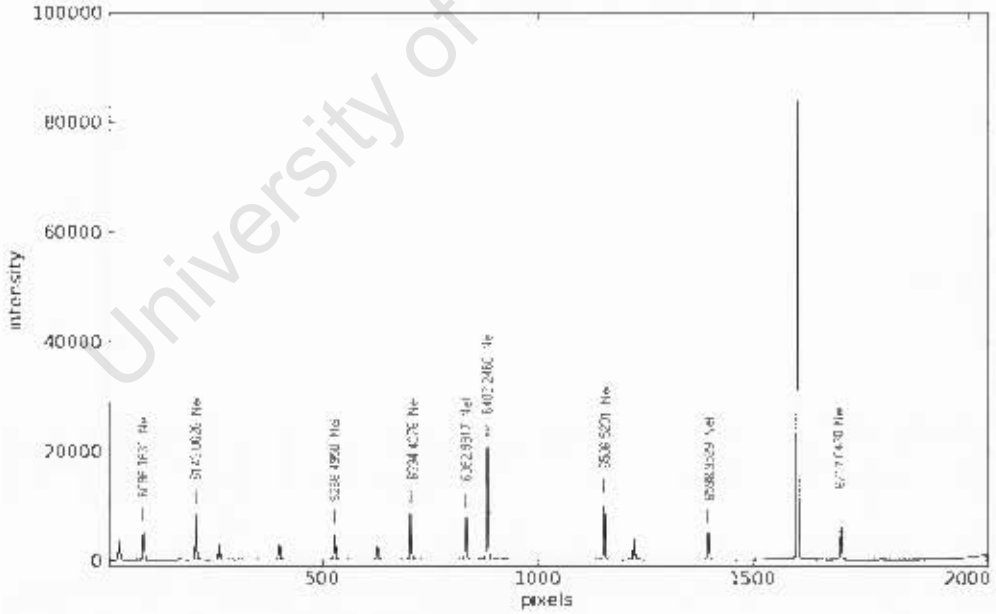

(b) Identification Arc Spectrum: Frame 83, CCD 2

Figure B.3: Lines are identified in the example arc image (Frame 83, 4 January 2006, in lower panel) using the Spectral Atlas line identification chart (upper panel) in the wavelength range 6000 Å to 6850 Å (associated with CCD 2 and CCD 5).

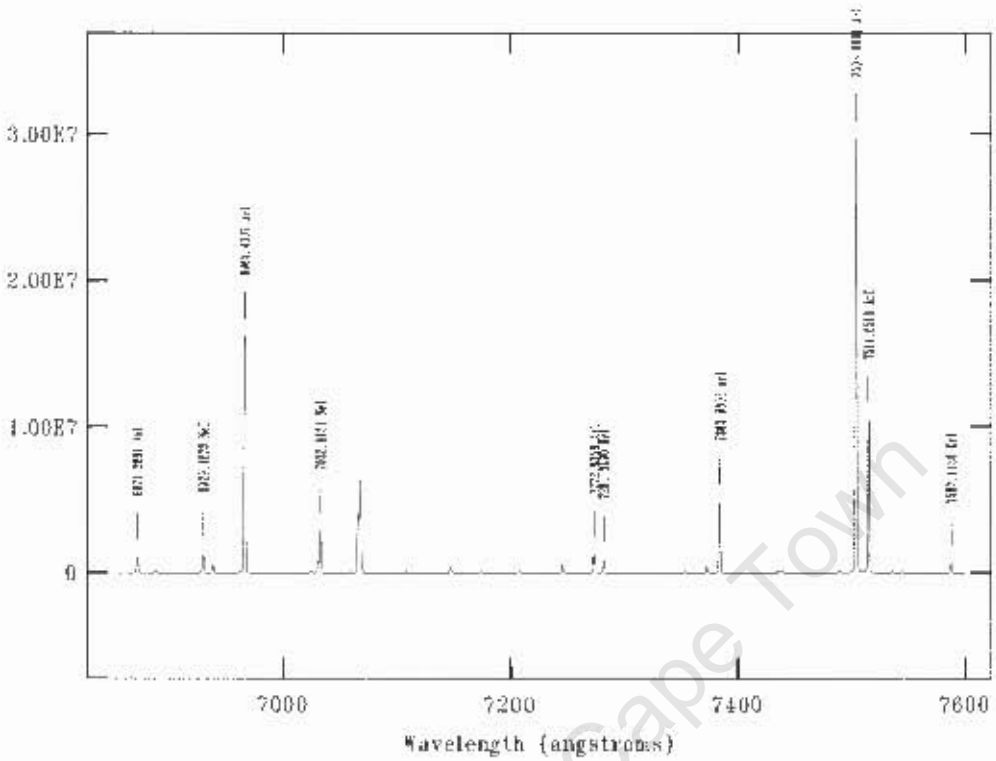

(a) HeNeAr Spectral Atlas Chart: 6850 Å to 7600 Å (Crosswhite 1975)

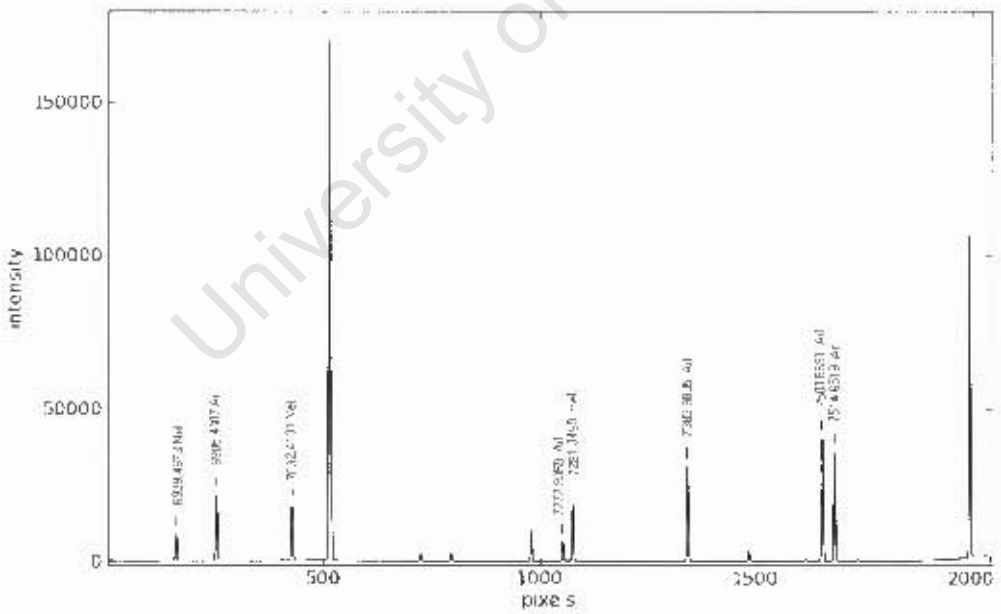

(b) Identification Arc Spectrum: Frame 83, CCD 1

Figure B.4: Lines are identified in the example arc image (Frame 83, 4 January 2006, in lower panel) using the Spectral Atlas line identification chart (upper panel) in the wavelength range 6850 Å to 7600 Å (associated with CCD 1 and CCD 6).

Appendices C

List of Abbreviations

1D	One-Dimensional
2D	Two-Dimensional
3D	Three-Dimensional
AO	Adaptive Optics
AM CVn	AM Canum Venaticorum star
B	Background Block
BC	Bolometric Correction
CCD	Charge Coupled Device
CN	Classical Nova
CO	Carbon Oxygen
CV	Cataclysmic Variable Star
DEC	Declination
FWHM	Full Width at Half Maximum
IFU	Integral Field Unit
IMACS	Inamori Magellan Areal Camera and Spectrograph
IRAF	Image Reduction and Analysis Facility
NE	North-East
NIST	National Institute of Standards and Technology
O	Object Block
PN	Planetary Nebula
RA	Right Ascension
RMS	Root Mean Squared
RS Oph	RS Orphiuchi
SN Ia	Type Ia Supernova
THEA	Transient Heavy Element Absorption system
SW	South-West
UT	Universal Time
V445 Pup	V445 Puppis
VLT	Very Large Telescope
WD	White Dwarf

Bibliography

Allen, M. G., Groves, B. A., Dopita, M. A., Sutherland, R. S., & Kewley, L. J. 2008, ApJS, 178, 20

Allington-Smith, J. & Content, R. 1998, PASP, 110, 1216

Ashok, N. M. & Banerjee, D. P. K. 2003, A&A, 409, 1007

Balick, B. & Hajian, A. R. 2004, AJ, 127, 2269

Bildsten, L., Shen, K. J., Weinberg, N. N., & Nelemans, G. 2007, ApJ, 662, L95

Bode, M. & Evans, A. 2008, Classical novae, Cambridge astrophysics series (Cambridge University Press)

Bode, M. F., ed. 1987, RS Ophiuchi (1985) and the recurrent nova phenomenon

Bode, M. F., Harman, D. J., O'Brien, T. J., Bond, H. E., Starrfield, S., Darnley, M. J., Evans, A., & Eyres, S. P. S. 2007, ApJ, 665, L63

Branch, D. & Nomoto, K. 2007, Nature, 447, 393

Chandrasekhar, T., Ashok, N. M., & Ragland, S. 1992, MNRAS, 255, 412

Crosswhite, H. M. 1975, Journal of Research of the National Bureau of Standards, 79, 17

Dressler, A., Bigelow, B., Hare, T., Sutin, B., Thompson, I., Burley, G., Epps, H., Oemler, A., Bagish, A., Birk, C., Clardy, K., Gunnels, S., Kelson, D., Shectman, S., & Osip, D. 2011, PASP, 123, 288

Eyres, S. P. S., O'Brien, T. J., Beswick, R., Muxlow, T. W. B., Anupama, G. C., Kantharia, N. G., Bode, M. F., Gawroński, M. P., Feiler, R., Evans, A., Rushton, M. T., Davis, R. J., Prabhu, T., Porcas, R., & Hassall, B. J. M. 2009, MNRAS, 395, 1533

Fernández, R., Schwarz, H. E., & Monteiro, H. 2004, in Astronomical Society of the Pacific Conference Series, Vol. 313, Asymmetrical Planetary Nebulae III: Winds, Structure and the Thunderbird, ed. M. Meixner, J. H. Kastner, B. Balick, & N. Soker, 236

Gaposchkin, C. 1964, The galactic novae (Dover Publications)

Gehrz, R. 1989, in IAU Symposium, Vol. 135, Interstellar Dust, ed. L. J. Allamandola & A. G. G. M. Tielens, 445–+

Guerrero, M. A., Miranda, L. F., Riera, A., Velázquez, P. F., Olguín, L., Vázquez, R., Chu, Y.-H., Raga, A., & Benítez, G. 2008, ApJ, 683, 272

Hachisu, I. & Kato, M. 2001, ApJ, 558, 323

Harman, D. J. & O'Brien, T. J. 2003, MNRAS, 344, 1219

Hellier, C. 2001, Cataclysmic Variable Stars, ed. Hellier, C.

Iben, Jr., I. & Tutukov, A. V. 1991, ApJ, 370, 615

—. 1994, ApJ, 431, 264

Iijima, T. 2009, A&A, 505, 287

Iijima, T. & Esenoglu, H. H. 2003, A&A, 404, 997

Iijima, T. & Nakanishi, H. 2008, A&A, 482, 865

Kato, M. & Hachisu, I. 1999, ApJ, 513, L41

—. 2003a, ApJ, 587, L39

—. 2003b, ApJ, 598, L107

—. 2005, ApJ, 633, L117

Kato, M., Hachisu, I., Kiyota, S., & Saio, H. 2008, ApJ, 684, 1366

Kato, M., Saio, H., & Hachisu, I. 1989, ApJ, 340, 509

Kato, T., Kanatsu, K., Takamizawa, K., Takao, A., & Stubbings, R. 2000, IAU Circ., 7552, 1

Koornneef, J. 1983, A&A, 128, 84

Li, W., Bloom, J. S., Podsiadlowski, P., Miller, A. A., Cenko, S. B., Jha, S. W., Sullivan, M., Howell, D. A., Nugent, P. E., Butler, N. R., Ofek, E. O., Kasliwal, M. M., Richards, J. W., Stockton, A., Shih, H.-Y., Bildsten, L., Shara, M. M., Bibby, J., Filippenko, A. V., Ganeshalingam, M., Silverman, J. M., Kulkarni, S. R., Law, N. M., Poznanski, D., Quimby, R. M., McCully, C., Patel, B., Maguire, K., & Shen, K. J. 2011, Nature, 480, 348

Livio, M. 2000, in Type Ia Supernovae, Theory and Cosmology, ed. J. C. Niemeyer & J. W. Truran, 33

Lynch, D. K., Rudy, R. J., Mazuk, S., Venturini, C. C., Puetter, R. C., & Perry, R. B. 2004, AJ, 128, 2962

Lynch, D. K., Russell, R. W., & Sitko, M. L. 2001, AJ, 122, 3313

Mazzali, P. A., Maurer, I., Stritzinger, M., Taubenberger, S., Benetti, S., & Hachinger, S. 2011, MNRAS, 416, 881

Neckel, T. & Klare, G. 1980, A&AS, 42, 251

Osaki, Y. 1974, PASJ, 26, 429

Platais, I., Kozhurina-Platais, V., Zacharias, M. I., & Zacharias, N. 2001, IAU Circ., 7556, 1

Pottasch, S. R., Bernard-Salas, J., Beintema, D. A., & Feibelman, W. A. 2004, A&A, 423, 593

Raga, A. C., Riera, A., Mellema, G., Esquivel, A., & Velázquez, P. F. 2008, A&A, 489, 1141

Ralchenko, Y., Kramida, A., Reader, J., & NIST ASD Team. 2011, National Institute of Standards and Technology

Ribeiro, V. A. R. M., Bode, M. F., Darnley, M. J., Harman, D. J., Newsam, A. M., O'Brien, T. J., Bohigas, J., Echevarría, J. M., Bond, H. E., Chavushyan, V. H., Costero, R., Coziol, R., Evans, A., Eyres, S. P. S., León-Tavares, J., Richer, M. G., Tovmassian, G., Starrfield, S., & Zharikov, S. V. 2009, ApJ, 703, 1955

Rupen, M. P., Mioduszewski, A. J., & Dhawan, V. 2001, IAU Circ., 7728, 3

Rybicki, G. B. & Lightman, A. P. 1979, Radiative processes in astrophysics, ed. Rybicki, G. B. & Lightman, A. P.

Schlegel, D. J., Finkbeiner, D. P., & Davis, M. 1998, ApJ, 500, 525

Schmoll, J., Dodsworth, G. N., Content, R., & Allington-Smith, J. R. 2004, in Society of Photo-Optical Instrumentation Engineers (SPIE) Conference Series, Vol. 5492, Society of Photo-Optical Instrumentation Engineers (SPIE) Conference Series, ed. A. F. M. Moorwood & M. Iye, 624–633

Schönberner, D., Jacob, R., Steffen, M., Perinotto, M., Corradi, R. L. M., & Acker, A. 2005, A&A, 431, 963

Soker, N. & Rappaport, S. 2000, ApJ, 538, 241

Sokoloski, J. L., Rupen, M. P., & Mioduszewski, A. J. 2008, ApJ, 685, L137

Solf, J. & Ulrich, H. 1985, A&A, 148, 274

Starrfield, S., Sparks, W. M., & Truran, J. W. 1974, ApJS, 28, 247

Steffen, W., Espíndola, M., Martínez, S., & Koning, N. 2009, RevMexAA, 45, 143

Storey, P. J. & Zeippen, C. J. 2000, MNRAS, 312, 813

Sytov, A. Y., Bisikalo, D. V., Kaigorodov, P. V., & Boyarchuk, A. A. 2009, Astronomy Reports, 53, 223

Tody, D. 1993, in Astronomical Society of the Pacific Conference Series, Vol. 52, Astronomical Data Analysis Software and Systems II, ed. R. J. Hanisch, R. J. V. Brissenden, & J. Barnes, 173–+

van Dokkum, P. G. 2001, PASP, 113, 1420

Wagner, R. M., Foltz, C. B., & Starrfield, S. G. 2001, IAU Circ., 7556, 2

Wang, B., Meng, X., Chen, X., & Han, Z. 2009, MNRAS, 395, 847

Warner, B. 1995, Cataclysmic Variable Stars, Cambridge Astrophysics (Cambridge University Press)

Weston, J. & Sokoloski, J. 2011, in American Astronomical Society Meeting Abstracts 218, 410.13

Williams, R. & Mason, E. 2010, Ap&SS, 327, 207

Williams, R., Mason, E., Della Valle, M., & Ederoclite, A. 2008, ApJ, 685, 451

Williams, R. E. 1992, AJ, 104, 725

—. 1994, ApJ, 426, 279

Wilson, R. E. 1953, Carnegie Institute Washington D.C. Publication, 0

Wooden, II, W. H. 1970, AJ, 75, 324

Woudt, P. A., Steeghs, D., Karovska, M., Warner, B., Groot, P. J., Nelemans, G., Roelofs, G. H. A., Marsh, T. R., Nagayama, T., Smits, D. P., & O'Brien, T. 2009, ApJ, 706, 738

Yoon, S.-C. & Langer, N. 2004, A&A, 419, 645